Incompressible Flow over Airfoils

Of the many problems now engaging attention, the following are considered of immediate importance and will be considered by the committee as rapidly as funds can be secured for the purpose. . . . The evolution of more efficient wing sections of practical form, embodying suitable dimensions for an economical structure, with moderate travel of the center-of-pressure and still affording a large range of angle-of-attack combined with efficient action.

From the first Annual Report of the NACA, 1915

PREVIEW BOX

Imagine that you have just been given an airfoil of a particular shape at a certain angle of attack to a given low-speed flow, and you have been asked to obtain the lift (or more importantly, the lift coefficient) of the airfoil. What do you do (besides panicking)? Your first inclination might be to make a model of the airfoil, put it in a low-speed wind tunnel, and measure the lift coefficient. This is indeed what aerodynamicists have been doing for more than 100 years. The early part of this chapter discusses such experimental measurements of airfoil properties in low-speed wind tunnels. These measurements give you an immediate feel for airfoil lift, drag, and moment coefficients as a function of angle of attack. The experimental measurements give you a fast track towards obtaining a comfortable and practical understanding as to how airfoils behave. That is what the first three sections of this chapter are all about.

Most of the rest of this chapter, however, deals with our second inclination as to how to obtain the airfoil properties, namely, to *calculate* them. This is a horse of a different color. You will be introduced to the elegant circulation theory of lift—the crowning jewel of inviscid, incompressible flow theory for the calculation of lift. At the turn of the twentieth century, the circulation theory of lift was a breakthrough

in the theoretical prediction of lift. In this chapter, we first apply this theory to thin airfoils at small angles of attack; thin airfoil theory was developed in Germany during World War I and is by far the most tractable means of obtaining analytical solutions for lift and moments on an airfoil. But, as we shall see, thin airfoil theory, as its name implies, holds only for thin airfoils at small angles of attack. This is not as restrictive as it seems, however, because many airplanes over the past years have relatively thin airfoils, and cruise at relatively small angles of attack. Thin airfoil theory gives us a lot of practical results, plus the intellectual gratification of carrying through some elegant theoretical thinking—give it a good read and I think you will like it.

Since the 1960s, the advent and development of the high-speed digital computer allowed detailed numerical solutions based on the circulation theory of lift, solutions for the lift on a body of arbitrary shape and thickness at any angle of attack, subject of course to the assumption of inviscid potential flow. These numerical solutions, an extension of the panel solutions discussed in Section 3.17, are discussed towards the end of this chapter—they are the "gold standard" for low-speed, inviscid-flow airfoil calculations, and are used throughout the aeronautical industry and by many aeronautical research and development laboratories. The concept of panel solutions is an inspired numerical application of the circulation theory of lift, and it has opened the door to the analysis of practically any airfoil shape at any angle of attack.

Airfoils come in many different shapes. An historical sequence of airfoil shapes through 1935 is shown in Figure 4.1. Beginning in 1938, the National Advisory Committee for Aeronautics (NACA) developed a revolutionary series of airfoil shapes designed to encourage laminar flow in the boundary layer over the airfoil, hence dramatically reducing skin friction drag on the airfoil; the shape of a representative laminar-flow airfoil is given in Figure 4.2. Although these shapes never produced the desired amount of laminar flow in practice, by a stroke of serendipity they proved to be excellent high-speed airfoils for jet-powered airplanes after 1945. Beginning in 1965 National Aeronautics and Space Administration (NASA)
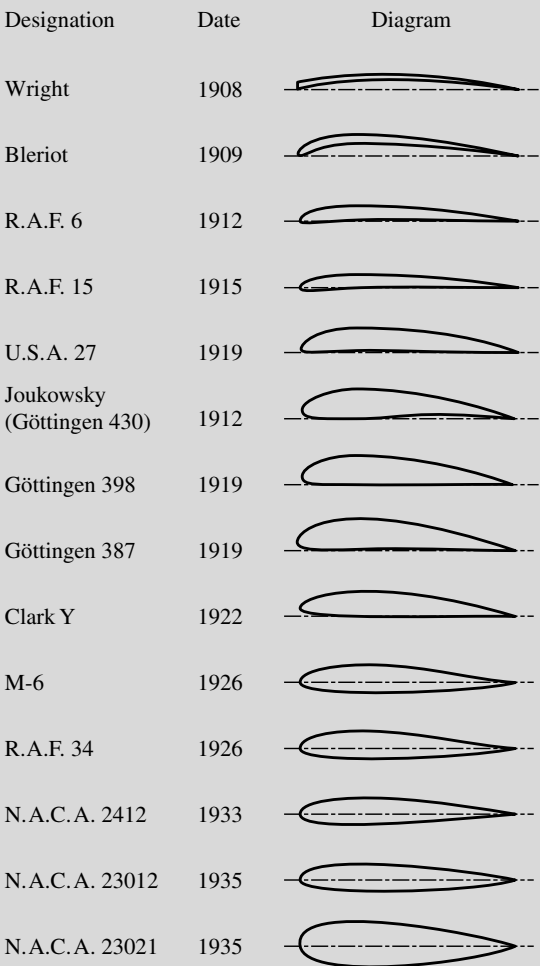
Designation	Date	Diagram
Wright	1908	
Bleriot	1909	
R.A.F. 6	1912	
R.A.F. 15	1915	
U.S.A. 27	1919	
Joukowsky (Göttingen 430)	1912	
Göttingen 398	1919	
Göttingen 387	1919	
Clark Y	1922	
M-6	1926	
R.A.F. 34	1926	
N.A.C.A. 2412	1933	
N.A.C.A. 23012	1935	
N.A.C.A. 23021	1935	

Figure 4.1 Historical sequence of airfoil sections. (Millikan, Clark B., *Aerodynamics of the Airplane,* Wiley, 1941.)
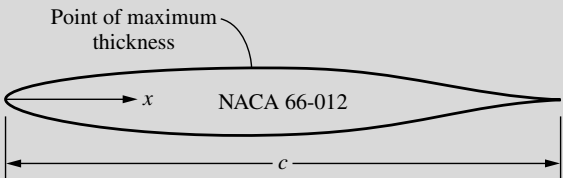
Figure 4.2 Laminar-flow airfoil shape.

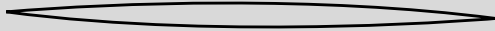**Figure 4.3** Supercritical airfoil shape.

Figure 4.4 Supersonic airfoil shapes.

developed another series of revolutionary airfoil shapes, supercritical airfoils, designed for efficient flight near Mach one; a typical supercritical airfoil shape is shown in Figure 4.3. Classic airfoil shapes for supersonic flow are shown in Figure 4.4; note the very slender profiles with sharp leading edges. All the airfoil shapes shown in Figure 4.1 through 4.4 were designed for specific purposes in their time and have been used on untold numbers of different airplanes. Today, the proper design of new airfoil shapes is more important than ever. Using numerical techniques, aircraft companies usually custom-design the airfoil shapes for new airplanes, shapes that best fit the design requirements for the specific airplane. This chapter is exclusively devoted to the study of airfoils; it discusses the fundamental aspects of airfoil aerodynamics—aspects that are the heart of airfoil design and performance.

Figure 4.5 shows an airplane in flight, sustained in the air by the aerodynamic action of its wing. Airplane wings are made up of airfoil shapes. The first step in understanding the aerodynamics of wings is to understand the aerodynamics of airfoils. Airfoil aerodynamics is important stuff—it is the stuff of this chapter. Moreover, it is truly interesting. It is fun to visualize the flow over an airfoil and to learn how to calculate the resulting lift on the airfoil. Read on and enjoy.

Figure 4.5 DeHaviland DHC-6 Twin Otter.
© PhotoDisc/Alamy RF

4.1 INTRODUCTION

With the advent of successful powered flight at the turn of the twentieth century, the importance of aerodynamics ballooned almost overnight. In turn, interest grew in the understanding of the aerodynamic action of such lifting surfaces as fixed wings on airplanes and, later, rotors on helicopters. In the period 1912–1918, the analysis of airplane wings took a giant step forward when Ludwig Prandtl and his colleagues at Göttingen, Germany, showed that the aerodynamic consideration of wings could be split into two parts: (1) the study of the

section of a wing—an airfoil—and (2) the modification of such airfoil properties to account for the complete, finite wing. This approach is still used today; indeed, the theoretical calculation and experimental measurement of modern airfoil properties have been a major part of the aeronautics research carried out by the National Aeronautics and Space Administration (NASA) in the 1970s and 1980s. (See Chapter 5 of Reference 2 for a historical sketch on airfoil development and Reference 10 for a description of modern airfoil research.) Following Prandtl's philosophy, the present chapter deals exclusively with airfoils, whereas Chapter 5 treats the case of a complete, finite wing. Therefore, in this chapter and Chapter 5, we make a major excursion into aerodynamics as applied to airplanes.

What is an airfoil? Consider a wing as drawn in perspective in Figure 4.6. The wing extends in the y direction (the span direction). The freestream velocity V_∞ is parallel to the xz plane. Any section of the wing cut by a plane parallel to the xz plane is called an *airfoil*. The purpose of this chapter is to present theoretical methods for the calculation of airfoil properties. In most of this chapter we will deal with inviscid flow, which does not lead to predictions of airfoil drag; indeed, d'Alembert's paradox says that the drag on an airfoil is zero—clearly not a realistic answer. We will have to wait until Section 4.12 and Chapter 15 and a discussion of viscous flow before predictions of drag can be made. However, the lift and moments on the airfoil are due mainly to the pressure distribution, which (below the stall) is dictated by inviscid flow. Therefore, this chapter concentrates on the theoretical prediction of airfoil lift and moments.

The road map for this chapter is given in Figure 4.7. After some initial discussion on airfoil nomenclature and characteristics, we present two approaches to low-speed airfoil theory. One is the classical thin airfoil theory developed during the period 1910–1920 (the right-hand branch of Figure 4.7). The other is the modern numerical approach for arbitrary airfoils using vortex panels
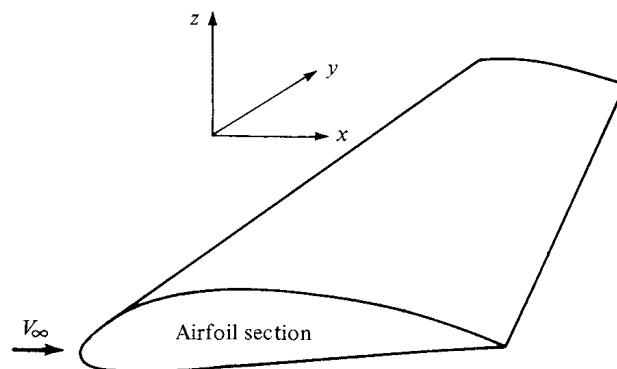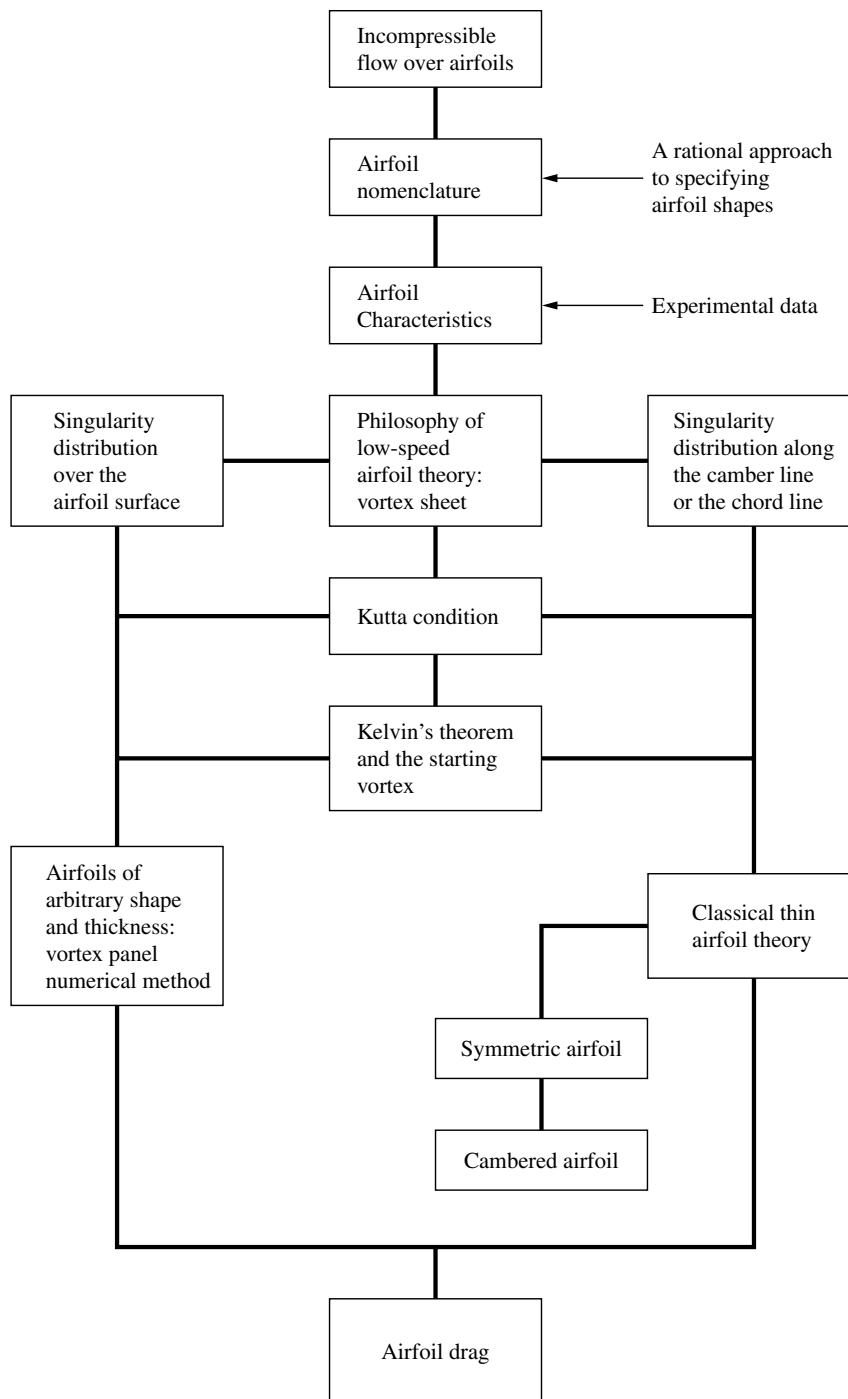

Figure 4.6 Definition of an airfoil.

```
┌──────────────────┐
│ Incompressible   │
│ flow over airfoils│
└──────────────────┘
         │
┌──────────────────┐        A rational approach
│ Airfoil          │ ◄───── to specifying
│ nomenclature     │        airfoil shapes
└──────────────────┘
         │
┌──────────────────┐
│ Airfoil          │ ◄───── Experimental data
│ Characteristics  │
└──────────────────┘
```

| Singularity distribution over the airfoil surface | Philosophy of low-speed airfoil theory: vortex sheet | Singularity distribution along the camber line or the chord line |

Kutta condition

Kelvin's theorem and the starting vortex

Airfoils of arbitrary shape and thickness: vortex panel numerical method

Classical thin airfoil theory

Symmetric airfoil

Cambered airfoil

Airfoil drag

Figure 4.7 Road map for Chapter 4.

(the left-hand branch of Figure 4.7). Please refer to this road map as you work your way through this chapter.

4.2 AIRFOIL NOMENCLATURE

The first patented airfoil shapes were developed by Horatio F. Phillips in 1884. Phillips was an Englishman who carried out the first serious wind-tunnel experiments on airfoils. In 1902, the Wright brothers conducted their own airfoil tests in a wind tunnel, developing relatively efficient shapes which contributed to their successful first flight on December 17, 1903 (see Section 1.1). Clearly, in the early days of powered flight, airfoil design was basically customized and personalized. However, in the early 1930s, NACA—the forerunner of NASA—embarked on a series of definitive airfoil experiments using airfoil shapes that were constructed rationally and systematically. Many of these NACA airfoils are in common use today. Therefore, in this chapter we follow the nomenclature established by the NACA; such nomenclature is now a well-known standard.

Consider the airfoil sketched in Figure 4.8. The *mean camber line* is the locus of points halfway between the upper and lower surfaces as measured perpendicular to the mean camber line itself. The most forward and rearward points of the mean camber line are the *leading and trailing edges,* respectively. The straight line connecting the leading and trailing edges is the *chord line* of the airfoil, and the precise distance from the leading to the trailing edge measured along the chord line is simply designated the *chord c* of the airfoil. The *camber* is the maximum distance between the mean camber line and the chord line, measured perpendicular to the chord line. The *thickness* is the distance between the upper and lower surfaces, also measured perpendicular to the chord line. The shape of the airfoil at the leading edge is usually circular, with a leading-edge radius of approximately $0.02c$. The shapes of all standard NACA airfoils are generated by specifying the shape of the mean camber line and then wrapping a specified symmetrical thickness distribution around the mean camber line.

The force-and-moment system on an airfoil was discussed in Section 1.5, and the relative wind, angle of attack, lift, and drag were defined in Figure 1.16. You should review these considerations before proceeding further.
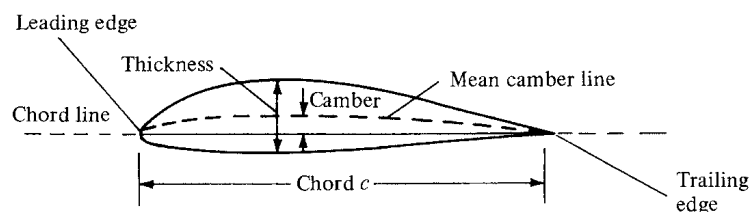

Figure 4.8 Airfoil nomenclature.

The NACA identified different airfoil shapes with a logical numbering system. For example, the first family of NACA airfoils, developed in the 1930s, was the "four-digit" series, such as the NACA 2412 airfoil. Here, the first digit is the maximum camber in hundredths of chord, the second digit is the location of maximum camber along the chord from the leading edge in tenths of chord, and the last two digits give the maximum thickness in hundredths of chord. For the NACA 2412 airfoil, the maximum camber is $0.02c$ located at $0.4c$ from the leading edge, and the maximum thickness is $0.12c$. It is common practice to state these numbers in percent of chord, that is, 2 percent camber at 40 percent chord, with 12 percent thickness. An airfoil with no camber, that is, with the camber line and chord line coincident, is called a *symmetric airfoil*. Clearly, the shape of a symmetric airfoil is the same above and below the chord line. For example, the NACA 0012 airfoil is a symmetric airfoil with a maximum thickness of 12 percent.

The second family of NACA airfoils was the "five-digit" series, such as the NACA 23012 airfoil. Here, the first digit when multiplied by $\frac{3}{2}$ gives the design lift coefficient[1] in tenths, the next two digits when divided by 2 give the location of maximum camber along the chord from the leading edge in hundredths of chord, and the final two digits give the maximum thickness in hundredths of chord. For the NACA 23012 airfoil, the design lift coefficient is 0.3, the location of maximum camber is at $0.15c$, and the airfoil has 12 percent maximum thickness.

One of the most widely used family of NACA airfoils is the "6-series" laminar flow airfoils, developed during World War II. An example is the NACA 65-218. Here, the first digit simply identifies the series, the second gives the location of minimum pressure in tenths of chord from the leading edge (for the basic symmetric thickness distribution at zero lift), the third digit is the design lift coefficient in tenths, and the last two digits give the maximum thickness in hundredths of chord. For the NACA 65-218 airfoil, the 6 is the series designation, the minimum pressure occurs at $0.5c$ for the basic symmetric thickness distribution at zero lift, the design lift coefficient is 0.2, and the airfoil is 18 percent thick.

The complete NACA airfoil numbering system is given in Reference 11. Indeed, Reference 11 is a definitive presentation of the classic NACA airfoil work up to 1949. It contains a discussion of airfoil theory, its application, coordinates for the shape of NACA airfoils, and a huge bulk of experimental data for these airfoils. This author strongly encourages you to read Reference 11 for a thorough presentation of airfoil characteristics.

As a matter of interest, the following is a short partial listing of airplanes currently in service that use standard NACA airfoils.

---

[1] The design lift coefficient is the theoretical lift coefficient for the airfoil when the angle of attack is such that the slope of the mean camber line at the leading edge is parallel to the freestream velocity.

Airplane	Airfoil
Beechcraft Sundowner	NACA 63A415
Beechcraft Bonanza	NACA 23016.5 (at root)
	NACA 23012 (at tip)
Cessna 150	NACA 2412
Fairchild A-10	NACA 6716 (at root)
	NACA 6713 (at tip)
Gates Learjet 24D	NACA 64A109
General Dynamics F-16	NACA 64A204
Lockheed C-5 Galaxy	NACA 0012 (modified)

In addition, many of the large aircraft companies today design their own special-purpose airfoils; for example, the Boeing 727, 737, 747, 757, 767, and 777 all have specially designed Boeing airfoils. Such capability is made possible by modern airfoil design computer programs utilizing either panel techniques or direct numerical finite-difference solutions of the governing partial differential equations for the flow field. (Such equations are developed in Chapter 2.)

4.3 AIRFOIL CHARACTERISTICS

Before discussing the theoretical calculation of airfoil properties, let us examine some typical results. During the 1930s and 1940s, the NACA carried out numerous measurements of the lift, drag, and moment coefficients on the standard NACA airfoils. These experiments were performed at low speeds in a wind tunnel where the constant-chord wing spanned the entire test section from one sidewall to the other. In this fashion, the flow "sees" a wing without wing tips—a so-called infinite wing, which theoretically stretches to infinity along the span (in the y direction in Figure 4.6). Because the airfoil section is the same at any spanwise location along the infinite wing, the properties of the airfoil and the infinite wing are identical. Hence, airfoil data are frequently called infinite wing data. (In contrast, we see in Chapter 5 that the properties of a finite wing are somewhat different from its airfoil properties.)

The typical variation of lift coefficient with angle of attack for an airfoil is sketched in Figure 4.9. At low-to-moderate angles of attack, c_l varies *linearly* with α; the slope of this straight line is denoted by a_0 and is called the *lift slope*. In this region, the flow moves smoothly over the airfoil and is attached over most of the surface, as shown in the streamline picture at the left of Figure 4.9. However, as α becomes large, the flow tends to separate from the top surface of the airfoil, creating a large wake of relatively "dead air" behind the airfoil as shown at the right of Figure 4.9. Inside this separated region, the flow is recirculating, and part of the flow is actually moving in a direction opposite to the freestream—so-called reversed flow. (Refer also to Figure 1.42.) This separated flow is due to viscous effects and is discussed in Section 4.12 and Chapter 15. The consequence of this separated flow at high α is a precipitous decrease in lift and a large increase in drag; under such conditions the airfoil is said to be *stalled*. The maximum
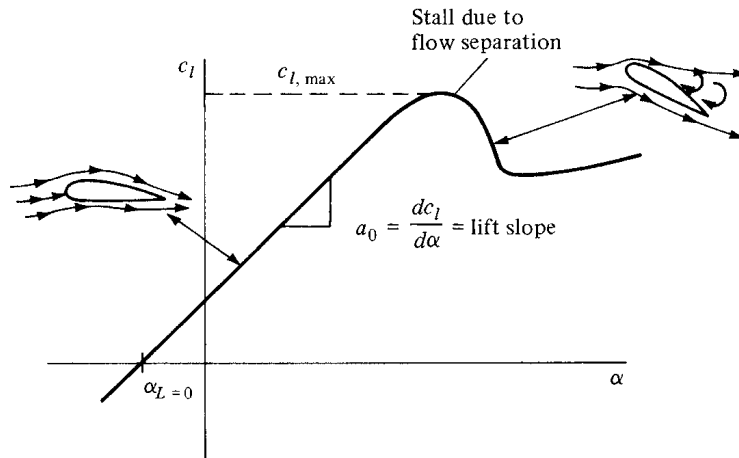
Figure 4.9 Schematic of lift-coefficient variation with angle of attack for an airfoil.

value of c_l, which occurs just prior to the stall, is denoted by $c_{l,\max}$; it is one of the most important aspects of airfoil performance, because it determines the stalling speed of an airplane. The higher is $c_{l,\max}$, the lower is the stalling speed. A great deal of modern airfoil research has been directed toward increasing $c_{l,\max}$. Again examining Figure 4.9, we see that c_l increases linearly with α until flow separation begins to have an effect. Then the curve becomes nonlinear, c_l reaches a maximum value, and finally the airfoil stalls. At the other extreme of the curve, noting Figure 4.9, the lift at $\alpha = 0$ is finite; indeed, the lift goes to zero only when the airfoil is pitched to some negative angle of attack. The value of α when lift equals zero is called the *zero-lift angle of attack* and is denoted by $\alpha_{L=0}$. For a symmetric airfoil, $\alpha_{L=0} = 0$, whereas for all airfoils with positive camber (camber *above* the chord line), $\alpha_{L=0}$ is a negative value, usually on the order of -2 or $-3°$.

The inviscid flow airfoil theory discussed in this chapter allows us to predict the lift slope a_0 and $\alpha_{L=0}$ for a given airfoil. It does not allow us to calculate $c_{l,\max}$, which is a difficult viscous flow problem, to be discussed in Chapters 15 to 20.

Experimental results for lift and moment coefficients for the NACA 2412 airfoil are given in Figure 4.10. Here, the moment coefficient is taken about the quarter-chord point. Recall from Section 1.6 that the force-and-moment system on an airfoil can be transferred to any convenient point; however, the quarter-chord point is commonly used. (Refresh your mind on this concept by reviewing Section 1.6, especially Figure 1.25.) Also shown in Figure 4.10 are theoretical results to be discussed later. Note that the experimental data are given for two different Reynolds numbers. The lift slope a_0 is not influenced by Re; however, $c_{l,\max}$ is dependent upon Re. This makes sense, because $c_{l,\max}$ is governed by viscous effects, and Re is a similarity parameter that governs the strength of inertia forces relative to viscous forces in the flow. [See Section 1.7 and Equation (1.35).]
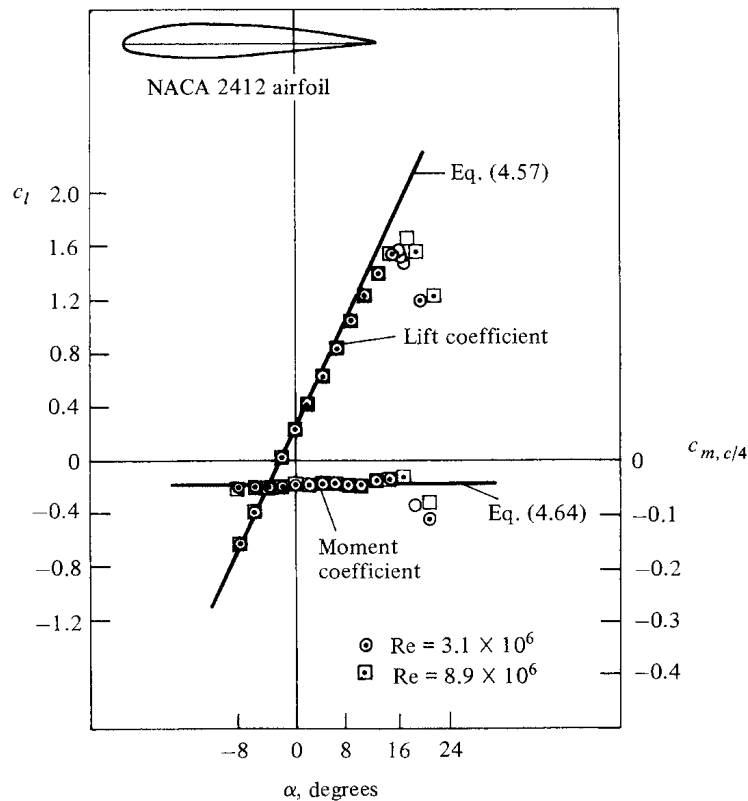
Figure 4.10 Experimental data for lift coefficient and moment
coefficient about the quarter-chord point for an NACA 2412 airfoil.
(Source: Data obtained from Abbott and von Doenhoff, Reference 11.)
Also shown is a comparison with theory described in Section 4.8.

The moment coefficient is also insensitive to Re except at large α. The NACA
2412 airfoil is a commonly used airfoil, and the results given in Figure 4.10 are
quite typical of airfoil characteristics. For example, note from Figure 4.10 that
$\alpha_{L=0} = -2.1°$, $c_{l,\max} \approx 1.6$, and the stall occurs at $\alpha \approx 16°$.

This chapter deals primarily with airfoil theory for an inviscid, incompressible
flow; such theory is incapable of predicting airfoil drag, as noted earlier. However,
for the sake of completeness, experimental data for the drag coefficient c_d for the
NACA 2412 airfoil are given in Figure 4.11 as a function of the angle of attack.[2]
The physical source of this drag coefficient is both skin friction drag and pres-
sure drag due to flow separation (so-called form drag). The sum of these two

---

[2] In many references, such as Reference 11, it is common to plot c_d versus c_l, rather than versus α. A plot
of c_d versus c_l is called a *drag polar*. For the sake of consistency with Figure 4.10, we choose to plot c_d
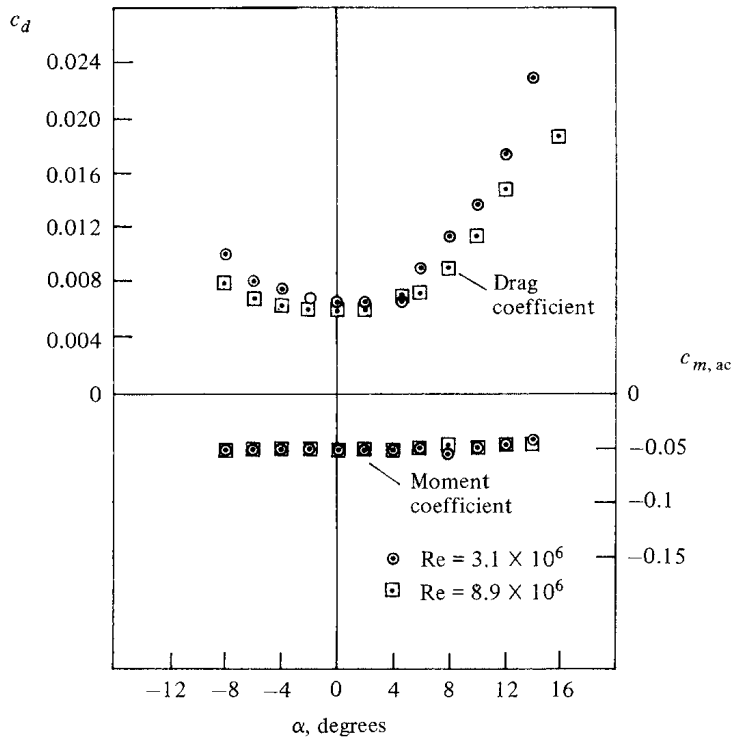versus α here.

Figure 4.11 Experimental data for profile drag coefficient and moment coefficient about the aerodynamic center for the NACA 2412 airfoil. *(Source: Data obtained from Abbott and von Doenhoff, Reference 11.)*

effects yields the *profile* drag coefficient c_d for the airfoil, which is plotted in Figure 4.11. Note that c_d is sensitive to Re, which is to be expected since both skin friction and flow separation are viscous effects. Again, we must wait until Section 4.12 and Chapters 15 to 20 to obtain some tools for theoretically predicting c_d.

Also plotted in Figure 4.11 is the moment coefficient about the aerodynamic center $c_{m,ac}$. In general, moments on an airfoil are a function of α. However, there is one point on the airfoil about which the moment is independent of angle of attack; such a point is defined as the *aerodynamic center*. Clearly, the data in Figure 4.11 illustrate a constant value for $c_{m,ac}$ over a wide range of α.

For an elementary but extensive discussion of airfoil and wing properties, see Chapter 5 of Reference 2.

EXAMPLE 4.1

Consider an NACA 2412 airfoil with a chord of 0.64 m in an airstream at standard sea level conditions. The freestream velocity is 70 m/s. The lift per unit span is 1254 N/m. Calculate the angle of attack and the drag per unit span.

■ **Solution**

At standard sea level, $\rho = 1.23$ kg/m^3:

$$q_\infty = \tfrac{1}{2}\rho_\infty V_\infty^2 = \tfrac{1}{2}(1.23)(70)^2 = 3013.5 \text{ N/m}^2$$

$$c_l = \frac{L'}{q_\infty S} = \frac{L'}{q_\infty c(1)} = \frac{1254}{3013.5(0.64)} = 0.65$$

From Figure 4.10, for $c_l = 0.65$, we obtain $\boxed{\alpha = 4^\circ}$.

To obtain the drag per unit span, we must use the data in Figure 4.11. However, since $c_d = f(\text{Re})$, let us calculate Re. At standard sea level, $\mu = 1.789 \times 10^{-5}$ kg/(m · s). Hence,

$$\text{Re} = \frac{\rho_\infty V_\infty c}{\mu_\infty} = \frac{1.23(70)(0.64)}{1.789 \times 10^{-5}} = 3.08 \times 10^6$$

Therefore, using the data for Re $= 3.1 \times 10^6$ in Figure 4.11, we find $c_d = 0.0068$. Thus,

$$D' = q_\infty S c_d = q_\infty c(1) c_d = 3013.5(0.64)(0.0068) = \boxed{13.1 \text{ N/m}}$$

EXAMPLE 4.2

For the airfoil and flow conditions given in Example 4.1, calculate the moment per unit span about the aerodynamic center.

■ **Solution**

From Figure 4.11, $c_{m,\text{ac}}$, which is independent of angle of attack, is -0.05. The moment per unit span about the aerodynamic center is

$$M'_{\text{ac}} = q_\infty S c c_{m,\text{ac}}$$

$$= (3013.5)(0.64)(0.64)(-0.05) = \boxed{-61.7 \text{ Nm}}$$

Recall the sign convention for aerodynamic moments introduced in Section 1.5, namely, that a negative moment, as obtained here, is a pitch-down moment, tending to reduce the angle of attack.

EXAMPLE 4.3

For the NACA 2412 airfoil, calculate and compare the lift-to-drag ratios at angles of attack of 0, 4, 8, and 12 degrees. The Reynolds number is 3.1×10^6.

■ **Solution**

The lift-to-drag ratio, L/D, is given by

$$\frac{L}{D} = \frac{q_\infty S c_\ell}{q_\infty S c_d} = \frac{c_\ell}{c_d}$$

From Figures 4.10 and 4.11, we have

α	C_ℓ	C_d	C_ℓ/C_d
0	0.25	0.0065	38.5
4	0.65	0.0070	93
8	1.08	0.0112	96
12	1.44	0.017	85

Note that, as the angle of attack increases, the lift-to-drag ratio first increases, reaches a maximum, and then decreases. The maximum lift-to-drag ratio, $(L/D)_{max}$, is an important parameter in airfoil performance; it is a direct measure of aerodynamic efficiency. The higher the value of $(L/D)_{max}$, the more efficient is the airfoil. The values of L/D for airfoils are quite large numbers in comparison to that for a complete airplane. Due to the extra drag associated with all parts of the airplane, values of $(L/D)_{max}$ for real airplanes are on the order of 10 to 20.

4.4 PHILOSOPHY OF THEORETICAL SOLUTIONS FOR LOW-SPEED FLOW OVER AIRFOILS: THE VORTEX SHEET

In Section 3.14, the concept of vortex flow was introduced; refer to Figure 3.31 for a schematic of the flow induced by a point vortex of strength Γ located at a given point O. (Recall that Figure 3.31, with its counterclockwise flow, corresponds to a negative value of Γ. By convention, a positive Γ induces a clockwise flow.) Let us now expand our concept of a point vortex. Referring to Figure 3.31, imagine a straight line perpendicular to the page, going through point O, and extending to infinity both out of and into the page. This line is a straight *vortex filament* of strength Γ. A straight vortex filament is drawn in perspective in Figure 4.12. (Here, we show a clockwise flow, which corresponds to a positive value of Γ.) The flow induced in any plane perpendicular to the straight vortex filament by the filament itself is identical to that induced by a point vortex of strength Γ; that is, in Figure 4.12, the flows in the planes perpendicular to the vortex filament at O and O' are identical to each other and are identical to the flow induced by a point vortex of strength Γ. Indeed, the point vortex described in Section 3.14 is simply a section of a straight vortex filament.

In Section 3.17, we introduced the concept of a source sheet, which is an infinite number of line sources side by side, with the strength of each line source being infinitesimally small. For vortex flow, consider an analogous situation. Imagine an infinite number of straight vortex filaments side by side, where the strength of each filament is infinitesimally small. These side-by-side vortex filaments form a *vortex sheet,* as shown in perspective in the upper left of Figure 4.13. If we look along the series of vortex filaments (looking along the y axis in Figure 4.13), the vortex sheet will appear as sketched at the lower right of Figure 4.13. Here, we are looking at an edge view of the sheet; the vortex filaments are all perpendicular
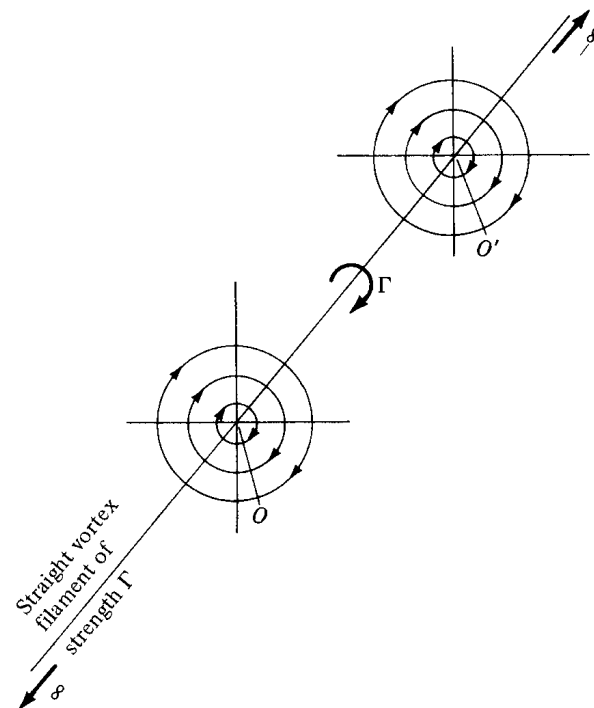
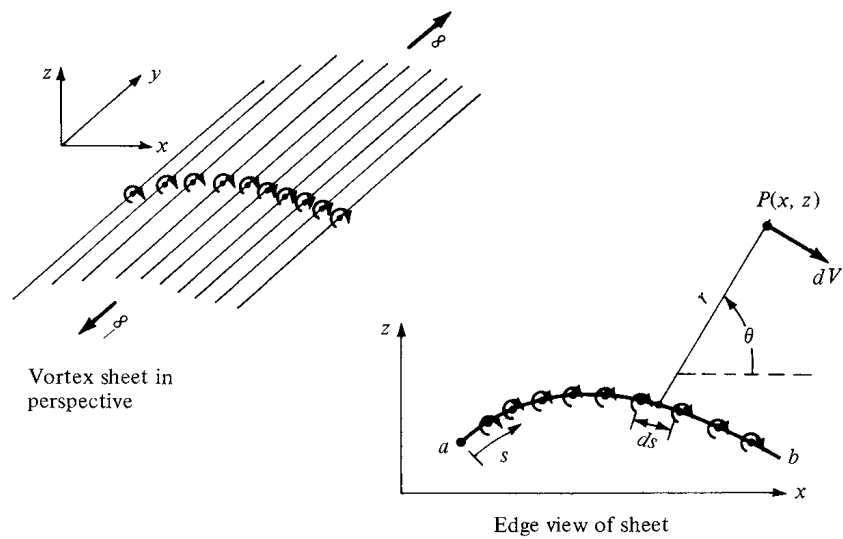**Figure 4.12** Vortex filament.

Figure 4.13 Vortex sheet.

to the page. Let s be the distance measured along the vortex sheet in the edge view. Define $\gamma = \gamma(s)$ as the strength of the vortex sheet, per unit length along s. Thus, the strength of an infinitesimal portion ds of the sheet is $\gamma\,ds$. This small section of the vortex sheet can be treated as a distinct vortex of strength $\gamma\,ds$. Now consider point P in the flow, located a distance r from ds; the Cartesian coordinates of P are (x, z). The small section of the vortex sheet of strength $\gamma\,ds$ induces an infinitesimally small velocity dV at point P. From Equation (3.105), dV is given by

$$dV = -\frac{\gamma\,ds}{2\pi r} \tag{4.1}$$

and is in a direction perpendicular to r, as shown in Figure 4.13. The velocity at P induced by the entire vortex sheet is the summation of Equation (4.1) from point a to point b. Note that dV, which is perpendicular to r, changes direction at point P as we sum from a to b; hence, the incremental velocities induced at P by different sections of the vortex sheet must be added vectorally. Because of this, it is sometimes more convenient to deal with the velocity potential. Again referring to Figure 4.13, the increment in velocity potential $d\phi$ induced at point P by the elemental vortex $\gamma\,ds$ is, from Equation (3.112),

$$d\phi = -\frac{\gamma\,ds}{2\pi}\theta \tag{4.2}$$

In turn, the velocity potential at P due to the entire vortex sheet from a to b is

$$\boxed{\phi(x, z) = -\frac{1}{2\pi}\int_a^b \theta\gamma\,ds} \tag{4.3}$$

Equation (4.1) is particularly useful for our discussion of classical thin airfoil theory, whereas Equation (4.3) is important for the numerical vortex panel method.

Recall from Section 3.14 that the circulation Γ around a point vortex is equal to the strength of the vortex. Similarly, the circulation around the vortex sheet in Figure 4.13 is the sum of the strengths of the elemental vortices; that is

$$\boxed{\Gamma = \int_a^b \gamma\,ds} \tag{4.4}$$

Recall that the source sheet introduced in Section 3.17 has a discontinuous change in the direction of the *normal* component of velocity across the sheet (from Figure 3.38, note that the normal component of velocity changes direction by 180° in crossing the sheet), whereas the tangential component of velocity is the same immediately above and below the source sheet. In contrast, for a vortex sheet, there is a discontinuous change in the tangential component of velocity across the sheet, whereas the normal component of velocity is preserved across the sheet. This change in tangential velocity across the vortex sheet is related to the strength of the sheet as follows. Consider a vortex sheet as sketched in
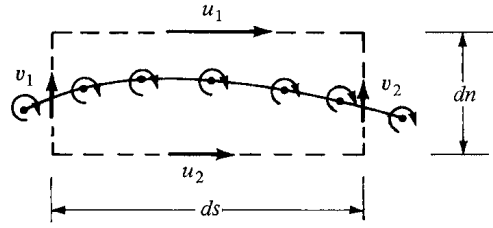
Figure 4.14 Tangential velocity jump across a
vortex sheet.

Figure 4.14. Consider the rectangular dashed path enclosing a section of the
sheet of length ds. The velocity components tangential to the top and bottom
of this rectangular path are u_1 and u_2, respectively, and the velocity components
tangential to the left and right sides are v_1 and v_2, respectively. The top and bottom
of the path are separated by the distance dn. From the definition of circulation
given by Equation (2.136), the circulation around the dashed path is

$$\Gamma = -(v_2\, dn - u_1\, ds - v_1\, dn + u_2\, ds)$$

or $$\Gamma = (u_1 - u_2)\, ds + (v_1 - v_2)\, dn \tag{4.5}$$

However, since the strength of the vortex sheet contained inside the dashed path
is $\gamma\, ds$, we also have

$$\Gamma = \gamma\, ds \tag{4.6}$$

Therefore, from Equations (4.5) and (4.6),

$$\gamma\, ds = (u_1 - u_2)\, ds + (v_1 - v_2)\, dn \tag{4.7}$$

Let the top and bottom of the dashed line approach the vortex sheet; that is, let
$dn \rightarrow 0$. In the limit, u_1 and u_2 become the velocity components tangential
to the vortex sheet immediately above and below the sheet, respectively, and
Equation (4.7) becomes

$$\gamma\, ds = (u_1 - u_2)\, ds$$

or $$\boxed{\gamma = u_1 - u_2} \tag{4.8}$$

Equation (4.8) is important; it states that *the local jump in tangential velocity
across the vortex sheet is equal to the local sheet strength.*

We have now defined and discussed the properties of a vortex sheet. The con-
cept of a vortex sheet is instrumental in the analysis of the low-speed characteris-
tics of an airfoil. A philosophy of airfoil theory of inviscid, incompressible flow
is as follows. Consider an airfoil of arbitrary shape and thickness in a freestream
with velocity V_∞, as sketched in Figure 4.15. Replace the airfoil surface with a
vortex sheet of variable strength $\gamma(s)$, as also shown in Figure 4.15. Calculate
the variation of γ as a function of s such that the induced velocity field from
the vortex sheet when added to the uniform velocity of magnitude V_∞ will make
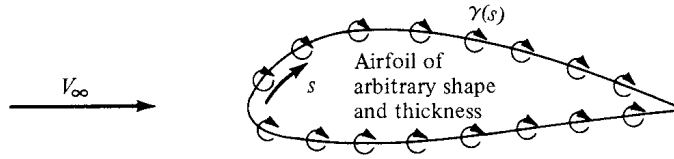
Figure 4.15 Simulation of an arbitrary airfoil by distributing a vortex sheet over the airfoil surface.

the vortex sheet (hence the airfoil surface) a *streamline of the flow*. In turn, the circulation around the airfoil will be given by

$$\Gamma = \int \gamma \, ds$$

where the integral is taken around the complete surface of the airfoil. Finally, the resulting lift is given by the Kutta-Joukowski theorem:

$$L' = \rho_\infty V_\infty \Gamma$$

This philosophy is not new. It was first espoused by Ludwig Prandtl and his colleagues at Göttingen, Germany, during the period 1912–1922. However, no general analytical solution for $\gamma = \gamma(s)$ exists for an airfoil of arbitrary shape and thickness. Rather, the strength of the vortex sheet must be found numerically, and the practical implementation of the above philosophy had to wait until the 1960s with the advent of large digital computers. Today, the above philosophy is the foundation of the modern vortex panel method, to be discussed in Section 4.9.

The concept of replacing the airfoil surface in Figure 4.15 with a vortex sheet is more than just a mathematical device; it also has physical significance. In real life, there is a thin boundary layer on the surface, due to the action of friction between the surface and the airflow (see Figures 1.41 and 1.46). This boundary layer is a highly viscous region in which the large velocity gradients produce substantial vorticity; that is, $\nabla \times \mathbf{V}$ is finite within the boundary layer. (Review Section 2.12 for a discussion of vorticity.) Hence, in real life, there is a distribution of vorticity along the airfoil surface due to viscous effects, and our philosophy of replacing the airfoil surface with a vortex sheet (such as in Figure 4.15) can be construed as a way of modeling this effect in an inviscid flow.[3]

Imagine that the airfoil in Figure 4.15 is made very thin. If you were to stand back and look at such a thin airfoil from a distance, the portions of the vortex sheet

---

[3] It is interesting to note that some recent research by NASA is hinting that even as complex a problem as flow separation, heretofore thought to be a completely viscous-dominated phenomenon, may in reality be an inviscid-dominated flow which requires only a rotational flow. For example, some inviscid flow-field numerical solutions for flow over a circular cylinder, when vorticity is introduced either by means of a nonuniform freestream or a curved shock wave, are accurately predicting the separated flow on the rearward side of the cylinder. However, as exciting as these results may be, they are too preliminary to be emphasized in this book. We continue to talk about flow separation in Chapters 15 to 20 as being a viscous-dominated effect, until definitely proved otherwise. This recent research is mentioned here only as another example of the physical connection between vorticity, vortex sheets, viscosity, and real life.
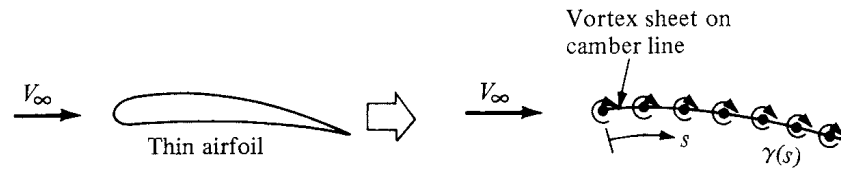
Figure 4.16 Thin airfoil approximation.

on the top and bottom surface of the airfoil would almost coincide. This gives rise to a method of approximating a thin airfoil by replacing it with a single vortex sheet distributed over the camber line of the airfoil, as sketched in Figure 4.16. The strength of this vortex sheet $\gamma(s)$ is calculated such that, in combination with the freestream, the camber line becomes a streamline of the flow. Although the approach shown in Figure 4.16 is approximate in comparison with the case shown in Figure 4.15, it has the advantage of yielding a closed-form analytical solution. This philosophy of thin airfoil theory was first developed by Max Munk, a colleague of Prandtl, in 1922 (see Reference 12). It is discussed in Sections 4.7 and 4.8.

4.5 THE KUTTA CONDITION

The lifting flow over a circular cylinder was discussed in Section 3.15, where we observed that an infinite number of potential flow solutions were possible, corresponding to the infinite choice of Γ. For example, Figure 3.33 illustrates three different flows over the cylinder, corresponding to three different values of Γ. The same situation applies to the potential flow over an airfoil; for a given airfoil at a given angle of attack, there are an infinite number of valid theoretical solutions, corresponding to an infinite choice of Γ. For example, Figure 4.17 illustrates two different flows over the same airfoil at the same angle of attack but with different values of Γ. At first, this may seem to pose a dilemma. We know from experience that a given airfoil at a given angle of attack produces a single value of lift (e.g., see Figure 4.10). So, although there is an infinite number of possible potential flow solutions, nature knows how to pick a particular solution. Clearly, the philosophy discussed in the previous section is not complete—we need an additional condition that *fixes* Γ for a given airfoil at a given α.

To attempt to find this condition, let us examine some experimental results for the development of the flow field around an airfoil which is set into motion from an initial state of rest. Figure 4.18 shows a series of classic photographs of the flow over an airfoil, taken from Prandtl and Tietjens (Reference 8). In Figure 4.18*a*, the flow has just started, and the flow pattern is just beginning to develop around the airfoil. In these early moments of development, the flow tries to curl around the sharp trailing edge from the bottom surface to the top surface, similar to the sketch shown at the left of Figure 4.17. However, more advanced considerations of inviscid, incompressible flow (see, e.g., Reference 9) show the theoretical result that the velocity becomes infinitely large at a sharp corner. Hence, the type
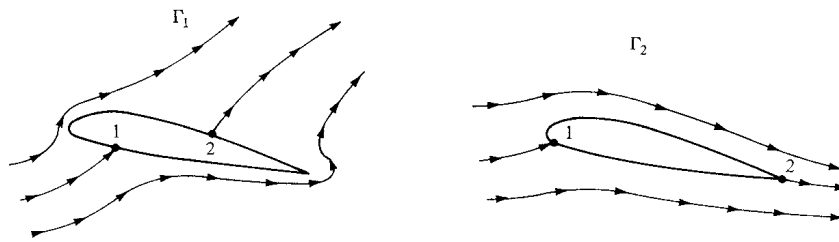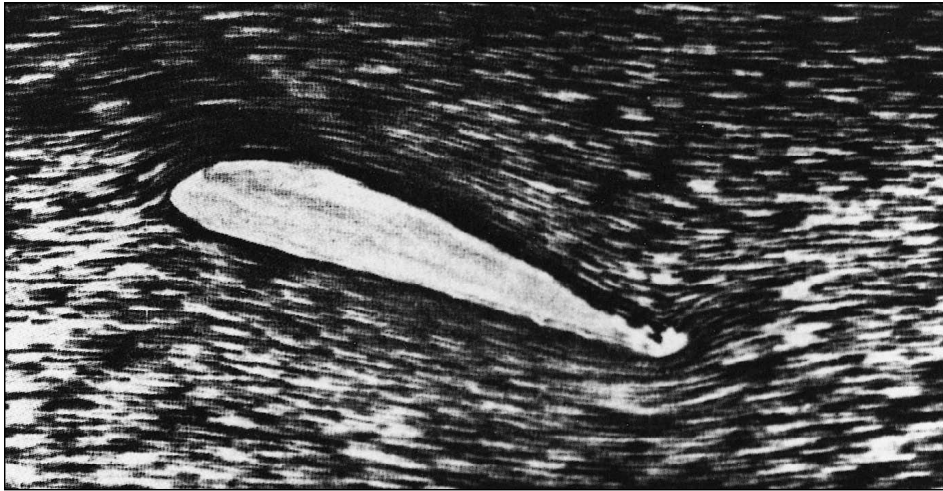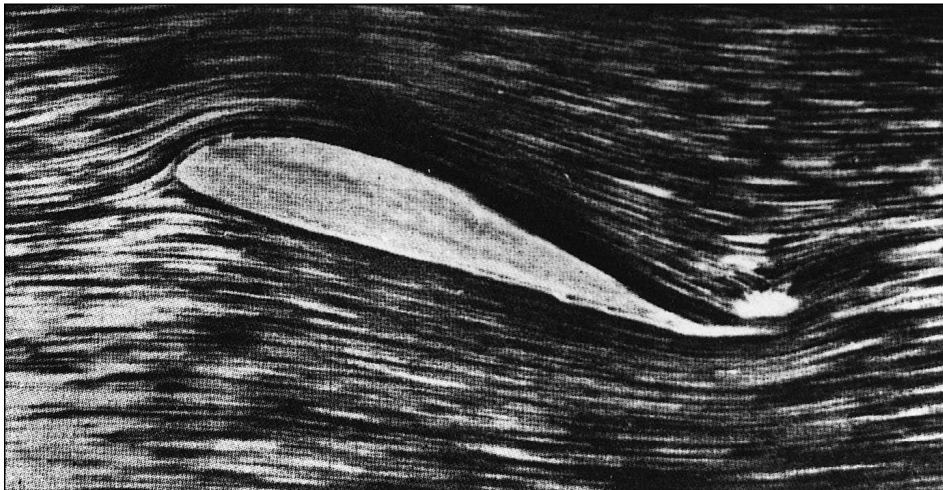
Figure 4.17 Effect of different values of circulation on the potential flow over a given airfoil at a given angle of attack. Points 1 and 2 are stagnation points.

(*a*)

(*b*)

Figure 4.18 The development of steady flow over an airfoil; the airfoil is impulsively started from rest and attains a steady velocity through the fluid. (*a*) A moment just after starting. (*b*) An intermediate time. *(Source: Prandtl and Tiejens, Reference 8.)*

(*c*)

Figure 4.18 (continued) The development of steady flow over an airfoil; the airfoil is impulsively started from rest and attains a steady velocity through the fluid. (*c*) The final steady flow. *(Source: Prandtl and Tiejens, Reference 8.)*

of flow sketched at the left of Figure 4.17, and shown in Figure 4.18*a*, is not tolerated very long by nature. Rather, as the real flow develops over the airfoil, the stagnation point on the upper surface (point 2 in Figure 4.17) moves toward the trailing edge. Figure 4.18*b* shows this intermediate stage. Finally, after the initial transient process dies out, the steady flow shown in Figure 4.18*c* is reached. This photograph demonstrates that the flow is *smoothly leaving the top and the bottom surfaces of the airfoil at the trailing edge*. This flow pattern is sketched at the right of Figure 4.17 and represents the type of pattern to be expected for the steady flow over an airfoil.

Reflecting on Figures 4.17 and 4.18, we emphasize again that in establishing the steady flow over a given airfoil at a given angle of attack, nature adopts that particular value of circulation (Γ_2 in Figure 4.17) which results in the flow leaving smoothly at the trailing edge. This observation was first made and used in a theoretical analysis by the German mathematician M. Wilhelm Kutta in 1902. Therefore, it has become known as the *Kutta condition*.

In order to apply the Kutta condition in a theoretical analysis, we need to be more precise about the nature of the flow at the trailing edge. The trailing edge can have a finite angle, as shown in Figures 4.17 and 4.18 and as sketched at the left of Figure 4.19, or it can be cusped, as shown at the right of Figure 4.19. First, consider the trailing edge with a finite angle, as shown at the left of Figure 4.19. Denote the velocities along the top surface and the bottom surface as V_1 and V_2, respectively. V_1 is parallel to the top surface at point *a*, and V_2 is parallel to the bottom surface at point *a*. For the finite-angle trailing edge, if these velocities were finite at point *a*, then we would have two velocities in two different directions at
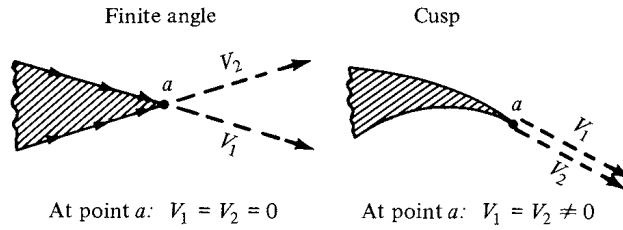
Figure 4.19 Different possible shapes of the trailing edge and their relation to the Kutta condition.

the same point, as shown at the left of Figure 4.19. However, this is not physically possible, and the only recourse is for both V_1 and V_2 to be zero at point a. That is, for the finite trailing edge, point a is a stagnation point, where $V_1 = V_2 = 0$. In contrast, for the cusped trailing edge shown at the right of Figure 4.19, V_1 and V_2 are in the same direction at point a, and hence both V_1 and V_2 can be finite. However, the pressure at point a, p_2, is a single, unique value, and Bernoulli's equation applied at both the top and bottom surfaces immediately adjacent to point a yields

$$p_a + \tfrac{1}{2}\rho V_1^2 = p_a + \tfrac{1}{2}\rho V_2^2$$

or
$$V_1 = V_2$$

Hence, for the cusped trailing edge, we see that the velocities leaving the top and bottom surfaces of the airfoil at the trailing edge are finite and equal in magnitude and direction.

We can summarize the statement of the Kutta condition as follows:

1. For a given airfoil at a given angle of attack, the value of Γ around the airfoil is such that the flow leaves the trailing edge smoothly.
2. If the trailing-edge angle is finite, then the trailing edge is a stagnation point.
3. If the trailing edge is cusped, then the velocities leaving the top and bottom surfaces at the trailing edge are finite and equal in magnitude and direction.

Consider again the philosophy of simulating the airfoil with vortex sheets placed either on the surface or on the camber line, as discussed in Section 4.4. The strength of such a vortex sheet is variable along the sheet and is denoted by $\gamma(s)$. The statement of the Kutta condition in terms of the vortex sheet is as follows. At the trailing edge (TE), from Equation (4.8), we have

$$\gamma(\text{TE}) = \gamma(a) = V_1 - V_2 \tag{4.9}$$

However, for the finite-angle trailing edge, $V_1 = V_2 = 0$; hence, from Equation (4.9), $\gamma(\text{TE}) = 0$. For the cusped trailing edge, $V_1 = V_2 \neq 0$; hence, from Equation (4.9), we again obtain the result that $\gamma(\text{TE}) = 0$. Therefore, the Kutta

condition expressed in terms of the strength of the vortex sheet is

$$\boxed{\gamma(\text{TE}) = 0} \qquad (4.10)$$

4.5.1 Without Friction Could We Have Lift?

In Section 1.5 we emphasized that the resultant aerodynamic force on a body immersed in a flow is due to the net integrated effect of the pressure and shear stress distributions over the body surface. Moreover, in Section 4.1 we noted that lift on an airfoil is primarily due to the surface pressure distribution, and that shear stress has virtually no effect on lift. It is easy to see why. Look at the airfoil shapes in Figures 4.17 and 4.18, for example. Recall that pressure acts *normal* to the surface, and for these airfoils the direction of this normal pressure is essentially in the vertical direction, that is, the lift direction. In contrast the shear stress acts *tangential* to the surface, and for these airfoils the direction of this tangential shear stress is mainly in the horizontal direction, that is, the drag direction. Hence, pressure is the dominant player in the generation of lift, and shear stress has a negligible effect on lift. It is for this reason that the lift on an airfoil below the stall can be accurately predicted by *inviscid* theories such as that discussed in this chapter.

However, if we lived in a perfectly inviscid world, an airfoil could not produce lift. Indeed, the presence of friction is the very reason why we have lift. These sound like strange, even contradictory statements to our discussion in the preceding paragraph. What is going on here? The answer is that in real life, the *way* that nature insures that the flow will leave smoothly at the trailing edge, that is, the mechanism that nature uses to choose the flow shown in Figure 4.18*c*, is that the viscous boundary layer remains attached to the surface all the way to the trailing edge. *Nature enforces the Kutta condition by means of friction*. If there were no boundary layer (i.e., no friction), there would be no physical mechanism in the real world to achieve the Kutta condition.

So we are led to the most ironic situation that lift, which is created by the surface pressure distribution—an inviscid phenomenon, would not exist in a frictionless (inviscid) world. In this regard, we can say that without friction we could not have lift. However, we say this in the informed manner as discussed above.

4.6 KELVIN'S CIRCULATION THEOREM AND THE STARTING VORTEX

In this section, we put the finishing touch to the overall philosophy of airfoil theory before developing the quantitative aspects of the theory itself in subsequent sections. This section also ties up a loose end introduced by the Kutta condition described in the previous section. Specifically, the Kutta condition states that the circulation around an airfoil is just the right value to ensure that the flow smoothly leaves the trailing edge. *Question:* How does nature generate this circulation?
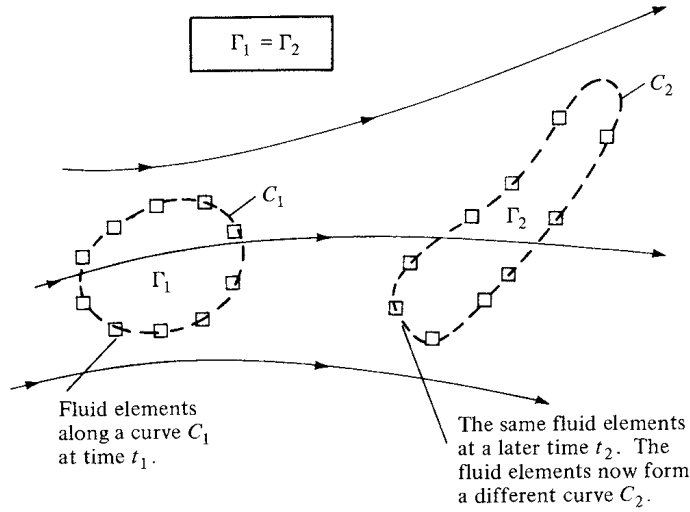
Figure 4.20 Kelvin's theorem.

Does it come from nowhere, or is circulation somehow conserved over the whole flow field? Let us examine these matters more closely.

Consider an arbitrary inviscid, incompressible flow as sketched in Figure 4.20. Assume that all body forces **f** are zero. Choose an arbitrary curve C_1 and identify the fluid elements that are on this curve at a given instant in time t_1. Also, by definition the circulation around curve C_1 is $\Gamma_1 = -\int_{C_1} \mathbf{V} \cdot \mathbf{ds}.$ Now let these specific fluid elements move downstream. At some later time, t_2, these *same* fluid elements will form another curve C_2, around which the circulation is $\Gamma_2 = -\int_{C_2} \mathbf{V} \cdot \mathbf{ds}.$ For the conditions stated above, we can readily show that $\Gamma_1 = \Gamma_2$. In fact, since we are following a set of specific fluid elements, we can state that circulation around a closed curve formed by a set of contiguous fluid elements remains constant as the fluid elements move throughout the flow. Recall from Section 2.9 that the substantial derivative gives the time rate of change following a given fluid element. Hence, a mathematical statement of the above discussion is simply

$$\frac{D\Gamma}{Dt} = 0 \qquad (4.11)$$

which says that the time rate of change of circulation around a closed curve consisting of the same fluid elements is zero. Equation (4.11) along with its supporting discussion is called *Kelvin's circulation theorem*.[4] Its derivation from

---

[4] Kelvin's theorem also holds for an inviscid compressible flow in the special case where $\rho = \rho(p)$; that is, the density is some single-valued function of pressure. Such is the case for isentropic flow, to be treated in later chapters.
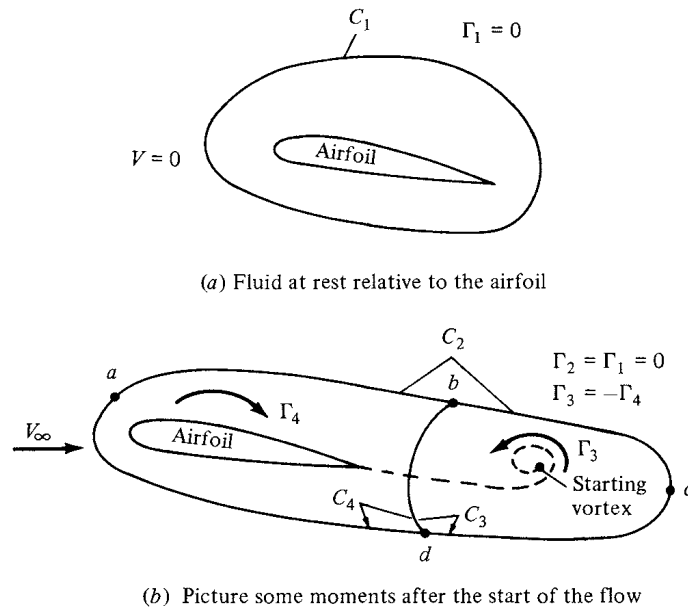
(*a*) Fluid at rest relative to the airfoil

(*b*) Picture some moments after the start of the flow

Figure 4.21 The creation of the starting vortex and the resulting generation of circulation around the airfoil.

first principles is left as Problem 4.3. Also, recall our definition and discussion of a vortex sheet in Section 4.4. An interesting consequence of Kelvin's circulation theorem is proof that a stream surface which is a vortex sheet at some instant in time remains a vortex sheet for all times.

Kelvin's theorem helps to explain the generation of circulation around an airfoil, as follows. Consider an airfoil in a fluid at rest, as shown in Figure 4.21*a*. Because $\mathbf{V} = 0$ everywhere, the circulation around curve C_1 is zero. Now start the flow in motion over the airfoil. Initially, the flow will tend to curl around the trailing edge, as explained in Section 4.5 and illustrated at the left of Figure 4.17. In so doing, the velocity at the trailing edge theoretically becomes infinite. In real life, the velocity tends toward a very large finite number. Consequently, during the very first moments after the flow is started, a thin region of very large velocity gradients (and therefore high vorticity) is formed at the trailing edge. This high-vorticity region is fixed to the same fluid elements, and consequently it is flushed downstream as the fluid elements begin to move downstream from the trailing edge. As it moves downstream, this thin sheet of intense vorticity is unstable, and it tends to roll up and form a picture similar to a point vortex. This vortex is called the *starting vortex* and is sketched in Figure 4.21*b*. After the flow around the airfoil has come to a steady state where the flow leaves the trailing edge smoothly (the Kutta condition), the high velocity gradients at the trailing edge disappear and vorticity

is no longer produced at that point. However, the starting vortex has already been formed during the starting process, and it moves steadily downstream with the flow forever after. Figure 4.21b shows the flow field sometime after steady flow has been achieved over the airfoil, with the starting vortex somewhere downstream. The fluid elements that initially made up curve C_1 in Figure 4.21a have moved downstream and now make up curve C_2, which is the complete circuit *abcda* shown in Figure 4.21b. Thus, from Kelvin's theorem, the circulation Γ_2 around curve C_2 (which encloses both the airfoil and the starting vortex) is the same as that around curve C_1, namely, zero. $\Gamma_2 = \Gamma_1 = 0$. Now let us subdivide C_2 into two loops by making the cut *bd*, thus forming curves C_3 (circuit *bcdb*) and C_4 (circuit *abda*). Curve C_3 encloses the starting vortex, and curve C_4 encloses the airfoil. The circulation Γ_3 around curve C_3 is due to the starting vortex; by inspecting Figure 4.21b, we see that Γ_3 is in the counterclockwise direction (i.e., a negative value). The circulation around curve C_4 enclosing the airfoil is Γ_4. Since the cut *bd* is common to both C_3 and C_4, the sum of the circulations around C_3 and C_4 is simply equal to the circulation around C_2:

$$\Gamma_3 + \Gamma_4 = \Gamma_2$$

However, we have already established that $\Gamma_2 = 0$. Hence,

$$\Gamma_4 = -\Gamma_3$$

that is, the circulation around the airfoil is equal and opposite to the circulation around the starting vortex.

This brings us to the summary as well as the crux of this section. As the flow over an airfoil is started, the large velocity gradients at the sharp trailing edge result in the formation of a region of intense vorticity which rolls up downstream of the trailing edge, forming the starting vortex. This starting vortex has associated with it a counterclockwise circulation. Therefore, as an equal-and-opposite reaction, a clockwise circulation around the airfoil is generated. As the starting process continues, vorticity from the trailing edge is constantly fed into the starting vortex, making it stronger with a consequent larger counterclockwise circulation. In turn, the clockwise circulation around the airfoil becomes stronger, making the flow at the trailing edge more closely approach the Kutta condition, thus weakening the vorticity shed from the trailing edge. Finally, the starting vortex builds up to just the right strength such that the equal-and-opposite clockwise circulation around the airfoil leads to smooth flow from the trailing edge (the Kutta condition is exactly satisfied). When this happens, the vorticity shed from the trailing edge becomes zero, the starting vortex no longer grows in strength, and a steady circulation exists around the airfoil.

EXAMPLE 4.4

For the NACA 2412 airfoil at the conditions given in Example 4.1, calculate the strength of the steady-state starting vortex.

■ **Solution**

From the given conditions in Example 4.1,

$$L' = 1254 \text{ N/m}$$

$$V_\infty = 70 \text{ m/s}$$

$$\rho_\infty = 1.23 \text{ kg/m}^3$$

From the Kutta-Joukowski theorem, Equation (3.140),

$$L' = \rho_\infty V_\infty \Gamma$$

the circulation associated with the flow over the airfoil is

$$\Gamma = \frac{L'}{\rho_\infty V_\infty} = \frac{1254}{(1.23)(70)} = 14.56 \ \frac{\text{m}^2}{\text{s}}$$

Referring to Figure 4.21, the steady-state starting vortex has strength equal and opposite to the circulation around the airfoil. Hence,

$$\boxed{\text{Strength of starting vortex} = -14.56 \ \tfrac{\text{m}^2}{\text{s}}}$$

Note: For practical calculations in aerodynamics, an actual number for circulation is rarely needed. Circulation is a mathematical quantity defined by Equation (2.136), and it is an essential theoretical concept within the framework of the circulation theory of lift. For example, in Section 4.7, an analytical expression for circulation is derived as Equation (4.30), and then immediately inserted into the Kutta-Joukowski theorem, Equation (4.31), yielding a formula for the lift coefficient, Equation (4.33). Nowhere do we need to calculate an actual number for Γ. In the present example, however, the *strength* of the starting vortex is indeed given by its circulation, and hence to compare the strengths of various starting vortices, calculating numbers for Γ is relevant. Even this can be considered only an academic exercise. In this author's experience, no practical aerodynamic calculation requires the strength of a starting vortex. The starting vortex is simply a theoretical construct that is consistent with the generation of circulation around a lifting two-dimensional body.

4.7 CLASSICAL THIN AIRFOIL THEORY: THE SYMMETRIC AIRFOIL

Some experimentally observed characteristics of airfoils and a philosophy for the theoretical prediction of these characteristics have been discussed in the preceding sections. Referring to our chapter road map in Figure 4.7, we have now completed the central branch. In this section, we move to the right-hand branch of Figure 4.7, namely, a quantitative development of thin airfoil theory. The basic equations necessary for the calculation of airfoil lift and moments are established in this section, with an application to symmetric airfoils. The case of cambered airfoils will be treated in Section 4.8.

For the time being, we deal with *thin* airfoils; for such a case, the airfoil can be simulated by a vortex sheet placed along the camber line, as discussed in Section 4.4. Our purpose is to calculate the variation of $\gamma(s)$ such that the camber line becomes a streamline of the flow and such that the Kutta condition is satisfied at the trailing edge; that is, $\gamma(\text{TE}) = 0$ [see Equation (4.10)]. Once we have found the particular $\gamma(s)$ that satisfies these conditions, then the total circulation Γ around the airfoil is found by integrating $\gamma(s)$ from the leading edge to the trailing edge. In turn, the lift is calculated from Γ via the Kutta-Joukowski theorem.

Consider a vortex sheet placed on the camber line of an airfoil, as sketched in Figure 4.22a. The freestream velocity is V_∞, and the airfoil is at the angle of attack α. The x axis is oriented along the chord line, and the z axis is perpendicular to the chord. The distance measured along the camber line is denoted by s. The shape of the camber line is given by $z = z(x)$. The chord length is c. In Figure 4.22a, w' is the component of velocity normal to the camber line induced by the vortex sheet; $w' = w'(s)$. For a thin airfoil, we rationalized in Section 4.4 that the distribution of a vortex sheet over the surface of the airfoil, when viewed from a distance, looks almost the same as a vortex sheet placed on the camber line. Let us stand back once again and view Figure 4.22a from a distance. If the airfoil
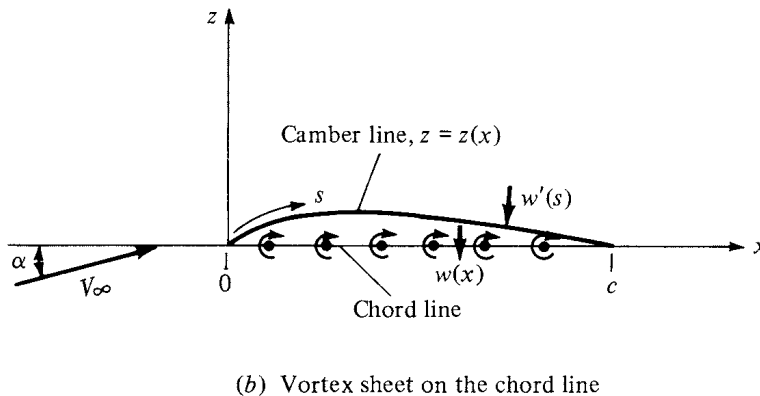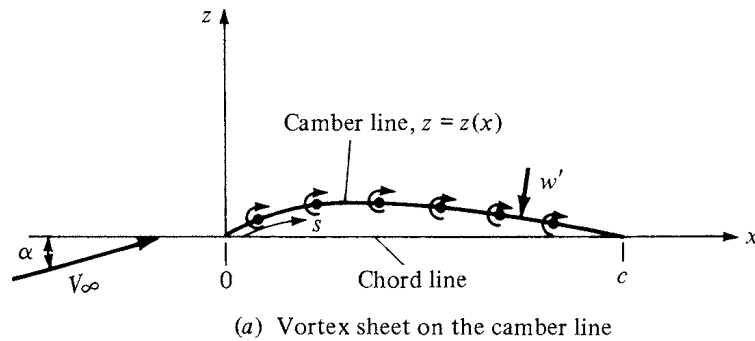

(*a*) Vortex sheet on the camber line

(*b*) Vortex sheet on the chord line

Figure 4.22 Placement of the vortex sheet for thin airfoil analysis.

is thin, the camber line is close to the chord line, and viewed from a distance, the vortex sheet appears to fall approximately on the chord line. Therefore, once again, let us reorient our thinking and place the vortex sheet on the chord line, as sketched in Figure 4.22b. Here, $\gamma = \gamma(x)$. We still wish the camber line to be a streamline of the flow, and $\gamma = \gamma(x)$ is calculated to satisfy this condition as well as the Kutta condition $\gamma(c) = 0$. That is, the strength of the vortex sheet on the chord line is determined such that the camber line (not the chord line) is a streamline.

For the camber line to be a streamline, the component of velocity normal to the camber line must be zero at all points along the camber line. The velocity at any point in the flow is the sum of the uniform freestream velocity and the velocity induced by the vortex sheet. Let $V_{\infty,n}$ be the component of the freestream velocity normal to the camber line. Thus, for the camber line to be a streamline,

$$V_{\infty,n} + w'(s) = 0 \qquad (4.12)$$

at every point along the camber line.

An expression for $V_{\infty,n}$ in Equation (4.12) is obtained by the inspection of Figure 4.23. At any point P on the camber line, where the slope of the camber line is dz/dx, the geometry of Figure 4.23 yields

$$V_{\infty,n} = V_\infty \sin\left[\alpha + \tan^{-1}\left(-\frac{dz}{dx}\right)\right] \qquad (4.13)$$

For a thin airfoil at small angle of attack, both α and $\tan^{-1}(-dz/dx)$ are small values. Using the approximation that $\sin\theta \approx \tan\theta \approx \theta$ for small θ, where θ is in
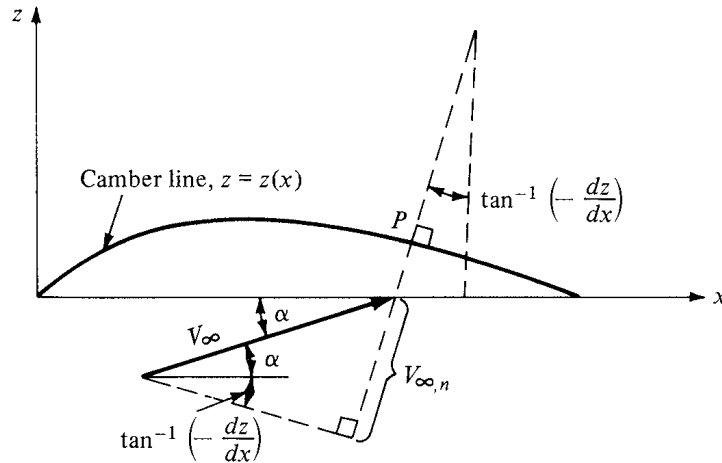

Figure 4.23 Determination of the component of freestream velocity normal to the camber line.

radians, Equation (4.13) reduces to

$$V_{\infty,n} = V_\infty \left(\alpha - \frac{dz}{dx} \right) \qquad (4.14)$$

Equation (4.14) gives the expression for $V_{\infty,n}$ to be used in Equation (4.12). Keep in mind that, in Equation (4.14), α is in radians.

Returning to Equation (4.12), let us develop an expression for $w'(s)$ in terms of the strength of the vortex sheet. Refer again to Figure 4.22*b*. Here, the vortex sheet is along the chord line, and $w'(s)$ is the component of velocity normal to the camber line induced by the vortex sheet. Let $w(x)$ denote the component of velocity normal to the *chord line* induced by the vortex sheet, as also shown in Figure 4.22*b*. If the airfoil is thin, the camber line is close to the chord line, and it is consistent with thin airfoil theory to make the approximation that

$$w'(s) \approx w(x) \qquad (4.15)$$

An expression for $w(x)$ in terms of the strength of the vortex sheet is easily obtained from Equation (4.1), as follows. Consider Figure 4.24, which shows the vortex sheet along the chord line. We wish to calculate the value of $w(x)$ at the location x. Consider an elemental vortex of strength $\gamma \, d\xi$ located at a distance ξ from the origin along the chord line, as shown in Figure 4.24. The strength of the vortex sheet γ varies with the distance along the chord; that is, $\gamma = \gamma(\xi)$. The velocity dw at point x induced by the elemental vortex at point ξ is given by Equation (4.1) as

$$dw = -\frac{\gamma(\xi) \, d\xi}{2\pi(x - \xi)} \qquad (4.16)$$

In turn, the velocity $w(x)$ induced at point x by *all* the elemental vortices along the chord line is obtained by integrating Equation (4.16) from the leading edge ($\xi = 0$) to the trailing edge ($\xi = c$):

$$w(x) = -\int_0^c \frac{\gamma(\xi) \, d\xi}{2\pi(x - \xi)} \qquad (4.17)$$

Combined with the approximation stated by Equation (4.15), Equation (4.17) gives the expression for $w'(s)$ to be used in Equation (4.12).
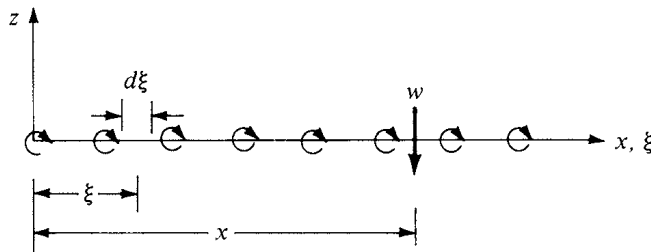

Figure 4.24 Calculation of the induced velocity at the chord line.

Recall that Equation (4.12) is the boundary condition necessary for the camber line to be a streamline. Substituting Equations (4.14), (4.15), and (4.17) into (4.12), we obtain

$$V_\infty \left(\alpha - \frac{dz}{dx} \right) - \int_0^c \frac{\gamma(\xi)\, d\xi}{2\pi(x - \xi)} = 0$$

or
$$\boxed{\frac{1}{2\pi} \int_0^c \frac{\gamma(\xi)\, d\xi}{x - \xi} = V_\infty \left(\alpha - \frac{dz}{dx} \right)} \tag{4.18}$$

the *fundamental equation of thin airfoil theory;* it is simply a statement that the camber line is a streamline of the flow.

Note that Equation (4.18) is written at a given point x on the chord line, and that dz/dx is evaluated at that point x. The variable ξ is simply a dummy variable of integration which varies from 0 to c along the chord line, as shown in Figure 4.24. The vortex strength $\gamma = \gamma(\xi)$ is a variable along the chord line. For a given airfoil at a given angle of attack, both α and dz/dx are known values in Equation (4.18). Indeed, the only unknown in Equation (4.18) is the vortex strength $\gamma(\xi)$. Hence, Equation (4.18) is an integral equation, the solution of which yields the variation of $\gamma(\xi)$ such that the camber line is a streamline of the flow. The central problem of thin airfoil theory is to solve Equation (4.18) for $\gamma(\xi)$, subject to the Kutta condition, namely, $\gamma(c) = 0$.

In this section, we treat the case of a symmetric airfoil. As stated in Section 4.2, a symmetric airfoil has no camber; the camber line is coincident with the chord line. Hence, for this case, $dz/dx = 0$, and Equation (4.18) becomes

$$\frac{1}{2\pi} \int_0^c \frac{\gamma(\xi)\, d\xi}{x - \xi} = V_\infty \alpha \tag{4.19}$$

In essence, within the framework of thin airfoil theory, a symmetric airfoil is treated the same as a flat plate; note that our theoretical development does not account for the airfoil thickness distribution. Equation (4.19) is an *exact* expression for the inviscid, incompressible flow over a flat plate at a small angle of attack.

To help deal with the integral in Equations (4.18) and (4.19), let us transform ξ into θ via the following transformation:

$$\xi = \frac{c}{2}(1 - \cos\theta) \tag{4.20}$$

Since x is a fixed point in Equations (4.18) and (4.19), it corresponds to a particular value of θ, namely, θ_0, such that

$$x = \frac{c}{2}(1 - \cos\theta_0) \tag{4.21}$$

Also, from Equation (4.20),

$$d\xi = \frac{c}{2} \sin\theta\, d\theta \tag{4.22}$$

Substituting Equations (4.20) to (4.22) into (4.19), and noting that the limits of integration become $\theta = 0$ at the leading edge (where $\xi = 0$) and $\theta = \pi$ at the trailing edge (where $\xi = c$), we obtain

$$\frac{1}{2\pi} \int_0^\pi \frac{\gamma(\theta) \sin\theta \, d\theta}{\cos\theta - \cos\theta_0} = V_\infty \alpha \tag{4.23}$$

A rigorous solution of Equation (4.23) for $\gamma(\theta)$ can be obtained from the mathematical theory of integral equations, which is beyond the scope of this book. Instead, we simply state that the solution is

$$\boxed{\gamma(\theta) = 2\alpha V_\infty \frac{(1 + \cos\theta)}{\sin\theta}} \tag{4.24}$$

We can verify this solution by substituting Equation (4.24) into (4.23) yielding

$$\frac{1}{2\pi} \int_0^\pi \frac{\gamma(\theta) \sin\theta \, d\theta}{\cos\theta - \cos\theta_0} = \frac{V_\infty \alpha}{\pi} \int_0^\pi \frac{(1 + \cos\theta) \, d\theta}{\cos\theta - \cos\theta_0} \tag{4.25}$$

The following standard integral appears frequently in airfoil theory and is derived in Appendix E of Reference 9:

$$\int_0^\pi \frac{\cos n\theta \, d\theta}{\cos\theta - \cos\theta_0} = \frac{\pi \sin n\theta_0}{\sin\theta_0} \tag{4.26}$$

Using Equation (4.26) in the right-hand side of Equation (4.25), we find that

$$\frac{V_\infty \alpha}{\pi} \int_0^\pi \frac{(1 + \cos\theta) \, d\theta}{\cos\theta - \cos\theta_0} = \frac{V_\infty \alpha}{\pi} \left(\int_0^\pi \frac{d\theta}{\cos\theta - \cos\theta_0} + \int_0^\pi \frac{\cos\theta \, d\theta}{\cos\theta - \cos\theta_0} \right)$$

$$= \frac{V_\infty \alpha}{\pi}(0 + \pi) = V_\infty \alpha \tag{4.27}$$

Substituting Equation (4.27) into (4.25), we have

$$\frac{1}{2\pi} \int_0^\pi \frac{\gamma(\theta) \sin\theta \, d\theta}{\cos\theta - \cos\theta_0} = V_\infty \alpha$$

which is identical to Equation (4.23). Hence, we have shown that Equation (4.24) is indeed the solution to Equation (4.23). Also, note that at the trailing edge, where $\theta = \pi$, Equation (4.24) yields

$$\gamma(\pi) = 2\alpha V_\infty \frac{0}{0}$$

which is an indeterminant form. However, using L'Hospital's rule on Equation (4.24),

$$\gamma(\pi) = 2\alpha V_\infty \frac{-\sin\pi}{\cos\pi} = 0$$

Thus, Equation (4.24) also satisfies the Kutta condition.

We are now in a position to calculate the lift coefficient for a thin, symmetric airfoil. The total circulation around the airfoil is

$$\Gamma = \int_0^c \gamma(\xi)\, d\xi \tag{4.28}$$

Using Equations (4.20) and (4.22), Equation (4.28) transforms to

$$\Gamma = \frac{c}{2} \int_0^\pi \gamma(\theta) \sin\theta\, d\theta \tag{4.29}$$

Substituting Equation (4.24) into (4.29), we obtain

$$\Gamma = \alpha c V_\infty \int_0^\pi (1 + \cos\theta)\, d\theta = \pi \alpha c V_\infty \tag{4.30}$$

Substituting Equation (4.30) into the Kutta-Joukowski theorem, we find that the lift per unit span is

$$L' = \rho_\infty V_\infty \Gamma = \pi \alpha c \rho_\infty V_\infty^2 \tag{4.31}$$

The lift coefficient is

$$c_l = \frac{L'}{q_\infty S} \tag{4.32}$$

where

$$S = c(1)$$

Substituting Equation (4.31) into (4.32), we have

$$c_l = \frac{\pi \alpha c \rho_\infty V_\infty^2}{\frac{1}{2} \rho_\infty V_\infty^2 c(1)}$$

or

$$\boxed{c_l = 2\pi\alpha} \tag{4.33}$$

and

$$\boxed{\text{Lift slope} = \frac{dc_l}{d\alpha} = 2\pi} \tag{4.34}$$

Equations (4.33) and (4.34) are important results; they state the theoretical re-sult that the lift coefficient is *linearly proportional to angle of attack,* which is supported by the experimental results discussed in Section 4.3. They also state that the theoretical lift slope is equal to 2π rad^{-1}, which is 0.11 degree^{-1}. The experimental lift coefficient data for an NACA 0012 symmetric airfoil are given in Figure 4.25; note that Equation (4.33) accurately predicts c_l over a large range of angle of attack. (The NACA 0012 airfoil section is commonly used on airplane tails and helicopter blades.)

The moment about the leading edge can be calculated as follows. Consider the elemental vortex of strength $\gamma(\xi)\,d\xi$ located a distance ξ from the leading edge, as sketched in Figure 4.26. The circulation associated with this elemental vortex is $d\Gamma = \gamma(\xi)\,d\xi$. In turn, the increment of lift dL contributed by the elemental vortex is $dL = \rho_\infty V_\infty\, d\Gamma$. This increment of lift creates a moment
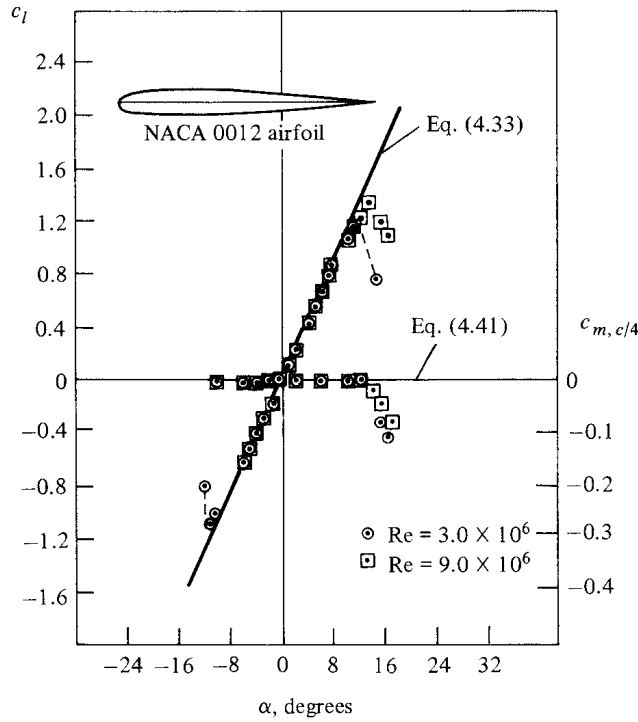
Figure 4.25 Comparison between theory and experiment for
the lift and moment coefficients for an NACA 0012 airfoil.
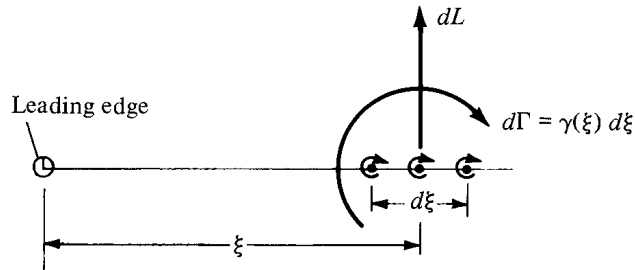*(Source: Abbott and von Doenhoff, Reference 11.)*

Figure 4.26 Calculation of moments about the leading edge.

about the leading edge $dM = -\xi(dL)$. The total moment about the leading edge
(LE) (per unit span) due to the entire vortex sheet is therefore

$$M'_{LE} = -\int_0^c \xi(dL) = -\rho_\infty V_\infty \int_0^c \xi\gamma(\xi)\,d\xi \qquad (4.35)$$

Transforming Equation (4.35) via Equations (4.20) and (4.22), and performing
the integration, we obtain (the details are left for Problem 4.4):

$$M'_{LE} = -q_\infty c^2 \frac{\pi\alpha}{2} \qquad (4.36)$$

The moment coefficient is

$$c_{m,\text{le}} = \frac{M'_{\text{LE}}}{q_\infty S c}$$

where $S = c(1)$. Hence,

$$c_{m,\text{le}} = \frac{M'_{\text{LE}}}{q_\infty c^2} = -\frac{\pi\alpha}{2} \tag{4.37}$$

However, from Equation (4.33),

$$\pi\alpha = \frac{c_l}{2} \tag{4.38}$$

Combining Equations (4.37) and (4.38), we obtain

$$\boxed{c_{m,\text{le}} = -\frac{c_l}{4}} \tag{4.39}$$

From Equation (1.22), the moment coefficient about the quarter-chord point is

$$c_{m,c/4} = c_{m,\text{le}} + \frac{c_l}{4} \tag{4.40}$$

Combining Equations (4.39) and (4.40), we have

$$\boxed{c_{m,c/4} = 0} \tag{4.41}$$

In Section 1.6, a definition is given for the center of pressure as that point about which the moments are zero. Clearly, Equation (4.41) demonstrates the theoretical result that the *center of pressure is at the quarter-chord point for a symmetric airfoil.*

By the definition given in Section 4.3, that point on an airfoil where moments are independent of angle of attack is called the aerodynamic center. From Equation (4.41), the moment about the quarter chord is zero for all values of α. Hence, for a symmetric airfoil, we have the theoretical result that the *quarter-chord point is both the center of pressure and the aerodynamic center.*

The theoretical result for $c_{m,c/4} = 0$ in Equation (4.41) is supported by the experimental data given in Figure 4.25. Also, note that the experimental value of $c_{m,c/4}$ is constant over a wide range of α, thus demonstrating that the real aerodynamic center is essentially at the quarter chord.

Let us summarize the above results. The essence of thin airfoil theory is to find a distribution of vortex sheet strength along the chord line that will make the camber line a streamline of the flow while satisfying the Kutta condition $\gamma(\text{TE}) = 0$. Such a vortex distribution is obtained by solving Equation (4.18) for $\gamma(\xi)$, or in terms of the transformed independent variable θ, solving Equation (4.23) for $\gamma(\theta)$ [recall that Equation (4.23) is written for a symmetric airfoil]. The resulting vortex distribution $\gamma(\theta)$ for a symmetric airfoil is given by Equation (4.24). In turn, this vortex distribution, when inserted into the Kutta-Joukowski theorem,

gives the following important theoretical results for a symmetric airfoil:

1. $c_l = 2\pi\alpha$.
2. Lift slope $= 2\pi$.
3. The center of pressure and the aerodynamic center are both located at the quarter-chord point.

Consider a thin flat plate at 5 deg. angle of attack. Calculate the: (*a*) lift coefficient, (*b*) moment coefficient about the leading edge, (*c*) moment coefficient about the quarter-chord point, and (*d*) moment coefficient about the trailing edge.

■ **Solution**

Recall that the results obtained in Section 4.7, although couched in terms of a thin symmetric airfoil, apply in particular to a flat plate with zero thickness.

(*a*) From Equation (4.33),

$$c_\ell = 2\pi\alpha$$

where α is in radians

$$\alpha = \frac{5}{57.3} = 0.0873\,\text{rad}$$

$$c_\ell = 2\pi(0.0873) = \boxed{0.5485}$$

(*b*) From Equation (4.39)

$$c_{m,\ell e} = -\frac{c_\ell}{4} = -\frac{0.5485}{4} = \boxed{-0.137}$$

(*c*) From Equation (4.41)

$$c_{m,c/4} = \boxed{0}$$

(*d*) Figure 4.27 is a sketch of the force and moment system on the plate. We place the lift at the quarter-chord point, along with the moment about the quarter-chord point.
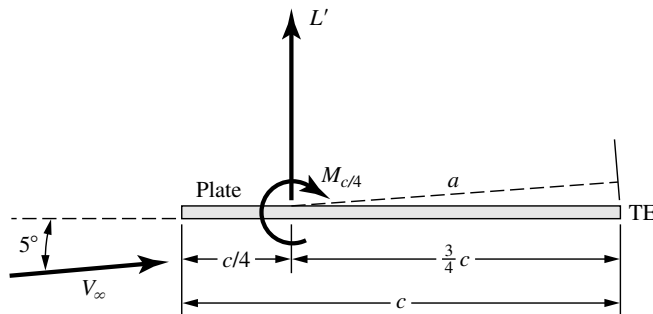

Figure 4.27 Flat plate at 5-degree angle of attack.

This represents the force and moment system on the plate. Recall from the discussion in Section 1.6 that the force and moment system can be represented by the lift acting through any point on the plate, and giving the moment about that point. Here, for convenience, we place the lift at the quarter-chord point.

The lift acts perpendicular to V_∞. (Part of the statement of the Kutta-Joukowski theorem given by Equation (3.140) is that the direction of the force associated with the circulation Γ is perpendicular to V_∞.) From Figure 4.27, the moment arm from L' to the trailing edge is the length a, where

$$a = \left(\tfrac{3}{4}c\right)\cos\alpha = \left(\tfrac{3}{4}c\right)\cos 5°$$

One of the assumptions of thin airfoil theory is that the angle of attack is small, and hence we can assume that $\cos\alpha \approx 1$. Therefore, the moment arm from the point of action of the lift to the trailing edge is reasonably given by $\tfrac{3}{4}c$. (Note that, in the previous Figure 4.26, the assumption of small α is already implicit because the moment arm is drawn parallel to the plate.)

Examining Figure 4.27, the moment about the trailing edge is

$$M'_{\text{te}} = \left(\frac{3}{4}c\right) L' + M'_{c/4}$$

$$c_{m,\text{te}} = \frac{M'_{\text{te}}}{q_\infty c^2} = \left(\frac{3}{4}c\right)\frac{L'}{q_\infty c^2} + \frac{M'_{c/4}}{q_\infty c^2}$$

$$c_{m,\text{te}} = \frac{3}{4}c_\ell + c_{m,c/4}$$

Since $\qquad c_{m,c/4} = 0$ we have

$$c_{m,\text{te}} = \frac{3}{4}c_\ell$$

$$c_{m,\text{te}} = \frac{3}{4}(0.5485) = \boxed{0.411}$$

4.8 THE CAMBERED AIRFOIL

Thin airfoil theory for a cambered airfoil is a generalization of the method for a symmetric airfoil discussed in Section 4.7. To treat the cambered airfoil, return to Equation (4.18):

$$\frac{1}{2\pi}\int_0^c \frac{\gamma(\xi)\,d\xi}{x-\xi} = V_\infty\left(\alpha - \frac{dz}{dx}\right) \tag{4.18}$$

For a cambered airfoil, dz/dx is finite, and this makes the analysis more elaborate than in the case of a symmetric airfoil, where $dz/dx = 0$. Once again, let us transform Equation (4.18) via Equations (4.20) to (4.22), obtaining

$$\frac{1}{2\pi}\int_0^\pi \frac{\gamma(\theta)\sin\theta\,d\theta}{\cos\theta - \cos\theta_0} = V_\infty\left(\alpha - \frac{dz}{dx}\right) \tag{4.42}$$

We wish to obtain a solution for $\gamma(\theta)$ from Equation (4.42), subject to the Kutta condition $\gamma(\pi) = 0$. Such a solution for $\gamma(\theta)$ will make the camber line a streamline of the flow. However, as before a rigorous solution of Equation (4.42) for $\gamma(\theta)$ is beyond the scope of this book. Rather, the result is stated below:

$$\gamma(\theta) = 2V_\infty \left(A_0 \frac{1 + \cos\theta}{\sin\theta} + \sum_{n=1}^{\infty} A_n \sin n\theta \right) \qquad (4.43)$$

Note that the above expression for $\gamma(\theta)$ consists of a leading term very similar to Equation (4.24) for a symmetric airfoil, plus a Fourier sine series with coefficients A_n. The values of A_n depend on the shape of the camber line dz/dx, and A_0 depends on both dz/dx and α, as shown below.

The coefficients A_0 and $A_n (n = 1, 2, 3, \ldots)$ in Equation (4.43) must be specific values in order that the camber line be a streamline of the flow. To find these specific values, substitute Equations (4.43) into Equation (4.42):

$$\frac{1}{\pi} \int_0^\pi \frac{A_0(1 + \cos\theta)\,d\theta}{\cos\theta - \cos\theta_0} + \frac{1}{\pi} \sum_{n=1}^{\infty} \int_0^\pi \frac{A_n \sin n\theta \sin\theta\,d\theta}{\cos\theta - \cos\theta_0} = \alpha - \frac{dz}{dx} \qquad (4.44)$$

The first integral can be evaluated from the standard form given in Equation (4.26). The remaining integrals can be obtained from another standard form, which is derived in Appendix E of Reference 9, and which is given below:

$$\int_0^\pi \frac{\sin n\theta \sin\theta\,d\theta}{\cos\theta - \cos\theta_0} = -\pi \cos n\theta_0 \qquad (4.45)$$

Hence, using Equations (4.26) and (4.45), we can reduce Equation (4.44) to

$$A_0 - \sum_{n=1}^{\infty} A_n \cos n\theta_0 = \alpha - \frac{dz}{dx}$$

or

$$\frac{dz}{dx} = (\alpha - A_0) + \sum_{n=1}^{\infty} A_n \cos n\theta_0 \qquad (4.46)$$

Recall that Equation (4.46) was obtained directly from Equation (4.42), which is the transformed version of the fundamental equation of thin airfoil theory, Equation (4.18). Furthermore, recall that Equation (4.18) is evaluated at a given point x along the chord line, as sketched in Figure 4.24. Hence, Equation (4.46) is also evaluated at the given point x; here, dz/dx and θ_0 correspond to the same point x on the chord line. Also, recall that dz/dx is a function of θ_0, where $x = (c/2)(1 - \cos\theta_0)$ from Equation (4.21).

Examine Equation (4.46) closely. It is in the form of a Fourier cosine series expansion for the function of dz/dx. In general, the Fourier cosine series representation of a function $f(\theta)$ over an interval $0 \le \theta \le \pi$ is given by

$$f(\theta) = B_0 + \sum_{n=1}^{\infty} B_n \cos n\theta \qquad (4.47)$$

where, from Fourier analysis, the coefficients B_0 and B_n are given by

$$B_0 = \frac{1}{\pi} \int_0^\pi f(\theta)\, d\theta \tag{4.48}$$

and

$$B_n = \frac{2}{\pi} \int_0^\pi f(\theta) \cos n\theta\, d\theta \tag{4.49}$$

(See, e.g., page 217 of Reference 6.) In Equation (4.46), the function dz/dx is analogous to $f(\theta)$ in the general form given in Equation (4.47). Thus, from Equations (4.48) and (4.49), the coefficients in Equation (4.46) are given by

$$\alpha - A_0 = \frac{1}{\pi} \int_0^\pi \frac{dz}{dx}\, d\theta_0$$

or

$$A_0 = \alpha - \frac{1}{\pi} \int_0^\pi \frac{dz}{dx}\, d\theta_0 \tag{4.50}$$

and

$$A_n = \frac{2}{\pi} \int_0^\pi \frac{dz}{dx} \cos n\theta_0\, d\theta_0 \tag{4.51}$$

Keep in mind that in the above, dz/dx is a function of θ_0. Note from Equation (4.50) that A_0 depends on both α and the shape of the camber line (through dz/dx), whereas from Equation (4.51) the values of A_n depend only on the shape of the camber line.

Pause for a moment and think about what we have done. We are considering the flow over a cambered airfoil of given shape dz/dx at a given angle of attack α. In order to make the camber line a streamline of the flow, the strength of the vortex sheet along the chord line must have the distribution $\gamma(\theta)$ given by Equation (4.43), where the coefficients A_0 and A_n are given by Equations (4.50) and (4.51), respectively. Also, note that Equation (4.43) satisfies the Kutta condition $\gamma(\pi) = 0$. Actual numbers for A_0 and A_n can be obtained for a given shape airfoil at a given angle of attack simply by carrying out the integrations indicated in Equations (4.50) and (4.51). For an example of such calculations applied to an NACA 23012 airfoil, see Example 4.5 at the end of this section. Also, note that when $dz/dx = 0$, Equation (4.43) reduces to Equation (4.24) for a symmetric airfoil. Hence, the symmetric airfoil is a special case of Equation (4.43).

Let us now obtain expressions for the aerodynamic coefficients for a cambered airfoil. The total circulation due to the entire vortex sheet from the leading edge to the trailing edge is

$$\Gamma = \int_0^c \gamma(\xi)\, d\xi = \frac{c}{2} \int_0^\pi \gamma(\theta) \sin \theta\, d\theta \tag{4.52}$$

Substituting Equation (4.43) for $\gamma(\theta)$ into Equation (4.52), we obtain

$$\Gamma = c V_\infty \left[A_0 \int_0^\pi (1 + \cos \theta)\, d\theta + \sum_{n=1}^\infty A_n \int_0^\pi \sin n\theta \sin \theta\, d\theta \right] \tag{4.53}$$

From any standard table of integrals,

$$\int_0^\pi (1 + \cos\theta)\, d\theta = \pi$$

and

$$\int_0^\pi \sin n\theta \sin\theta\, d\theta = \begin{cases} \pi/2 & \text{for } n = 1 \\ 0 & \text{for } n \neq 1 \end{cases}$$

Hence, Equation (4.53) becomes

$$\Gamma = cV_\infty \left(\pi A_0 + \frac{\pi}{2} A_1 \right) \tag{4.54}$$

From Equation (4.54), the lift per unit span is

$$L' = \rho_\infty V_\infty \Gamma = \rho_\infty V_\infty^2 c \left(\pi A_0 + \frac{\pi}{2} A_1 \right) \tag{4.55}$$

In turn, Equation (4.55) leads to the lift coefficient in the form

$$c_l = \frac{L'}{\frac{1}{2}\rho_\infty V_\infty^2 c(1)} = \pi(2A_0 + A_1) \tag{4.56}$$

Recall that the coefficients A_0 and A_1 in Equation (4.56) are given by Equations (4.50) and (4.51), respectively. Hence, Equation (4.56) becomes

$$\boxed{c_l = 2\pi \left[\alpha + \frac{1}{\pi} \int_0^\pi \frac{dz}{dx} (\cos\theta_0 - 1)\, d\theta_0 \right]} \tag{4.57}$$

and

$$\boxed{\text{Lift slope} \equiv \frac{dc_l}{d\alpha} = 2\pi} \tag{4.58}$$

Equations (4.57) and (4.58) are important results. Note that, as in the case of the symmetric airfoil, the theoretical lift slope for a cambered airfoil is 2π. It is a general result from thin airfoil theory that $dc_l/d\alpha = 2\pi$ for any shape airfoil. However, the expression for c_l itself differs between a symmetric and a cambered airfoil, the difference being the integral term in Equation (4.57). This integral term has physical significance, as follows. Return to Figure 4.9, which illustrates the lift curve for an airfoil. The angle of zero lift is denoted by $\alpha_{L=0}$ and is a negative value. From the geometry shown in Figure 4.9, clearly

$$c_l = \frac{dc_l}{d\alpha} (\alpha - \alpha_{L=0}) \tag{4.59}$$

Substituting Equation (4.58) into (4.59), we have

$$c_l = 2\pi(\alpha - \alpha_{L=0}) \tag{4.60}$$

Comparing Equations (4.60) and (4.57), we see that the integral term in Equation (4.57) is simply the negative of the zero-lift angle; that is

$$\alpha_{L=0} = -\frac{1}{\pi} \int_0^\pi \frac{dz}{dx} (\cos\theta_0 - 1)\, d\theta_0 \qquad (4.61)$$

Hence, from Equation (4.61), thin airfoil theory provides a means to predict the angle of zero lift. Note that Equation (4.61) yields $\alpha_{L=0} = 0$ for a symmetric airfoil, which is consistent with the results shown in Figure 4.25. Also, note that the more highly cambered the airfoil, the larger will be the absolute magnitude of $\alpha_{L=0}$.

Returning to Figure 4.26, the moment about the leading edge can be obtained by substituting $\gamma(\theta)$ from Equation (4.43) into the transformed version of Equation (4.35). The details are left for Problem 4.9. The result for the moment coefficient is

$$c_{m,\text{le}} = -\frac{\pi}{2}\left(A_0 + A_1 - \frac{A_2}{2}\right) \qquad (4.62)$$

Substituting Equation (4.56) into (4.62), we have

$$c_{m,\text{le}} = -\left[\frac{c_l}{4} + \frac{\pi}{4}(A_1 - A_2)\right] \qquad (4.63)$$

Note that, for $dz/dx = 0$, $A_1 = A_2 = 0$ and Equation (4.63) reduces to Equation (4.39) for a symmetric airfoil.

The moment coefficient about the quarter chord can be obtained by substituting Equation (4.63) into (4.40), yielding

$$c_{m,c/4} = \frac{\pi}{4}(A_2 - A_1) \qquad (4.64)$$

Unlike the symmetric airfoil, where $c_{m,c/4} = 0$, Equation (4.64) demonstrates that $c_{m,c/4}$ is finite for a cambered airfoil. Therefore, the quarter chord is *not* the center of pressure for a cambered airfoil. However, note that A_1 and A_2 depend only on the shape of the camber line and do not involve the angle of attack. Hence, from Equation (4.64), $c_{m,c/4}$ is *independent* of α. Thus, the quarter-chord point is the *theoretical location* of the aerodynamic center for a cambered airfoil.

The location of the center of pressure can be obtained from Equation (1.21):

$$x_{\text{cp}} = -\frac{M'_{\text{LE}}}{L'} = -\frac{c_{m,\text{le}}c}{c_l} \qquad (4.65)$$

Substituting Equation (4.63) into (4.65), we obtain

$$x_{\text{cp}} = \frac{c}{4}\left[1 + \frac{\pi}{c_l}(A_1 - A_2)\right] \qquad (4.66)$$

Equation (4.66) demonstrates that the center of pressure for a cambered airfoil varies with the lift coefficient. Hence, as the angle of attack changes, the center of pressure also changes. Indeed, as the lift approaches zero, x_{cp} moves toward infinity; that is, it leaves the airfoil. For this reason, the center of pressure is not always a convenient point at which to draw the force system on an airfoil. Rather, the force-and-moment system on an airfoil is more conveniently considered at the aerodynamic center. (Return to Figure 1.25 and the discussion at the end of Section 1.6 for the referencing of the force-and-moment system on an airfoil.)

EXAMPLE 4.6

Consider an NACA 23012 airfoil. The mean camber line for this airfoil is given by

$$\frac{z}{c} = 2.6595 \left[\left(\frac{x}{c}\right)^3 - 0.6075 \left(\frac{x}{c}\right)^2 + 0.1147 \left(\frac{x}{c}\right) \right] \qquad \text{for } 0 \le \frac{x}{c} \le 0.2025$$

and

$$\frac{z}{c} = 0.02208 \left(1 - \frac{x}{c}\right) \qquad \text{for } 0.2025 \le \frac{x}{c} \le 1.0$$

Calculate (*a*) the angle of attack at zero lift, (*b*) the lift coefficient when $\alpha = 4°$, (*c*) the moment coefficient about the quarter chord, and (*d*) the location of the center of pressure in terms of x_{cp}/c, when $\alpha = 4°$. Compare the results with experimental data.

■ **Solution**

We will need dz/dx. From the given shape of the mean camber line, this is

$$\frac{dz}{dx} = 2.6595 \left[3 \left(\frac{x}{c}\right)^2 - 1.215 \left(\frac{x}{c}\right) + 0.1147 \right] \qquad \text{for } 0 \le \frac{x}{c} \le 0.2025$$

and

$$\frac{dz}{dx} = -0.02208 \qquad \text{for } 0.2025 \le \frac{x}{c} \le 1.0$$

Transforming from x to θ, where $x = (c/2)(1 - \cos\theta)$, we have

$$\frac{dz}{dx} = 2.6595 \left[\frac{3}{4}(1 - 2\cos\theta + \cos^2\theta) - 0.6075(1 - \cos\theta) + 0.1147 \right]$$

or

$$= 0.6840 - 2.3736 \cos\theta + 1.995 \cos^2\theta \qquad \text{for } 0 \le \theta \le 0.9335 \text{ rad}$$

and

$$= -0.02208 \qquad \text{for } 0.9335 \le \theta \le \pi$$

(*a*) From Equation (4.61),

$$\alpha_{L=0} = -\frac{1}{\pi} \int_0^\pi \frac{dz}{dx}(\cos\theta - 1)\, d\theta$$

(*Note:* For simplicity, we have dropped the subscript zero from θ; in Equation (4.61), θ_0 is the variable of integration—it can just as well be symbolized as θ for the variable of integration.) Substituting the equation for dz/dx into Equation (4.61), we have

$$\alpha_{L=0} = -\frac{1}{\pi} \int_0^{0.9335} (-0.6840 + 3.0576 \cos\theta - 4.3686 \cos^2\theta + 1.995 \cos^3\theta)\, d\theta$$

(E.1)

$$-\frac{1}{\pi} \int_{0.9335}^\pi (0.02208 - 0.02208 \cos\theta)\, d\theta$$

From a table of integrals, we see that

$$\int \cos \theta \, d\theta = \sin \theta$$

$$\int \cos^2 \theta \, d\theta = \tfrac{1}{2} \sin \theta \cos \theta + \tfrac{1}{2}\theta$$

$$\int \cos^3 \theta \, d\theta = \tfrac{1}{3} \sin \theta (\cos^2 \theta + 2)$$

Hence, Equation (E.1) becomes

$$\alpha_{L=0} = -\frac{1}{\pi}[-2.8683\theta + 3.0576 \sin \theta - 2.1843 \sin \theta \cos \theta$$

$$+ 0.665 \sin \theta (\cos^2 \theta + 2)]_0^{0.9335}$$

$$- \frac{1}{\pi}[0.02208\theta - 0.02208 \sin \theta]_{0.9335}^{\pi}$$

Hence,

$$\alpha_{L=0} = -\frac{1}{\pi}(-0.0065 + 0.0665) = -0.0191 \text{ rad}$$

or

$$\boxed{\alpha_{L=0} = -1.09°}$$

(b) $\alpha = 4° = 0.0698$ rad
From Equation (4.60),

$$c_l = 2\pi(\alpha - \alpha_{L=0}) = 2\pi(0.0698 + 0.0191) = \boxed{0.559}$$

(c) The value of $c_{m,c/4}$ is obtained from Equation (4.64). For this, we need the two Fourier coefficients A_1 and A_2. From Equation (4.51),

$$A_1 = \frac{2}{\pi} \int_0^{\pi} \frac{dz}{dx} \cos \theta \, d\theta$$

$$A_1 = \frac{2}{\pi} \int_0^{0.9335} (0.6840 \cos \theta - 2.3736 \cos^2 \theta + 1.995 \cos^3 \theta) \, d\theta$$

$$+ \frac{2}{\pi} \int_{0.9335}^{\pi} (-0.02208 \cos \theta) \, d\theta$$

$$= \frac{2}{\pi}[0.6840 \sin \theta - 1.1868 \sin \theta \cos \theta - 1.1868\theta + 0.665 \sin \theta (\cos^2 \theta + 2)]_0^{0.9335}$$

$$+ \frac{2}{\pi}[-0.02208 \sin \theta]_{0.09335}^{\pi}$$

$$= \frac{2}{\pi}(0.1322 + 0.0177) = 0.0954$$

From Equation (4.51),

$$A_2 = \frac{2}{\pi} \int_0^\pi \frac{dz}{dx} \cos 2\theta \, d\theta = \frac{2}{\pi} \int_0^\pi \frac{dz}{dx}(2\cos^2\theta - 1) \, d\theta$$

$$= \frac{2}{\pi} \int_0^{0.9335} (-0.6840 + 2.3736\cos\theta - 0.627\cos^2\theta$$

$$- 4.747\cos^3\theta + 3.99\cos^4\theta) \, d\theta$$

$$+ \frac{2}{\pi} \int_{0.9335}^\pi (0.02208 - 0.0446\cos^2\theta) \, d\theta$$

Note:

$$\int \cos^4\theta \, d\theta = \tfrac{1}{4}\cos^3\theta\sin\theta + \tfrac{3}{8}(\sin\theta\cos\theta + \theta)$$

Thus,

$$A_2 = \frac{2}{\pi} \left\{ -0.6840\,\theta + 2.3736\sin\theta - 0.628\left(\frac{1}{2}\right)(\sin\theta\cos\theta + \theta) \right.$$

$$\left. - 4.747\left(\frac{1}{3}\right)\sin\theta(\cos^2\theta + 2) + 3.99\left[\frac{1}{4}\cos^3\sin\theta + \frac{3}{8}(\sin\theta\cos\theta + \theta)\right] \right\}_0^{0.9335}$$

$$+ \frac{2}{\pi} \left[0.02208\theta - 0.0446\left(\frac{1}{2}\right)(\sin\theta\cos\theta + \theta)\right]_{0.9335}^\pi$$

$$= \frac{2}{\pi}(0.11384 + 0.01056) = 0.0792$$

From Equation (4.64)

$$c_{m,c/4} = \frac{\pi}{4}(A_2 - A_1) = \frac{\pi}{4}(0.0792 - 0.0954)$$

$$\boxed{c_{m,c/4} = -0.0127}$$

(*d*) From Equation (4.66)

$$x_{cp} = \frac{c}{4}\left[1 + \frac{\pi}{c_l}(A_1 - A_2)\right]$$

Hence, $\dfrac{x_{cp}}{c} = \dfrac{1}{4}\left[1 + \dfrac{\pi}{0.559}(0.0954 - 0.0792)\right] = 0.273$

Comparison with Experimental Data   The data for the NACA 23012 airfoil are shown in Figure 4.28. From this, we make the following tabulation:

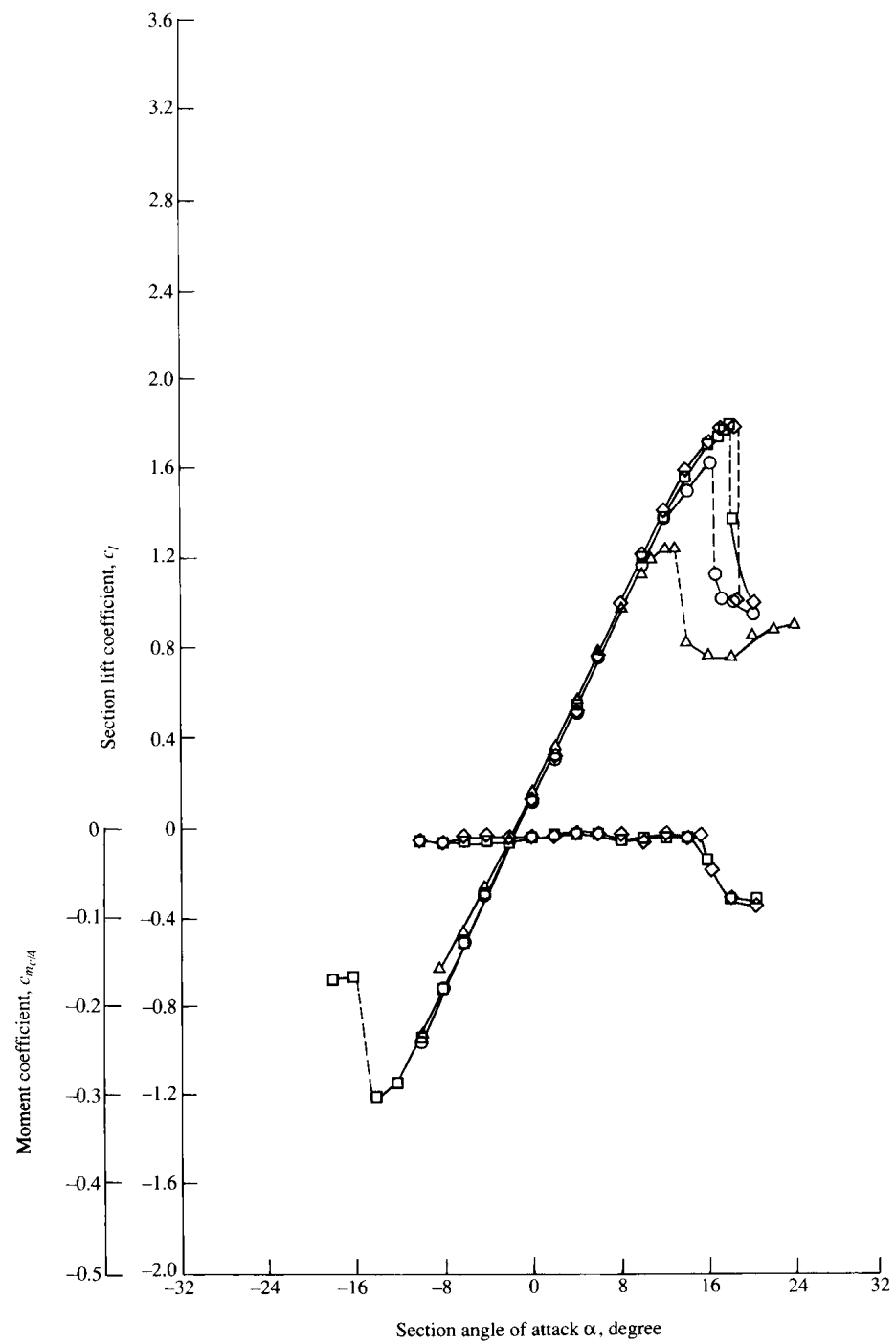|	Calculated	Experiment
$\alpha_{L=0}$	$-1.09°$	$-1.1°$
c_l (at $\alpha = 4°$)	0.559	0.55
$c_{m,c/4}$	-0.0127	-0.01

Figure 4.28 Lift- and moment-coefficient data for an NACA 23012 airfoil, for comparison with the theoretical results obtained in Example 4.6.

Note that the results from thin airfoil theory for a cambered airfoil agree very well with the experimental data. Recall that excellent agreement between thin airfoil theory for a symmetric airfoil and experimental data has already been shown in Figure 4.25. Hence, all of the work we have done in this section to develop thin airfoil theory is certainly worth the effort. Moreover, this illustrates that the development of thin airfoil theory in the early 1900s was a crowning achievement in theoretical aerodynamics and validates the mathematical approach of replacing the chord line of the airfoil with a vortex sheet, with the flow tangency condition evaluated along the mean camber line.

This brings to an end our introduction to classical thin airfoil theory. Returning to our road map in Figure 4.7, we have now completed the right-hand branch.

4.9 THE AERODYNAMIC CENTER: ADDITIONAL CONSIDERATIONS

The definition of the aerodynamic center is given in Section 4.3; it is that point on a body about which the aerodynamically generated moment is *independent of angle of attack*. At first thought, it is hard to imagine that such a point could exist. However, the moment coefficient data in Figure 4.11, which are constant with angle of attack, experimentally prove the existence of the aerodynamic center. Moreover, thin airfoil theory as derived in Sections 4.7 and 4.8 clearly shows that, within the assumptions embodied in the theory, not only does the aerodynamic center exist but that it is located at the quarter-chord point on the airfoil. Therefore, to Figure 1.24 which illustrates three different ways of stating the force and moment system on an airfoil, we can now add a fourth way, namely, the specification of the lift and drag acting through the aerodynamic center, and the value of the moment about the aerodynamic center. This is illustrated in Figure 4.29.

For most conventional airfoils, the aerodynamic center is close to, but not necessarily exactly at, the quarter-chord point. Given data for the shape of the
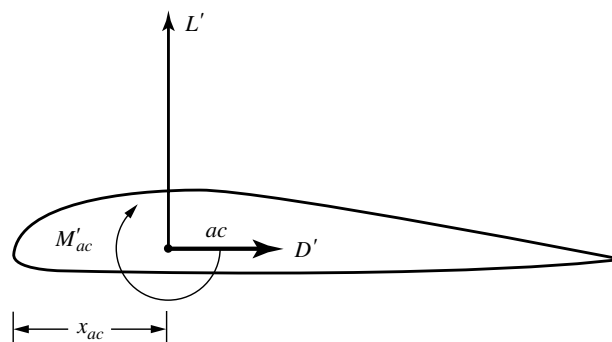

Figure 4.29 Lift, drag, and moments about the aerodynamic center.
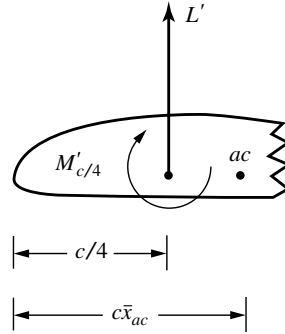
Figure 4.30 Lift and moments about the quarter-chord point, and a sketch useful for locating the aerodynamic center.

lift coefficient curve and the moment coefficient curve taken around an arbitrary point, we can calculate the location of the aerodynamic center as follows. Consider the lift and moment system taken about the quarter-chord point, as shown in Figure 4.30. We designate the location of the aerodynamic center by $c\bar{x}_{\rm ac}$ measured from the leading edge. Here, $\bar{x}_{\rm ac}$ is the location of the aerodynamic center as a fraction of the chord length c. Taking moments about the aerodynamic center designated by ac in Figure 4.30, we have

$$M'_{\rm ac} = L'(c\bar{x}_{\rm ac} - c/4) + M'_{c/4} \tag{4.67}$$

Dividing Equation (4.67) by $q_\infty Sc$, we have

$$\frac{M'_{\rm ac}}{q_\infty Sc} = \frac{L'}{q_\infty S}(\bar{x}_{\rm ac} - 0.25) + \frac{M'_{c/4}}{q_\infty Sc}$$

or
$$c_{m,{\rm ac}} = c_l(\bar{x}_{\rm ac} - 0.25) + c_{m,c/4} \tag{4.68}$$

Differentiating Equation (4.68) with respect to angle of attack α, we have

$$\frac{dc_{m,{\rm ac}}}{d\alpha} = \frac{dc_l}{d\alpha}(\bar{x}_{\rm ac} - 0.25) + \frac{dc_{m,c/4}}{d\alpha} \tag{4.69}$$

However, in Equation (4.69), $dc_{m,{\rm ac}}/d\alpha$ is zero by definition of the aerodynamic center. Hence, Equation (4.69) becomes

$$0 = \frac{dc_l}{d\alpha}(\bar{x}_{\rm ac} - 0.25) + \frac{dc_{m,c/4}}{d\alpha} \tag{4.70}$$

For airfoils below the stalling angle of attack, the slopes of the lift coefficient and moment coefficient curves are constant. Designating these slopes by

$$\frac{dc_l}{d\alpha} \equiv a_0; \qquad \frac{dc_{m,c/4}}{d\alpha} \equiv m_0$$

Equation (4.70) becomes

$$0 = a_0(\bar{x}_{ac} - 0.25) + m_0$$

or

$$\boxed{\bar{x}_{ac} = -\frac{m_0}{a_0} + 0.25}$$

(4.71)

Hence, Equation (4.71) proves that, for a body with linear lift and moment curves, that is, where a_0 and m_0 are fixed values, the aerodynamic center exists as a fixed point on the airfoil. Moreover, Equation (4.71) allows the calculation of the location of this point.

EXAMPLE 4.7

Consider the NACA 23012 airfoil studied in Example 4.6. Experimental data for this airfoil is plotted in Figure 4.28, and can be obtained from Reference 11. It shows that, at $\alpha = 4°$, $c_l = 0.55$ and $c_{m,c/4} = -0.005$. The zero-lift angle of attack is $-1.1°$. Also, at $\alpha = -4°$, $c_{m,c/4} = -0.0125$. (Note that the "experimental" value of $c_{m,c/4} = -0.01$ tabulated at the end of Example 4.6 is an average value over a range of angle of attack. Since the calculated value of $c_{m,c/4}$ from thin airfoil theory states that the quarter-chord point is the aerodynamic center, it makes sense in Example 4.6 to compare the calculated $c_{m,c/4}$ with an experimental value averaged over a range of angle of attack. However, in the present example, because $c_{m,c/4}$ in reality varies with angle of attack, we use the actual data at two different angles of attack.) From the given information, calculate the location of the aerodynamic center for the NACA 23012 airfoil.

■ **Solution**

Since $c_l = 0.55$ at $\alpha = 4°$ and $c_l = 0$ at $\alpha = -1.1°$, the lift slope is

$$a_0 = \frac{0.55 - 0}{4 - (-1.1)} = 0.1078 \text{ per degree}$$

The slope of the moment coefficient curve is

$$m_0 = \frac{-0.005 - (-0.0125)}{4 - (-4)} = 9.375 \times 10^{-4} \text{ per degree}$$

From Equation (4.71),

$$\bar{x}_{ac} = -\frac{m_0}{a_0} + 0.25 = -\frac{9.375 \times 10^{-4}}{0.1078} + 0.25 = \boxed{0.241}$$

The result agrees exactly with the measured value quoted on page 183 of Abbott and Von Doenhoff (Reference 11).

DESIGN BOX

The result of Example 4.7 shows that the aerodynamic center for the NACA 23012 airfoil is located *ahead* of, but very close to, the quarter-chord point. For some other families of airfoils, the aerodynamic center is located *behind,* but similarly close to, the quarter-chord point. For a given airfoil family, the location of the aerodynamic center depends on the airfoil thickness, as shown in Figure 4.31. The variation of $\bar{x}_{ac}$ with thickness for the NACA 230XX family is given in Figure 4.31*a*. Here, the aerodynamic center is ahead of the quarter-chord point, and becomes progressively farther ahead as the airfoil thickness is increased. In contrast, the variation of $\bar{x}_{ac}$ with thickness for the NACA 64-2XX family is given in Figure 4.31*b*. Here,

the aerodynamic center is behind the quarter-chord point, and becomes progressively farther behind as the airfoil thickness is increased.

From the point of view of purely aerodynamics, the existence of the aerodynamic center is interesting, but the specification of the force and moment system on the airfoil by placing the lift and drag at the aerodynamic center and giving the value of M'_{ac} as illustrated in Figure 4.29, is not more useful than placing the lift and drag at any other point on the airfoil and giving the value of M' at that point, such as shown in Figure 1.25. However, in flight dynamics, and in particular the consideration of the stability and control of flight vehicles, placing the lift and drag at, and
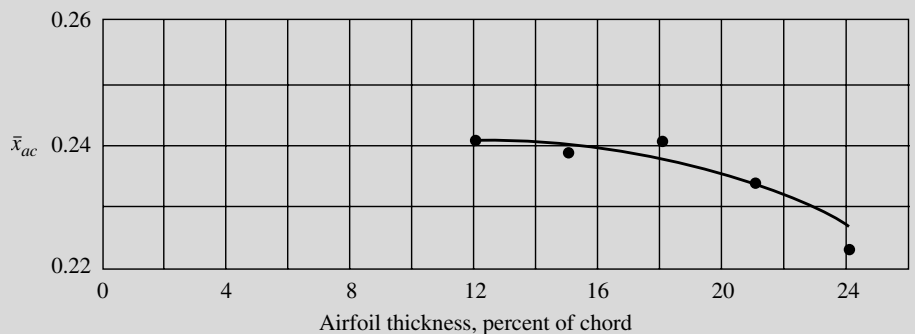
(*a*) **NACA 230XX Airfoil**
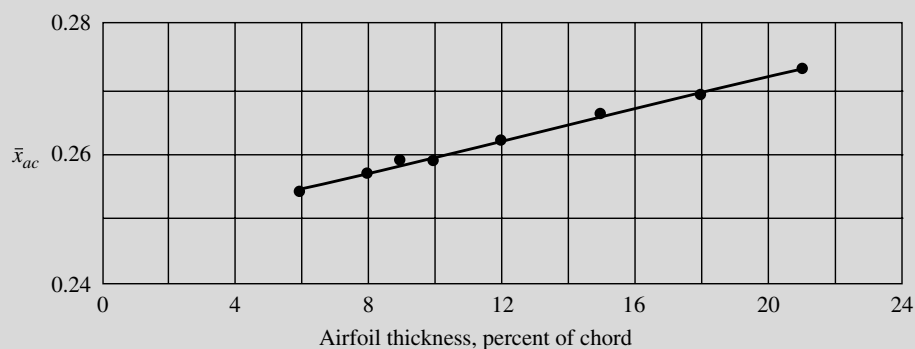
(*b*) **NACA 64-2XX Airfoil**

Figure 4.31 Variation of the location of the aerodynamic center with airfoil thickness. (*a*) NACA 230XX airfoil. (*b*) NACA 64-2XX airfoil.

dealing with the moment about, the aerodynamic center, is particularly convenient. The fact that M_{ac} for a flight vehicle is independent of angle of attack simplifies the analysis of the stability and control characteristics, and the use of the aerodynamic center therefore becomes important in airplane design. In the design process, it is important to know where the aerodynamic centers of the various components of the aircraft (wing, tail, fuselage, etc.) are located, and above all the location of the aerodynamic center for the complete flight vehicle. It is for this reason that we have placed extra emphasis on the aerodynamic center in Section 4.9. For an introduction to stability and control see Chapter 7 of the author's book *Introduction to Flight,* 5th edition, McGraw-Hill, Boston, 2005. For more information about the aerodynamic center, and its use in airplane design, see the author's book *Aircraft Performance and Design*, McGraw-Hill, Boston, 1999.

4.10 LIFTING FLOWS OVER ARBITRARY BODIES: THE VORTEX PANEL NUMERICAL METHOD

The thin airfoil theory described in Sections 4.7 and 4.8 is just what it says—it applies only to thin airfoils at small angles of attack. (Make certain that you understand exactly where in the development of thin airfoil theory these assumptions are made and the reasons for making them.) The advantage of thin airfoil theory is that closed-form expressions are obtained for the aerodynamic coefficients. Moreover, the results compare favorably with experimental data for airfoils of about 12 percent thickness or less. However, the airfoils on many low-speed airplanes are thicker than 12 percent. Moreover, we are frequently interested in high angles of attack, such as occur during takeoff and landing. Finally, we are sometimes concerned with the generation of aerodynamic lift on other body shapes, such as automobiles or submarines. Hence, thin airfoil theory is quite restrictive when we consider the whole spectrum of aerodynamic applications. We need a method that allows us to calculate the aerodynamic characteristics of bodies of arbitrary shape, thickness, and orientation. Such a method is described in this section. Specifically, we treat the vortex panel method, which is a numerical technique that has come into widespread use since the early 1970s. In reference to our road map in Figure 4.7, we now move to the left-hand branch. Also, since this chapter deals with airfoils, we limit our attention to two-dimensional bodies.

The vortex panel method is directly analogous to the source panel method described in Section 3.17. However, because a source has zero circulation, source panels are useful only for nonlifting cases. In contrast, vortices have circulation, and hence vortex panels can be used for lifting cases. (Because of the similarities between source and vortex panel methods, return to Section 3.17 and review the basic philosophy of the source panel method before proceeding further.)

The philosophy of covering a body *surface* with a vortex sheet of such a strength to make the surface a streamline of the flow was discussed in Section 4.4 We then went on to simplify this idea by placing the vortex sheet on the camber line of the airfoil as shown in Figure 4.16, thus establishing the basis for thin airfoil theory. We now return to the original idea of wrapping the vortex sheet over the complete surface of the body, as shown in Figure 4.15. We wish to find

$\gamma(s)$ such that the body surface becomes a streamline of the flow. There exists no closed-form analytical solution for $\gamma(s)$; rather, the solution must be obtained numerically. This is the purpose of the vortex panel method.

Let us approximate the vortex sheet shown in Figure 4.15 by a series of straight panels, as shown earlier in Figure 3.40. (In Chapter 3, Figure 3.40 was used to discuss source panels; here, we use the same sketch for discussion of vortex panels.) Let the vortex strength $\gamma(s)$ per unit length be constant over a given panel, but allow it to vary from one panel to the next. That is, for the n panels shown in Figure 3.40, the vortex panel strengths per unit length are $\gamma_1, \gamma_2, \ldots, \gamma_j, \ldots, \gamma_n$. These panel strengths are unknowns; the main thrust of the panel technique is to solve for γ_j, $j = 1$ to n, such that the body surface becomes a streamline of the flow and such that the Kutta condition is satisfied. As explained in Section 3.17, the midpoint of each panel is a control point at which the boundary condition is applied; that is, at each control point, the normal component of the flow velocity is zero.

Let P be a point located at (x, y) in the flow, and let r_{pj} be the distance from any point on the jth panel to P, as shown in Figure 3.40. The radius r_{pj} makes the angle θ_{pj} with respect to the x axis. The velocity potential induced at P due to the jth panel, $\Delta\phi_j$, is, from Equation (4.3),

$$\Delta\phi_j = -\frac{1}{2\pi} \int_j \theta_{pj} \gamma_j \, ds_j \tag{4.72}$$

In Equation (4.72), γ_j is constant over the jth panel, and the integral is taken over the jth panel only. The angle θ_{pj} is given by

$$\theta_{pj} = \tan^{-1} \frac{y - y_j}{x - x_j} \tag{4.73}$$

In turn, the potential at P due to *all* the panels is Equation (4.72) summed over all the panels:

$$\phi(P) = \sum_{j=1}^{n} \phi_j = -\sum_{j=1}^{n} \frac{\gamma_j}{2\pi} \int_j \theta_{pj} \, ds_j \tag{4.74}$$

Since point P is just an arbitrary point in the flow, let us put P at the control point of the ith panel shown in Figure 3.40. The coordinates of this control point are (x_i, y_i). Then Equations (4.73) and (4.74) become

$$\theta_{ij} = \tan^{-1} \frac{y_i - y_j}{x_i - x_j}$$

and
$$\phi(x_i, y_i) = -\sum_{j=1}^{n} \frac{\gamma_j}{2\pi} \int_j \theta_{ij} \, ds_j \tag{4.75}$$

Equation (4.75) is physically the contribution of *all* the panels to the potential at the control point of the ith panel.

At the control points, the normal component of the velocity is zero; this velocity is the superposition of the uniform flow velocity and the velocity induced by all the vortex panels. The component of V_∞ normal to the ith panel is given by Equation (3.148):

$$V_{\infty,n} = V_\infty \cos \beta_i \tag{3.148}$$

The normal component of velocity induced at (x_i, y_i) by the vortex panels is

$$V_n = \frac{\partial}{\partial n_i}[\phi(x_i, y_i)] \tag{4.76}$$

Combining Equations (4.75) and (4.76), we have

$$V_n = -\sum_{j=1}^{n} \frac{\gamma_j}{2\pi} \int_j \frac{\partial \theta_{ij}}{\partial n_i} \, ds_j \tag{4.77}$$

where the summation is over all the panels. The normal component of the flow velocity at the ith control point is the sum of that due to the freestream [Equation (3.148)] and that due to the vortex panels [Equation (4.77)]. The boundary condition states that this sum must be zero:

$$V_{\infty,n} + V_n = 0 \tag{4.78}$$

Substituting Equations (3.148) and (4.77) into (4.78), we obtain

$$V_\infty \cos \beta_i - \sum_{j=1}^{n} \frac{\gamma_j}{2\pi} \int_j \frac{\partial \theta_{ij}}{\partial n_i} \, ds_j = 0 \tag{4.79}$$

Equation (4.79) is the crux of the vortex panel method. The values of the integrals in Equation (4.79) depend simply on the panel geometry; they are not properties of the flow. Let $J_{i,j}$ be the value of this integral when the control point is on the ith panel. Then Equation (4.79) can be written as

$$V_\infty \cos \beta_i - \sum_{j=1}^{n} \frac{\gamma_j}{2\pi} J_{i,j} = 0 \tag{4.80}$$

Equation (4.80) is a linear algebraic equation with n unknowns, $\gamma_1, \gamma_2, \ldots, \gamma_n$. It represents the flow boundary condition evaluated at the control point of the ith panel. If Equation (4.80) is applied to the control points of *all* the panels, we obtain a system of n linear equations with n unknowns.

To this point, we have been deliberately paralleling the discussion of the source panel method given in Section 3.17; however, the similarity stops here. For the source panel method, the n equations for the n unknown source strengths are routinely solved, giving the flow over a nonlifting body. In contrast, for the lifting case with vortex panels, in addition to the n equations given by Equation (4.80) applied at all the panels, we must also satisfy the Kutta condition. This can be done in several ways. For example, consider Figure 4.32, which illustrates a detail of the vortex panel distribution at the trailing edge. Note that the length of each
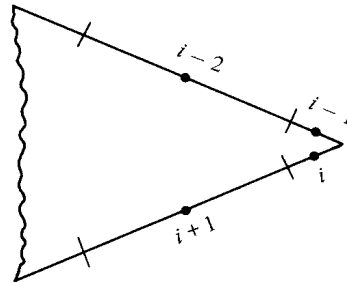
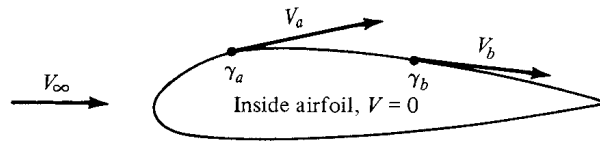**Figure 4.32** Vortex panels at the trailing edge.

Figure 4.33 Airfoil as a solid body, with zero velocity inside the profile.

panel can be different; their length and distribution over the body are up to your discretion. Let the two panels at the trailing edge (panels i and $i - 1$ in Figure 4.32) be very small. The Kutta condition is applied *precisely* at the trailing edge and is given by $\gamma(\text{TE}) = 0$. To approximate this numerically, if points i and $i - 1$ are close enough to the trailing edge, we can write

$$\gamma_i = -\gamma_{i-1} \tag{4.81}$$

such that the strengths of the two vortex panels i and $i - 1$ exactly cancel at the point where they touch at the trailing edge. Thus, in order to impose the Kutta condition on the solution of the flow, Equation (4.81) (or an equivalent expression) must be included. Note that Equation (4.80) evaluated at all the panels and Equation (4.81) constitute an *overdetermined* system of n unknowns with $n + 1$ equations. Therefore, to obtain a determined system, Equation (4.80) is not evaluated at one of the control points on the body. That is, we choose to ignore one of the control points, and we evaluate Equation (4.80) at the other $n - 1$ control points. This, in combination with Equation (4.81), now gives a system of n linear algebraic equations with n unknowns, which can be solved by standard techniques.

At this stage, we have conceptually obtained the values of $\gamma_1, \gamma_2, \ldots, \gamma_n$ which make the body surface a streamline of the flow and which also satisfy the Kutta condition. In turn, the flow velocity tangent to the surface can be obtained directly from γ. To see this more clearly, consider the airfoil shown in Figure 4.33. We are concerned only with the flow outside the airfoil and on its surface. Therefore, let the velocity be zero at every point *inside* the body, as shown in Figure 4.33. In particular, the velocity just inside the vortex sheet on the surface

is zero. This corresponds to $u_2 = 0$ in Equation (4.8). Hence, the velocity just outside the vortex sheet is, from Equation (4.8),

$$\gamma = u_1 - u_2 = u_1 - 0 = u_1$$

In Equation (4.8), u denotes the velocity tangential to the vortex sheet. In terms of the picture shown in Figure 4.33, we obtain $V_a = \gamma_a$ at point a, $V_b = \gamma_b$ at point b, etc. Therefore, *the local velocities tangential to the airfoil surface are equal to the local values of γ*. In turn, the local pressure distribution can be obtained from Bernoulli's equation.

The total circulation and the resulting lift are obtained as follows. Let s_j be the length of the jth panel. Then the circulation due to the jth panel is $\gamma_j s_j$. In turn, the total circulation due to all the panels is

$$\Gamma = \sum_{j=1}^{n} \gamma_j s_j \tag{4.82}$$

Hence, the lift per unit span is obtained from

$$L' = \rho_\infty V_\infty \sum_{j=1}^{n} \gamma_j s_j \tag{4.83}$$

The presentation in this section is intended to give only the general flavor of the vortex panel method. There are many variations of the method in use today, and you are encouraged to read the modern literature, especially as it appears in the *AIAA Journal* and the *Journal of Aircraft* since 1970. The vortex panel method as described in this section is termed a "first-order" method because it assumes a constant value of γ over a given panel. Although the method may appear to be straightforward, its numerical implementation can sometimes be frustrating. For example, the results for a given body are sensitive to the number of panels used, their various sizes, and the way they are distributed over the body surface (i.e., it is usually advantageous to place a large number of small panels near the leading and trailing edges of an airfoil and a smaller number of larger panels in the middle). The need to ignore one of the control points in order to have a determined system in n equations for n unknowns also introduces some arbitrariness in the numerical solution. Which control point do you ignore? Different choices sometimes yield different numerical answers for the distribution of γ over the surface. Moreover, the resulting numerical distributions for γ are not always smooth, but rather, they have oscillations from one panel to the next as a result of numerical inaccuracies. The problems mentioned above are usually overcome in different ways by different groups who have developed relatively sophisticated panel programs for practical use. For example, what is more common today is to use a *combination* of both source and vortex panels (source panels to basically simulate the airfoil thickness and vortex panels to introduce circulation) in a panel solution. This combination helps to mitigate some of the practical numerical problems just discussed. Again, you are encouraged to consult the literature for more information.
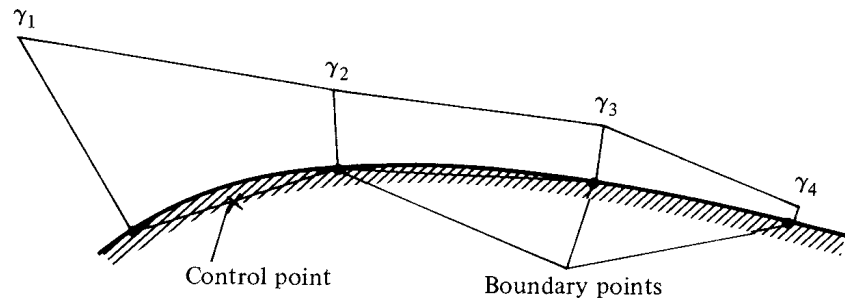
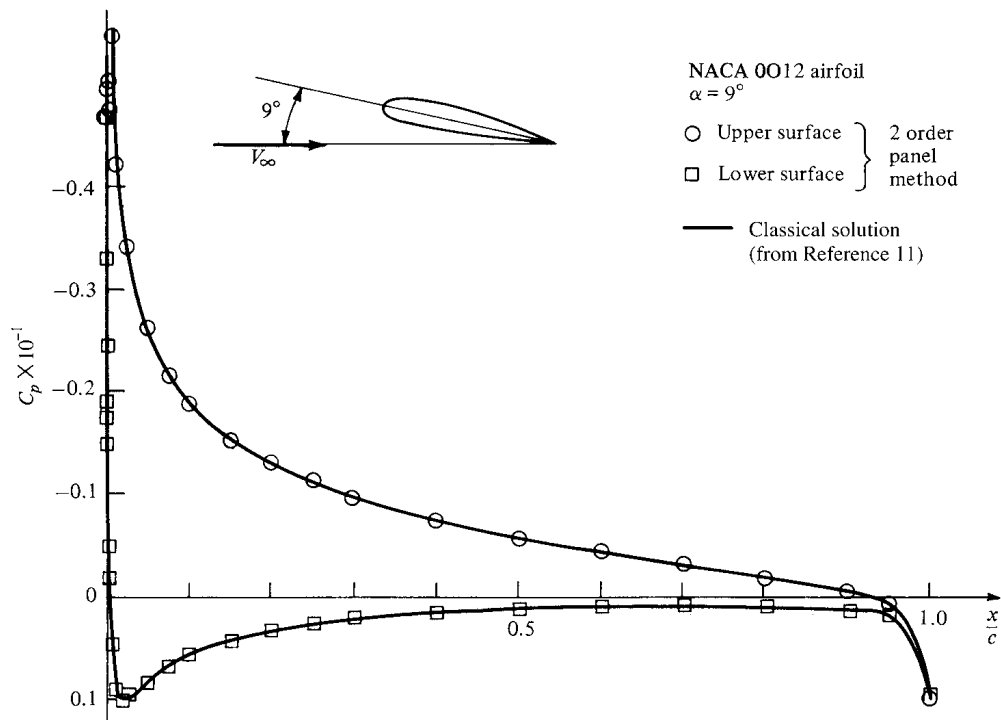**Figure 4.34** Linear distribution of γ over each panel—a second-order panel method.

Figure 4.35 Pressure coefficient distribution over an NACA 0012 airfoil; comparison between second-order vortex panel method and NACA theoretical results from Reference 11. The numerical panel results were obtained by one of the author's graduate students, Dr. Tae-Hwan Cho.

Such accuracy problems have also encouraged the development of higher-order panel techniques. For example, a "second-order" panel method assumes a *linear* variation of γ over a given panel, as sketched in Figure 4.34. Here, the value of γ at the edges of each panel is matched to its neighbors, and the values γ_1, γ_2, γ_3, etc. at the *boundary points* become the unknowns to be solved. The flow-tangency boundary condition is still applied at the *control point* of each

panel, as before. Some results using a second-order vortex panel technique are given in Figure 4.35, which shows the distribution of pressure coefficients over the upper and lower surfaces of an NACA 0012 airfoil at a 9° angle of attack. The circles and squares are numerical results from a second-order vortex panel technique developed at the University of Maryland, and the solid lines are from NACA results given in Reference 11. Excellent agreement is obtained.

Again, you are encouraged to consult the literature before embarking on any serious panel solutions of your own. For example, Reference 14 is a classic paper on panel methods, and Reference 15 highlights many of the basic concepts of panel methods along with actual computer program statement listings for simple applications. Reference 66 is a modern compilation of papers, several of which deal with current panel techniques. Finally, Katz and Plotkin (Reference 67) give perhaps the most thorough discussion of panel techniques and their foundations to date.

4.11 MODERN LOW-SPEED AIRFOILS

The nomenclature and aerodynamic characteristics of standard NACA airfoils are discussed in Sections 4.2 and 4.3; before progressing further, you should review these sections in order to reinforce your knowledge of airfoil behavior, especially in light of our discussions on airfoil theory. Indeed, the purpose of this section is to provide a modern sequel to the airfoils discussed in Sections 4.2 and 4.3.

During the 1970s, NASA designed a series of low-speed airfoils that have performance superior to the earlier NACA airfoils. The standard NACA airfoils were based almost exclusively on experimental data obtained during the 1930s and 1940s. In contrast, the new NASA airfoils were designed on a computer using a numerical technique similar to the source and vortex panel methods discussed earlier, along with numerical predictions of the viscous flow behavior (skin friction and flow separation). Wind-tunnel tests were then conducted to verify the computer-designed profiles and to obtain the definitive airfoil properties. Out of this work first came the general aviation–Whitcomb [GA(W)-1] airfoil, which has since been redesignated the LS(1)-0417 airfoil. The shape of this airfoil is given in Figure 4.36, obtained from Reference 16. Note that it has a large leading-edge radius ($0.08c$ in comparison to the standard $0.02c$) in order to flatten the usual peak in pressure coefficient near the nose. Also, note that the bottom surface near the trailing edge is cusped in order to increase the camber and hence the aerodynamic

Figure 4.36 Profile for the NASA LS(1)-0417 airfoil. When first introduced, this airfoil was labeled the GA(W)-1 airfoil, a nomenclature which has now been superseded. *(From Reference 16.)*
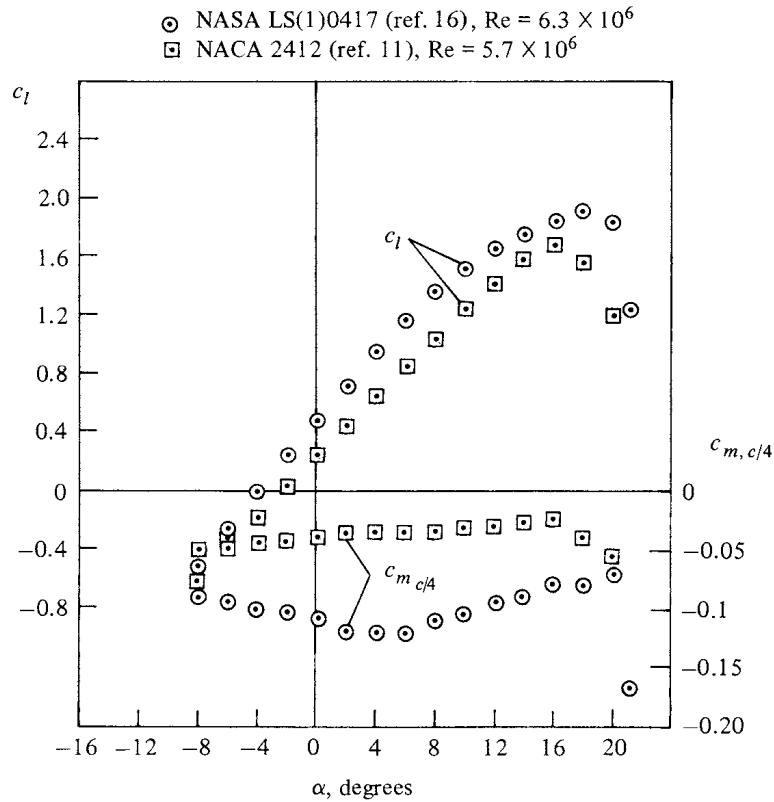
Figure 4.37 Comparison of the modern NASA LS(1)-0417 airfoil with the standard NACA 2412 airfoil.

loading in that region. Both design features tend to discourage flow separation over the top surface at high angle of attack, hence yielding higher values of the maximum lift coefficient. The experimentally measured lift and moment properties (from Reference 16) are given in Figure 4.37, where they are compared with the properties for an NACA 2412 airfoil, obtained from Reference 11. Note that $c_{l,\text{max}}$ for the NASA LS(1)-0417 is considerably higher than for the NACA 2412.

The NASA LS(1)-0417 airfoil has a maximum thickness of 17 percent and a design lift coefficient of 0.4. Using the same camber line, NASA has extended this airfoil into a family of low-speed airfoils of different thicknesses, for example, the NASA LS(1)-0409 and the LS(1)-0413. (See Reference 17 for more details.) In comparison with the standard NACA airfoils having the same thicknesses, these new LS(1)-04xx airfoils all have:

1. Approximately 30 percent higher $c_{l,\text{max}}$.
2. Approximately a 50 percent increase in the ratio of lift to drag (L/D) at a lift coefficient of 1.0. This value of $c_l = 1.0$ is typical of the climb lift coefficient for general aviation aircraft, and a high value of L/D greatly improves the climb performance. (See Reference 2 for a general

introduction to airplane performance and the importance of a high L/D ratio to airplane efficiency.)

It is interesting to note that the shape of the airfoil in Figure 4.36 is very similar to the supercritical airfoils to be discussed in Chapter 11. The development of the supercritical airfoil by NASA aerodynamicist Richard Whitcomb in 1965 resulted in a major improvement in airfoil drag behavior at high subsonic speeds, near Mach 1. The supercritical airfoil was a major breakthrough in high-speed aerodynamics. The LS(1)-0417 low-speed airfoil shown in Figure 4.36, first introduced as the GA(W)-1 airfoil, was a later spin-off from supercritical airfoil research. It is also interesting to note that the first production aircraft to use the NASA LS(1)-0417 airfoil was the Piper PA-38 Tomahawk, introduced in the late 1970s.

In summary, new airfoil development is alive and well in the aeronautics of the late twentieth century. Moreover, in contrast to the purely experimental development of the earlier airfoils, we now enjoy the benefit of powerful computer programs using panel methods and advanced viscous flow solutions for the design of new airfoils. Indeed, in the 1980s NASA established an official Airfoil Design Center at The Ohio State University, which services the entire general aviation industry with over 30 different computer programs for airfoil design and analysis. For additional information on such new low-speed airfoil development, you are urged to read Reference 16, which is the classic first publication dealing with these airfoils, as well as the concise review given in Reference 17.

DESIGN BOX

This chapter deals with incompressible flow over airfoils. Moreover, the analytical thin airfoil theory and the numerical panel methods discussed here are techniques for calculating the aerodynamic characteristics for a *given airfoil of specified shape*. Such an approach is frequently called the *direct problem,* wherein the shape of the body is given, and the surface pressure distribution (for example) is calculated. For design purposes, it is desirable to turn this process inside-out; it is desirable to specify the surface pressure distribution—a pressure distribution that will achieve enhanced airfoil performance—and calculate the shape of the airfoil that will produce the specified pressure distribution. This approach is called the *inverse problem*. Before the advent of the high-speed digital computer, and the concurrent rise of the discipline of computational fluid dynamics in the 1970s (see Section 2.17.2), the analytical solution of the inverse problem was difficult, and was not used by the practical airplane designer. Instead, for most of the airplanes designed before and during the twentieth century, the choice of an airfoil shape was based on reasonable experimental data (at best), and guesswork (at worst). This story is told in some detail in Reference 62. The design problem was made more comfortable with the introduction of the various families of NACA airfoils, beginning in the early 1930s. A logical method was used for the geometrical design of these airfoils, and definitive experimental data on the NACA airfoils were made available (such as shown in Figures 4.10, 4.11, and 4.28). For this reason, many airplanes designed during the middle of the twentieth century used standard NACA airfoil sections. Even today, the NACA airfoils are sometimes the most expeditious choice of the airplane designer, as indicated by the tabulation (by no means complete) in Section 4.2 of airplanes using such airfoils.
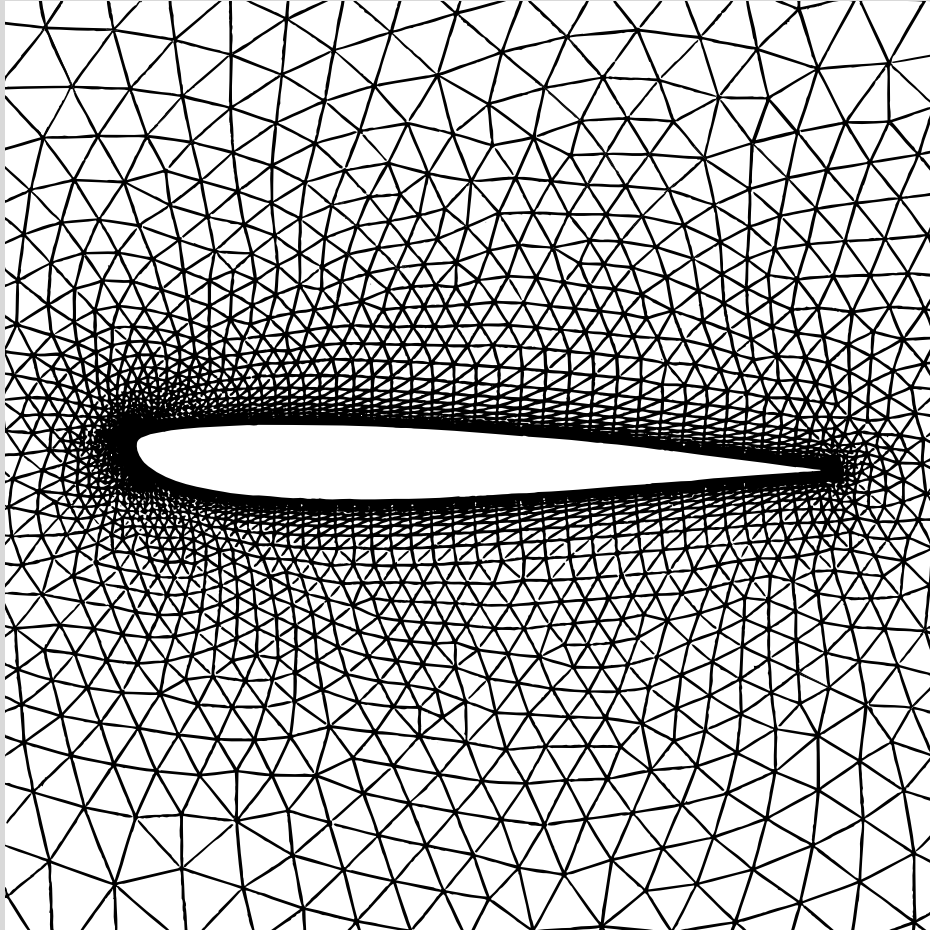
Figure 4.38 Unstructured mesh for the numerical calculation of the flow over an airfoil. *(Data Source: Anderson and Bonhaus, Reference 68.)*

However, today the power of computational fluid dynamics (CFD) is revolutionizing airfoil design and analysis. The inverse problem, and indeed the next step—the overall automated procedure that results in a completely optimized airfoil shape for a given design point—are being made tractable by CFD. An example of such work is illustrated in Figures 4.38 and 4.39, taken from the recent work of Kyle Anderson and Daryl Bonhaus (Reference 68). Here, CFD solutions of the continuity, momentum, and energy equations for a compressible, viscous flow (the Navier-Stokes equations, as denoted in Section 2.17.2) are carried out for the purpose of airfoil design. Using a finite volume CFD technique, and the grid shown in Figure 4.38, the inverse problem is solved. The *specified* pressure distribution over the top and bottom surfaces of the airfoil is given by the circles in Figure 4.39*a*. The optimization technique is iterative and requires starting with a pressure distribution that is not the desired, specified one; the initial distribution is given by the solid curves in Figure 4.39*a*, and the airfoil shape corresponding to this initial pressure distribution is shown by the solid curve in Figure 4.39*b*. (In Figure 4.39*b*, the airfoil shape appears distorted because an expanded scale is used for the ordinate.) After 10 design cycles, the optimized airfoil shape that supports
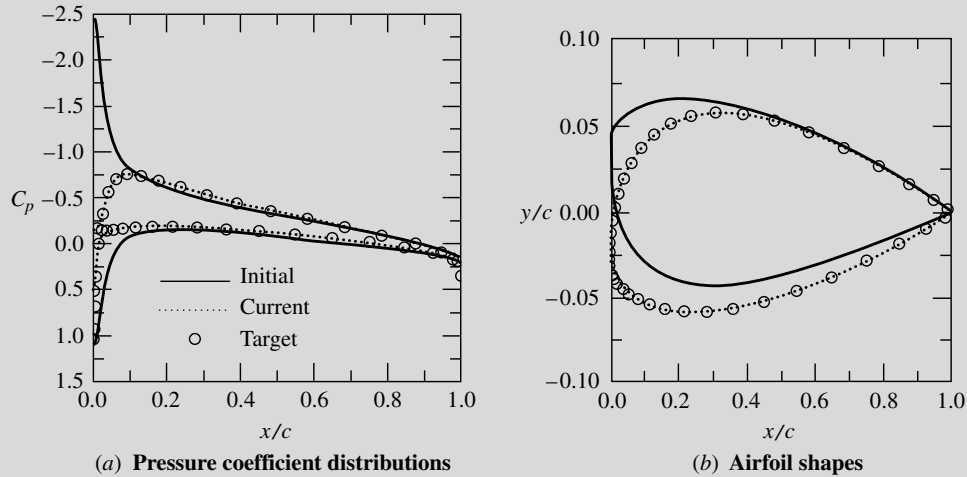
Figure 4.39 An example of airfoil optimized design using computational fluid dynamics. *(Data Source: Anderson and Bonhaus, Reference 68.)*

the specified pressure distribution is obtained, as given by the circles in Figure 4.39*b*. The initial airfoil shape is also shown in constant scale in Figure 4.38.

The results given in Figures 4.38 and 4.39 are shown here simply to provide the flavor of modern airfoil design and analysis. This is reflective of the wave of future airfoil design procedures, and you are encouraged to read the contemporary literature in order to keep up with this rapidly evolving field. However, keep in mind that the simpler analytical approach of thin airfoil theory discussed in the present chapter, and especially the simple practical results of this theory, will continue to be part of the whole "toolbox" of procedures to be used by the designer in the future. The fundamentals embodied in thin airfoil theory will continue to be part of the fundamentals of aerodynamics and will always be there as a partner with the modern CFD techniques.

4.12 VISCOUS FLOW: AIRFOIL DRAG

This is another "stand-alone" viscous flow section in the same spirit as Section 1.11. It does not break the continuity of our discussions on inviscid flow; rather, it is designed to complement them. Before reading further, you are encouraged to review the introduction to boundary layers given in Section 1.11.

The lift on an airfoil is primarily due to the pressure distribution exerted on its surface; the shear stress distribution acting on the airfoil, when integrated in the lift direction, is usually negligible. The lift, therefore, can be accurately calculated assuming inviscid flow in conjunction with the Kutta condition at the trailing edge. When used to predict drag, however, this same approach yields zero drag, a result that goes against common sense, and is called *d'Alembert's paradox* after Jean le Rond d'Alembert, the eighteenth-century French mathematician and scientist who first made such drag calculations for inviscid flows over two-dimensional bodies (see Sections 3.13 and 3.20).
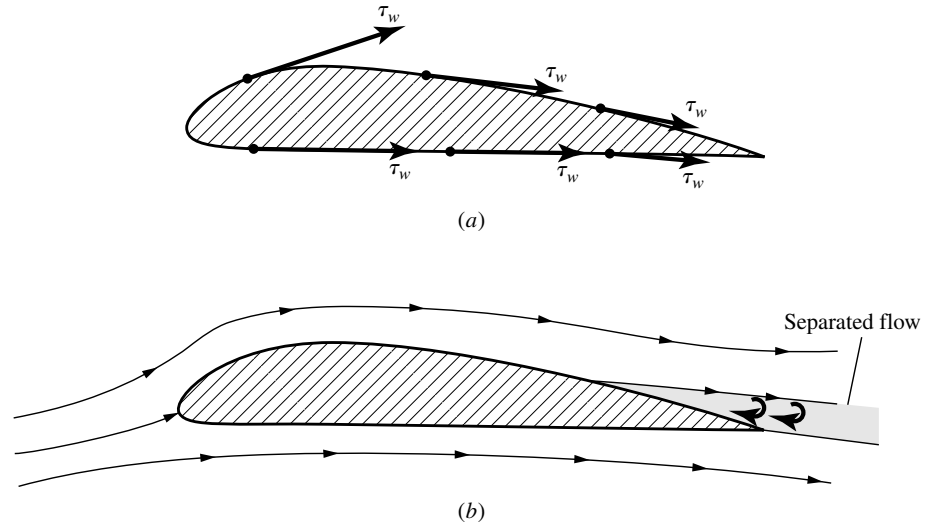
Figure 4.40 Subsonic airfoil drag is due to two components: (*a*) shear stress acting on the surface, and (*b*) pressure drag due to flow separation.
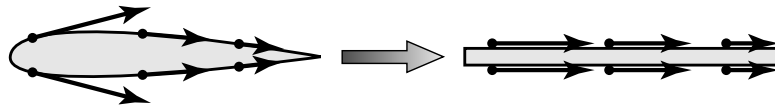

Figure 4.41 Estimation of skin-friction drag on an airfoil from that on a flat plate.

The paradox is immediately removed when viscosity (friction) is included in the flow. Indeed, viscosity in the flow is totally responsible for the aerodynamic drag on an airfoil. It acts through two mechanisms:

1. *Skin-friction drag,* due to the shear stress acting on the surface (Figure 4.40*a*), and

2. *Pressure drag due to flow separation,* sometimes called *form drag* (Figure 4.40*b*).

That shear stress creates drag is self-evident from Figure 4.40*a*. The pressure drag created by flow separation (Figure 4.40*b*) is a more subtle phenomenon and will be discussed towards the end of this section.

4.12.1 Estimating Skin-Friction Drag: Laminar Flow

As a first approximation, we assume that skin-friction drag on an airfoil is essentially the same as the skin-friction drag on a flat plate at zero angle of attack, as illustrated in Figure 4.41. Obviously, this approximation becomes more accurate the thinner the airfoil and the smaller the angle of attack. Consistent with the rest of this chapter, we will continue to deal with low-speed incompressible flow.
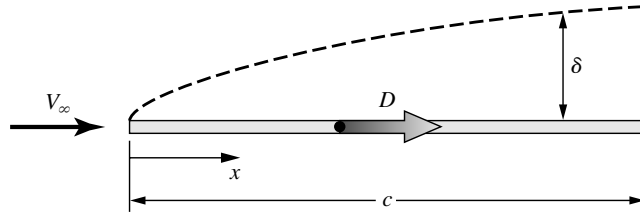
Figure 4.42 Total friction drag on a flat plate.

We first deal with the case of completely laminar flow over the airfoil (and hence the flat plate) in Figure 4.41. There is an exact analytical solution for the laminar boundary-layer flow over a flat plate. The details of this solution are given in Section 18.2, where we present boundary-layer theory in some detail. For the present section, we will use just the results of Section 18.2.

The boundary-layer thickness for incompressible laminar flow over a flat plate at zero angle of attack is given by Equation (18.23), repeated and renumbered below:

$$\delta = \frac{5.0x}{\sqrt{\text{Re}_x}} \tag{4.84}$$

where Re_x is the Reynolds number based on distance x measured from the leading edge (Figure 4.42),

$$\text{Re}_x = \frac{\rho_e V_\infty x}{\mu_\infty}$$

Note from Equation (4.84) that $\delta \propto \sqrt{x}$, that is, the boundary-layer thickness grows parabolically with distance from the leading edge.

The local shear stress, integrated over both the top and bottom surfaces of the flat plate shown in Figure 4.41, yields the net friction drag, D_f, on the plate, illustrated in Figure 4.42. To begin with, however, let us consider just *one* surface of the plate, either the top surface or the bottom surface. The shear stress distribution over the top surface is the same as that over the bottom surface. Let us choose the top surface. The integral of the shear stress over the top surface gives the net friction drag on that surface, $D_{f,\text{top}}$. Clearly, the net friction drag due to the shear stress integrated over the bottom surface, $D_{f,\text{bottom}}$, is the same value, $D_{f,\text{bottom}} = D_{f,\text{top}}$. Hence, the total skin friction drag, D_f, is

$$D_f = 2D_{f,\text{top}} = 2D_{f,\text{bottom}}$$

Define the skin-friction drag coefficient for the flow over *one* surface as

$$C_f \equiv \frac{D_{f,\text{top}}}{q_\infty S} = \frac{D_{f,\text{bottom}}}{q_\infty S} \tag{4.85}$$

The skin-friction drag coefficient is a function of the Reynolds number, and is given by Equation (18.22), repeated and renumbered below,

$$C_f = \frac{1.328}{\sqrt{\text{Re}_c}} \tag{4.86}$$

where Re_c is the Reynolds number based on the chord length c shown in Figure 4.42

$$\text{Re}_c = \frac{\rho_\infty V_\infty c}{\mu_\infty}$$

EXAMPLE 4.8

Consider the NACA 2412 airfoil, data for which is given in Figures 4.10 and 4.11. The data are given for two values of the Reynolds number based on chord length. For the case where $\text{Re}_c = 3.1 \times 10^6$, estimate: (a) the laminar boundary layer thickness at the trailing edge for a chord length of 1.5 m and (b) the net laminar skin-friction drag coefficient for the airfoil.

■ **Solution**

(a) From Equation (4.84) applied at the trailing edge, where $x = c$, we have

$$\delta = \frac{5.0c}{\sqrt{\text{Re}_c}} = \frac{(5.0)(1.5)}{\sqrt{3.1 \times 10^6}} = \boxed{0.00426 \text{ m}}$$

Notice how thin the boundary layer is; at the trailing edge, where its thickness is the largest, the boundary layer is only 0.426 cm thick.

(b) From Equation (4.86),

$$C_f = \frac{1.328}{\sqrt{\text{Re}_c}} = \frac{1.328}{\sqrt{3.1 \times 10^6}} = 7.54 \times 10^{-4}$$

Recall that the above result is for a single surface, either the top or bottom of the plate. Taking both surfaces into account:

$$\text{Net } C_f = 2(7.54 \times 10^{-4}) = \boxed{0.0015}$$

From the data in Figure 4.11, we see that at zero angle of attack for $\text{Re} = 3.1 \times 10^6$, the airfoil drag coefficient is 0.0068. This measured value is about 4.5 times higher than the value of 0.0015 we just calculated. But wait a moment! For the relatively high Reynolds number of 3.1×10^6, the boundary layer over the airfoil will be *turbulent,* not laminar. So our laminar flow calculation is not an appropriate estimate for the boundary layer thickness and the airfoil drag coefficient. Let us take the next step.

4.12.2 Estimating Skin-Friction Drag: Turbulent Flow

In contrast to the situation for laminar flow, there are no exact analytical solutions for turbulent flow. This sad state of affairs is discussed in Chapter 19. The analysis of any turbulent flow requires some amount of empirical data. All analyses of turbulent flow are approximate.

The analysis of the turbulent boundary layer over a flat plate is no exception. From Chapter 19 we lift the following approximate results for the incompressible turbulent flow over a flat plate. From Equation (19.1) repeated and

renumbered below:

$$\delta = \frac{0.37x}{\mathrm{Re}_x^{1/5}} \qquad (4.87)$$

and from Equation (19.2) repeated and renumbered below:

$$C_f = \frac{0.074}{\mathrm{Re}_c^{1/5}} \qquad (4.88)$$

We emphasize again that Equations (4.87) and (4.88) are only approximate results, and they represent only one set of results among a myriad of different turbulent flow analyses for the flat plate boundary layer. Nevertheless, Equations (4.87) and (4.88) give us some reasonable means to estimate the boundary-layer thickness and skin-friction drag coefficient for turbulent flow. Note that, in contrast to the inverse square root variation with Reynolds number for laminar flow, the turbulent flow results show an inverse fifth root variation with Reynolds number.

EXAMPLE 4.9

Repeat Example 4.8 assuming a turbulent boundary layer over the airfoil.

■ **Solution**

Once again we replace the airfoil with a flat plate at zero angle of attack.

   (*a*) The boundary-layer thickness at the trailing edge, where $x = c$ and $\mathrm{Re}_x = \mathrm{Re}_c = 3.1 \times 10^6$, is given by Equation (4.87):

$$\delta = \frac{0.37x}{\mathrm{Re}_x^{1/5}} = \frac{0.37(1.5)}{(3.1 \times 10^6)^{1/5}} = \boxed{0.0279 \text{ m}}$$

The turbulent boundary layer is still thin, 2.79 cm at the trailing edge, but by comparison is much thicker than the laminar boundary layer thickness of 0.426 cm from Example 4.8.

   (*b*) The skin-friction drag coefficient (based on one side of the flat plate) is given by Equation (4.88):

$$C_f = \frac{0.074}{\mathrm{Re}_c^{1/5}} = \frac{0.074}{(3.1 \times 10^6)^{1/5}} = 0.00372$$

The net skin-friction drag coefficient, taking into account both the top and bottom surfaces of the flat plate, is

$$\text{Net } C_f = 2(0.00372) = \boxed{0.00744}$$

This result is a factor of five larger than for the laminar boundary layer, and serves as an illustration of the considerable increase in skin friction caused by a turbulent boundary layer in comparison to that caused by a laminar boundary layer.

   The result for the skin friction drag coefficient in Example 4.9 is larger than the measured drag coefficient of the airfoil of 0.0068, which is the *sum* of both

skin friction drag and pressure drag due to flow separation. So our result in this example clearly overestimates the skin friction drag coefficient for the airfoil. But wait a minute! In actuality, the boundary layer over a body always starts out as a *laminar* boundary for some distance from the leading edge, and then transists to a turbulent boundary layer at some point downstream of the leading edge. The skin-friction drag is therefore a combination of laminar skin friction over the forward part of the airfoil, and turbulent skin friction over the remaining part. Let us examine this situation.

4.12.3 Transition

In Section 4.12.1 we assumed that the flow over a flat plate was all laminar. Similarly, in Section 4.12.2 we assumed all turbulent flow. In reality, the flow *always* starts out from the leading edge as laminar. Then at some point downstream of the leading edge, the laminar boundary layer becomes unstable and small "bursts" of turbulence begin to grow in the flow. Finally, over a certain region called the *transition region,* the boundary layer becomes completely turbulent. For purposes of analysis, we usually draw the picture shown in Figure 4.43, where a laminar boundary layer starts out from the leading edge of the flat plate and grows parabolically downstream. Then at the *transition point,* it becomes a turbulent boundary layer growing at a faster rate, on the order of $x^{4/5}$ downstream. The value of x where transition is said to take place is the *critical* value x_{cr}. In turn, x_{cr} allows the definition of a *critical Reynolds number* for transition as

$$\text{Re}_{x_{cr}} = \frac{\rho_\infty V_\infty x_{cr}}{\mu_\infty} \tag{4.89}$$

Transition is discussed in more detail in Section 15.2. Volumes of literature have been written on the phenomenon of transition from laminar to turbulent flow. Obviously, because τ_w is different for the two flows—as clearly illustrated by comparing the results of Examples 4.8 and 4.9—knowledge of where on the surface transition occurs is vital to an accurate prediction of skin friction drag. The location of the transition point (in reality, a finite region) depends on many quantities as discussed in Section 15.2. However, if the critical Reynolds number is given to you (usually from experiments for a given type of flow over a given
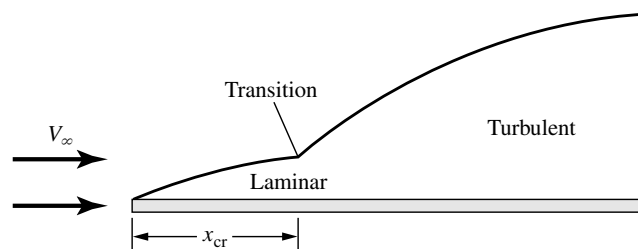

Figure 4.43 Transition from laminar to turbulent flow. The boundary layer thickness is exaggerated for clarity.

body), then the location of transition, x_{cr}, for that type of flow can be obtained directly from the definition, Equation (4.89).

For example, assume that you have an airfoil of given surface roughness (one of the factors that affect the location of transition) in a flow at a free-stream velocity of 50 m/s and you wish to predict how far from the leading edge the transition will take place. After searching through the literature for low-speed flows over such surfaces, you may find that the critical Reynolds number determined from experience is approximately $\text{Re}_{x_{cr}} = 5 \times 10^5$. Applying this "experience" to your problem, using Equation (4.89), and assuming the thermodynamic conditions correspond to standard sea level, where $\rho_\infty = 1.23 \text{ kg/m}^3$ and (from Section 1.11) $\mu_\infty = 1.789 \times 10^{-5} \text{ kg/(m)(s)}$, you find

$$x_{cr} = \frac{\mu_\infty \text{Re}_{x_{cr}}}{\rho_\infty V_\infty} = \frac{(1.789 \times 10^{-5})(5 \times 10^5)}{(1.23)(50)} = 0.145 \text{ m}$$

Note that the region of laminar flow in this example extends from the leading edge to 14.5 cm downstream from the leading edge. If now you double the freestream velocity to 100 m/s, the transition point is still governed by the critical Reynolds number, $\text{Re}_{x_{cr}} = 5 \times 10^5$. Thus,

$$x_{cr} = \frac{(1.789 \times 10^{-5})(5 \times 10^5)}{(1.23)(100)} = 0.0727 \text{ m}$$

Hence, when the velocity is doubled, the transition point moves forward one-half the distance to the leading edge.

In summary, once you know the critical Reynolds number, you can find x_{cr} from Equation (4.89). However, an accurate value for $\text{Re}_{x_{cr}}$ applicable to your problem must come from somewhere—experiment, free flight, or some semi-empirical theory—and this may be difficult to obtain. This situation provides a little insight into why basic studies of transition and turbulence are needed to advance our understanding of such flows and to allow us to apply more valid reasoning to the prediction of transition in practical problems.

EXAMPLE 4.10

For the NACA 2412 airfoil and the conditions in Example 4.7, calculate the net skin friction drag coefficient assuming that the critical Reynolds number is 500,000.

■ **Solution**

Consider Figure 4.44, which shows a flat plate with a laminar boundary layer extending from the leading edge over the distance x_1 to the transition point (region 1), and a turbulent boundary extending over the distance x_2 from the transition point to the trailing edge (region 2). The critical Reynolds number is

$$\text{Re}_{x_{cr}} = \frac{\rho_\infty V_\infty x_{cr}}{\mu_\infty} = 5 \times 10^5$$
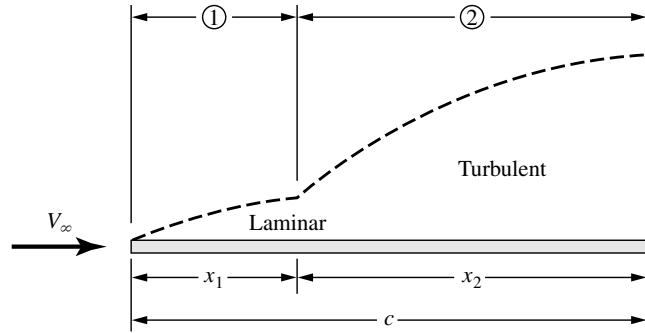
Figure 4.44 Laminar (region 1) and turbulent (region 2) flow over a flat plate.

where in Figure 4.44, $x_{cr} = x_1$. Hence

$$\text{Re}_{x_{cr}} = \frac{\rho_\infty V_\infty x_1}{\mu_\infty} = 5 \times 10^5$$

The Reynolds number based on chord length is given as

$$\text{Re}_c = \frac{\rho_\infty V_\infty c}{\mu_\infty} = 3.1 \times 10^6$$

Thus

$$\frac{\text{Re}_{x_{cr}}}{\text{Re}_c} = \frac{5 \times 10^5}{3.1 \times 10^6} = 0.1613 = \frac{(\rho_\infty V_\infty x_1/\mu_\infty)}{(\rho_\infty V_\infty c/\mu_\infty)} = \frac{x_1}{c}$$

This locates the transition point relative to the chord length, that is, in Figure 4.44, we have

$$\frac{x_1}{c} = 0.1613$$

Because the Reynolds number in the equations for skin friction drag coefficient is always based on length measured *from the leading edge,* we can not simply calculate the turbulent skin friction drag coefficient for region 2 by using Equation (4.88) with a Reynolds number based on x_2. Rather, we must carry out the following procedure.

Assuming all turbulent flow over the entire length of the plate, the drag (on one side of the plate) is $(D_{f,c})_{\text{turbulent}}$, where

$$(D_{f,c})_{\text{turbulent}} = q_\infty S (C_{f,c})_{\text{turbulent}}$$

As usual, we are dealing with the drag per unit span, hence $S = c(1)$.

$$(D_{f,c})_{\text{turbulent}} = q_\infty c (C_{f,c})_{\text{turbulent}}$$

The turbulent drag on just region 1 is $(D_{f,1})_{\text{turbulent}}$:

$$(D_{f,1})_{\text{turbulent}} = q_\infty S (C_{f,1})_{\text{turbulent}}$$

Here, $S = (x_1)(1)$:

$$(D_{f,1})_{\text{turbulent}} = q_\infty x_1 (C_{f,1})_{\text{turbulent}}$$

Thus, the turbulent drag just on region 2, $(D_{f,2})_{\text{turbulent}}$, is

$$(D_{f,2})_{\text{turbulent}} = (D_{f,c})_{\text{turbulent}} - (D_{f,1})_{\text{turbulent}}$$

$$(D_{f,2})_{\text{turbulent}} = q_\infty c(C_{f,c})_{\text{turbulent}} - q_\infty x_1 (C_{f,1})_{\text{turbulent}}$$

The laminar drag on region 1 is $(D_{f,1})_{\text{laminar}}$

$$(D_{f,1})_{\text{laminar}} = q_\infty S(C_{f,1})_{\text{laminar}} = q_\infty x_1 (C_{f,1})_{\text{laminar}}$$

The total skin-friction drag on the plate, D_f, is then

$$D_f = (D_{f,1})_{\text{laminar}} + (D_{f,2})_{\text{turbulent}}$$

or, $\qquad D_f = q_\infty x_1 (C_{f,1})_{\text{laminar}} + q_\infty c(C_{f,c})_{\text{turbulent}} - q_\infty x_1 (C_{f,1})_{\text{turbulent}}$ (4.90)

The total skin-friction drag coefficient is

$$C_f = \frac{D_f}{q_\infty S} = \frac{D_f}{q_\infty c} \tag{4.91}$$

Combining Equations (4.90) and (4.91):

$$C_f = \frac{x_1}{c}(C_{f,1})_{\text{laminar}} + (C_{f,c})_{\text{turbulent}} - \frac{x_1}{c}(C_{f,1})_{\text{turbulent}} \tag{4.92}$$

Since $x_1/c = 0.1613$, Equation (4.92) becomes

$$C_f = 0.1613(C_{f,1})_{\text{laminar}} + (C_{f,c})_{\text{turbulent}} - 0.1613(C_{f,1})_{\text{turbulent}} \tag{4.93}$$

The various skin friction drag coefficients in Equation (4.93) are obtained as follows. The Reynolds number for region 1 is

$$\text{Re}_{x_1} = \frac{\rho_\infty V_\infty x_1}{\mu_\infty} = \frac{x_1}{c}\left(\frac{\rho_\infty V_\infty c}{\mu_\infty}\right) = \frac{x_1}{c}\text{Re}_c = 0.1613(3.1 \times 10^6) = 5 \times 10^5$$

(Of course, we could have written this down directly because $x = x_1$ is the transition point, *determined* from the critical Reynolds number that is given as 5×10^5.) From Equation (4.86) for laminar flow, with the Reynolds number based on x_1, we have

$$(C_{f,1})_{\text{laminar}} = \frac{1.328}{\sqrt{\text{Re}_{x_1}}} = \frac{1.328}{\sqrt{5 \times 10^5}} = 0.00188$$

The value of $(C_{f,c})_{\text{turbulent}}$ has already been calculated in Example 4.8, namely,

$$(C_{f,c})_{\text{turbulent}} = 0.00372 \quad \text{(for one side)}$$

From Equation (4.88) with the Reynolds number based on x_1,

$$(C_{f,1})_{\text{turbulent}} = \frac{0.074}{\text{Re}_{x_1}^{1/5}} = \frac{0.074}{(5 \times 10^5)^{0.2}} = 0.00536$$

Inserting these values into Equation (4.93), we have

$$C_f = 0.1613(0.00188) + 0.00372 - 0.1613(0.00536) = 0.003158$$

Taking into account both sides of the flat plate,

$$\text{Net } C_f = 2(0.003158) = \boxed{0.0063}$$

From the data in Figure 4.11, the measured airfoil drag coefficient is 0.0068, which includes *both* skin friction drag and pressure drag due to flow separation. The result from Example 4.10, therefore, is qualitatively reasonable, giving a skin friction drag coefficient slightly less than the measure total drag coefficient. However, our calculated result of $C_f = 0.0063$ is for a critical Reynolds number of 500,000 for transition from laminar to turbulent flow. We do not know what the critical Reynolds number is for the experiments on which the data in Figure 4.11 are based. In Example 4.10, the assumption of $\mathrm{Re}_{x_{\mathrm{cr}}} = 500,000$ is very conservative; more likely the actual value is closer to 1,000,000. If we assume this higher value of $\mathrm{Re}_{x_{\mathrm{cr}}}$, what does it do to the calculated result for C_f? Let us take a look.

EXAMPLE 4.11

Repeat Example 4.10, but assuming the critical Reynolds number is 1×10^6.

■ **Solution**

$$\frac{x_1}{c} = \frac{1 \times 10^6}{3.1 \times 10^6} = 0.3226$$

Which, as we could write down immediately, is twice the length from Example 4.10 because the critical Reynolds number is twice as large. Equation (4.93) becomes

$$C_f = 0.3226(C_{f,1})_{\text{laminar}} + (C_{f,c})_{\text{turbulent}} - 0.3226(C_{f,1})_{\text{turbulent}} \qquad (4.94)$$

For region 1, we have

$$(C_{f,1})_{\text{laminar}} = \frac{1.328}{\sqrt{\mathrm{Re}_{x_1}}} = \frac{1.328}{\sqrt{1 \times 10^6}} = 0.001328$$

The value of $(C_{f,c})_{\text{turbulent}}$ is the same as before:

$$(C_{f,c})_{\text{turbulent}} = 0.00372$$

Once again, for region 1 assuming turbulent flow, we have

$$(C_{f,1})_{\text{turbulent}} = \frac{0.074}{(\mathrm{Re}_{x_1})^{1/5}} = \frac{0.074}{(1 \times 10^6)^{1/5}} = 0.004669$$

Substituting the above results in Equation (4.94), we have

$$C_f = 0.3226(0.001328) + 0.00372 - 0.3226(0.004669) = 0.002642$$

Since this result is for one side of the plate, the net skin friction drag coefficient is

$$\text{Net } C_f = 2(0.002642) = \boxed{0.00528}$$

Note: Comparing the results from Examples 4.10 and 4.11, we see that an increase in $\mathrm{Re}_{x_{\mathrm{cr}}}$ from 500,000 to 1,000,000 resulted in a skin friction drag coefficient that is 16 percent smaller. This difference underscores the importance of knowing where transition takes place on a surface for the calculation of skin friction drag.

Also, comparing the calculated results for skin friction drag coefficient with the measured total drag coefficient of 0.0068, from Example 4.10 the calculated $C_f = 0.0063$ would imply that the pressure drag due to flow separation is about 7.4 percent of the total drag. The result from Example 4.11 of $C_f = 0.00528$ would imply that the pressure drag due to flow separation is about 22 percent of the total drag.

Is this breakdown between skin friction and pressure drag quantitatively reasonable? An answer can be found in the recent results of Lombardi *et al.* given in Reference 92. Here, the authors calculated both the skin friction drag coefficient and the total drag coefficient for an NACA 0012 airfoil using an accurate computational fluid dynamic technique. More details of their calculations are given in Section 20.4. For a Reynolds number based on chord length of 3×10^6, and including a model for transition, they calculated a total drag coefficient of 0.00623 and a skin friction drag coefficient of 0.00534, indicating that the pressure drag due to flow separation is 15 percent of the total drag. For a streamlined body, this drag breakdown is reasonable; the drag on a streamlined two-dimensional shape is mostly skin friction drag, and by comparison the pressure drag is small. For example, it is reasonable to expect 80 percent of the drag to be skin friction drag and 20 percent to be pressure drag due to flow separation.

This is not to say that pressure drag due to flow separation is unimportant; quite the contrary, as the body becomes less streamlined (more like a blunt body), the pressure drag becomes the dominant factor. We need to take a closer look at this phenomenon.

4.12.4 Flow Separation

Pressure drag on an airfoil is caused by the flow separation. For a completely attached flow over an airfoil, the pressure acting on the rear surface gives rise to a force in the forward direction which completely counteracts the pressure acting on the front surface producing a force in the rearward direction, resulting in zero pressure drag. However, if the flow is partially separated over the rear surface, the pressure on the rear surface pushing forward will be smaller than the fully attached case, and the pressure acting on the front surface pushing backwards will not be fully counteracted, giving rise to a net pressure drag on the airfoil—the pressure drag due to flow separation.

What flow conditions are conducive to flow separation? To help answer this question, consider the flow over the NASA LS(1)-0417 airfoil at zero angle of attack, as shown in Figure 4.45. The streamlines move smoothly over the airfoil— there is no flow separation of any consequence. A computational fluid dynamic solution of the variation of pressure coefficient over the upper surface of the airfoil is shown at the bottom of Figure 4.45. Starting at the stagnation point at the leading edge, where for incompressible flow $C_p = 1.0$, the flow rapidly expands around the top surface. The pressure decreases dramatically, dipping to a minimum pressure at a location about 10 percent of the chord length downstream of the leading edge. Then as the flow moves farther downstream, the pressure
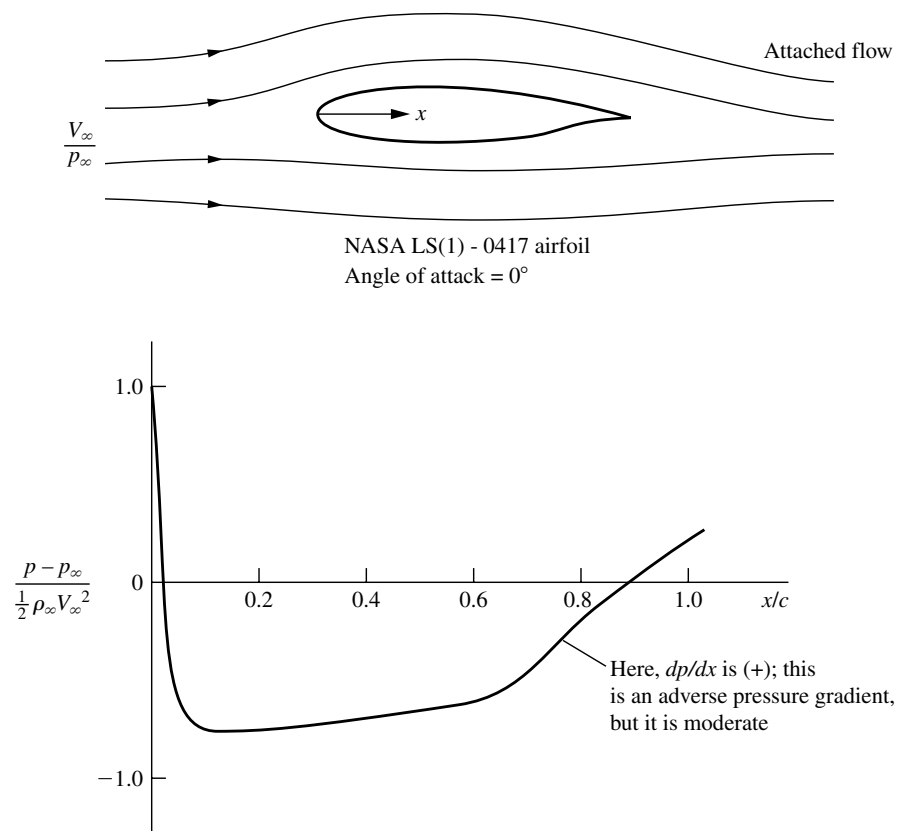
NASA LS(1) - 0417 airfoil
Angle of attack = 0°

Figure 4.45 Pressure distribution over the top surface for attached flow over an airfoil. Theoretical data for a modern NASA low-speed airfoil, from NASA Conference Publication 2046, *Advanced Technology Airfoil Research,* vol. II, March 1978, p. 11 (*Source:* After McGhee, Beasley, and Whitcomb).

gradually increases, reaching a value slightly above free-stream pressure at the trailing edge. This region of increasing pressure is called a region of *adverse* pressure gradient. By definition, an adverse pressure gradient is a region where the pressure *increases in the flow direction,* that is, in Figure 4.45, the region where dp/dx is *positive*. For the conditions shown in Figure 4.45, the adverse pressure gradient is moderate; that is, dp/dx is small, and for all practical purposes the flow remains attached to the airfoil surface except for a small region near the trailing edge (not shown in Figure 4.45).

Now consider the same airfoil at the very high angle of attack of 18.4 degrees, as shown in Figure 4.46. First, assume we have a purely inviscid flow with no flow separation—a purely artificial situation. A numerical solution for the inviscid flow gives the results shown by the dashed curve in Figure 4.46. In this artificial situation, the pressure would drop precipitously downstream of the leading edge to a value of C_p almost -9, and then rapidly increase downstream, recovering

NASA LS(1) - 0417 airfoil
Angle of attack = 18.4°

$$\frac{p - p_\infty}{\frac{1}{2}\rho_\infty V_\infty^2}$$

Pressure distribution
with separation

Pressure distribution if there
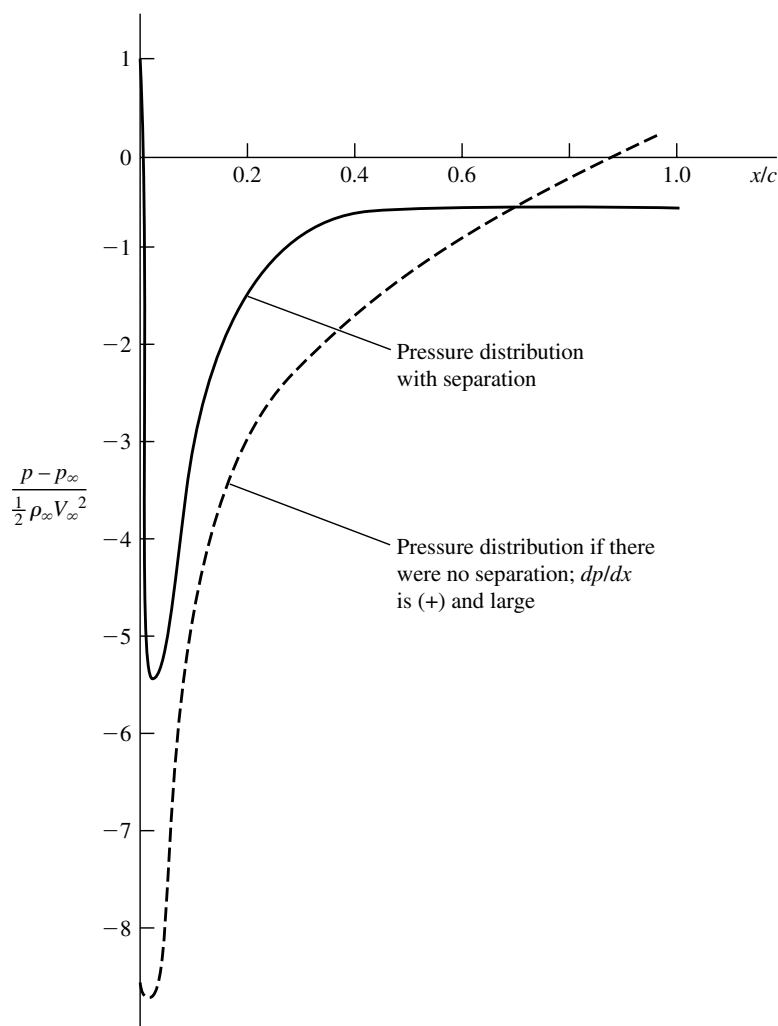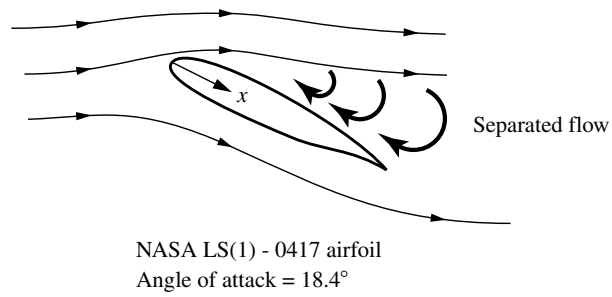were no separation; dp/dx
is (+) and large

Figure 4.46 Pressure distribution over the top surface for separated flow
over an airfoil. Theoretical data for a modern NASA low-speed airfoil, from
NASA Conference Publication 2045, Part 1, *Advanced Technology Airfoil
Research,* vol. 1, March 1978, p. 380. (*Source:* After Zumwalt and Nack).

Note: Length of the arrows denoting pressure is proportional to $p - p_{ref}$, where p_{ref} is an arbitrary reference pressure slightly less than the minimum pressure on the airfoil
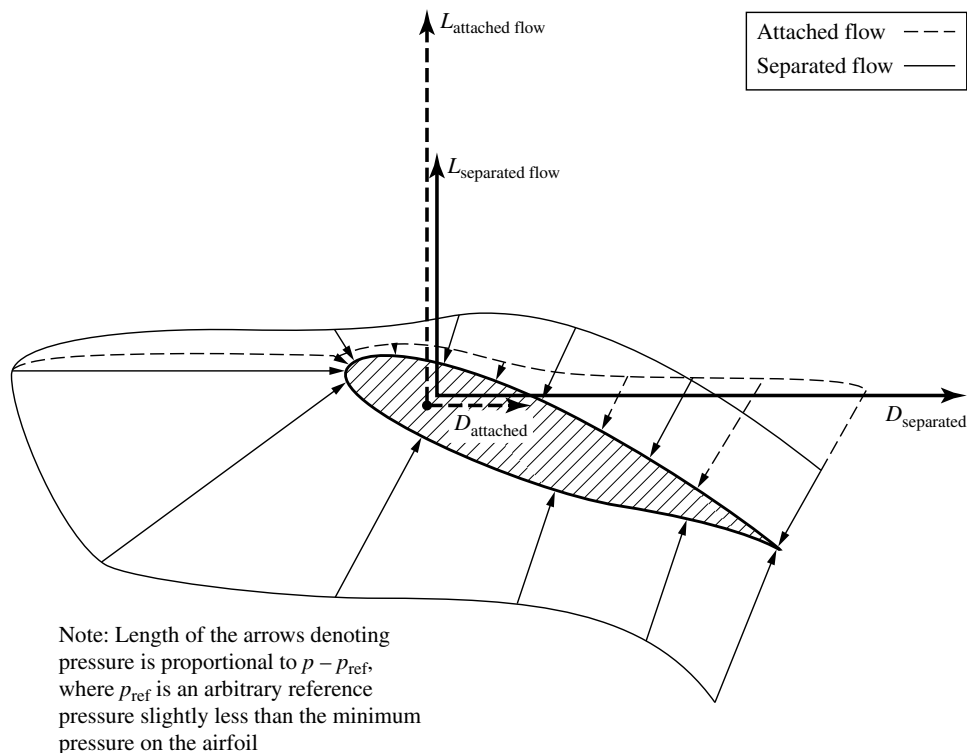
Figure 4.47 Qualitative comparison of pressure distribution, lift, and drag for attached and separated flows. Note that for separated flow, the lift decreases and the drag increases.

to a value slightly above p_∞ at the trailing edge. In this recovery, the pressure would increase rapidly, in contrast to the case shown in Figure 4.45. The adverse pressure gradient would be severe; that is, dp/dx would be large. In such a case, the *real* viscous flow tends to separate from the surface. In this real separated flow, the *actual* surface pressure distribution is given in Figure 4.46 by the *solid* curve, obtained from a computational fluid dynamic viscous flow calculation using the complete Navier-Stokes equations (see Chapter 15). In comparison to the dashed curve, the actual pressure distribution does not dip to as low a pressure minimum, and the pressure near the trailing edge does not recover to a value above p_∞.

It is important to visualize and compare the pressures acting on the surface of the airfoil for the case shown in Figure 4.46, this comparison is sketched in Figure 4.47. Here the airfoil at a large angle of attack (thus with flow separation) is shown with the real surface pressure distribution symbolized by the solid arrows. Pressure always acts normal to the surface. Hence the arrows are all locally perpendicular to the surface. The length of the arrows is representative of the magnitude of the pressure. A solid curve is drawn through the base of the arrows to form an "envelope" to make the pressure distribution easier to visualize. However, if the flow were *not* separated, that is, if the flow were attached, then the pressure distribution would be that shown by the dashed arrows (and the dashed envelope).

The solid and dashed arrows in Figure 4.47 qualitatively correspond to the solid and dashed pressure distribution curves, respectively, in Figure 4.46.

The solid and dashed arrows in Figure 4.47 should be compared carefully. They explain the two major consequences of separated flow over the airfoil. The first consequence is a loss of lift. The aerodynamic lift (the vertical force shown in Figure 4.47) is derived from the net component of the pressure distribution in the vertical direction in Figure 4.47 (assuming that the free stream relative wind is horizontal in this figure). High lift is obtained when the pressure on the bottom surface is large and the pressure on the top surface is small. Separation does not affect the bottom surface pressure distribution. However, comparing the solid and dashed arrows on the top surface *just downstream of the leading edge,* we find the solid arrows indicating a higher pressure when the flow is separated. This higher pressure is pushing down, hence reducing the lift. This reduction in lift is also compounded by the geometric effect that the position of the top surface of the airfoil near the leading edge is approximately horizontal in Figure 4.47. When the flow is separated, causing a higher pressure on this part of the airfoil surface, the direction in which the pressure is acting is closely aligned to the vertical, and hence, almost the full effect of the increased pressure is felt by the lift. The combined effect of the increased pressure on the top surface near the leading edge, and the fact that this portion of the surface is approximately horizontal, leads to the rather dramatic loss of lift when the flow separates. Note in Figure 4.47 that the lift for separated flow (the solid vertical vector) is smaller than the lift that would exist if the flow were attached (the dashed vertical vector).

Now let us concentrate on that portion of the top surface *near the trailing edge*. On this portion of the airfoil surface, the pressure for the separated flow is now *smaller* than the pressure that would exist if the flow were attached. Moreover, the top surface near the trailing edge geometrically is inclined more to the horizontal, and, in fact, somewhat faces in the horizontal direction. Recall that the drag is in the horizontal direction in Figure 4.47. Because of the inclination of the top surface near the trailing edge, the pressure exerted on this portion of the surface has a strong component in the horizontal direction. This component acts towards the left, tending to counter the horizontal component of force due to the high pressure acting on the nose of the airfoil pushing toward the right. The net pressure drag on the airfoil is the difference between the force exerted on the front pushing toward the right and the force exerted on the back pushing toward the left. When the flow is separated, the pressure on the back is lower than it would be if the flow were attached. Hence, for the separated flow, there is *less* force on the back pushing toward the left, and the *net* drag acting toward the right is therefore *increased*. Note in Figure 4.47 that the drag for separated flow (the solid horizontal vector) is larger than the drag that would exist if the flow were attached (the dashed horizontal vector).

Therefore, two major consequences of the flow separating over an airfoil are:

1. A drastic loss of lift (stalling).
2. A major increase in drag, caused by pressure drag due to flow separation.

Why does a flow separate from a surface? The answer is addressed in detail in Section 15.2. In brief, in a region of adverse pressure gradient the fluid elements moving along a streamline have to work their way "uphill" against an increasing pressure. Consequently, the fluid elements will slow down under the influence of an adverse pressure gradient. For the fluid elements moving outside the boundary layer, where the velocity (and hence kinetic energy) is high, this is not much of a problem. The fluid elements keep moving downstream. However, consider a fluid element deep inside the boundary layer. Its velocity is already small because it is retarded by friction forces. The fluid element still encounters the same adverse pressure gradient because the pressure is transmitted without change normal to the wall, but its velocity is too low to negotiate the increasing pressure. As a result, the element comes to a stop somewhere downstream and reverses its direction. Such reversed flow causes the flow field in general to separate from the surface, as shown at the top of Figure 4.46. This is physically how separated flow develops.

4.12.5 Comment

In this section we estimated skin friction drag on an airfoil by using the model of a flat plate at zero angle of attack, and calculating the skin friction drag for the airfoil using the formulas for the flat plate such as Equations (4.86) for laminar flow and Equation (4.88) for turbulent flow.[5] How reasonable is this? How close does the flat plate skin friction drag on a flat plate come to that on an airfoil? How close does the local shear stress distribution over the surface of the flat plate resemble that on the airfoil surface?

Some answers can be obtained by comparing the relatively exact computational fluid dynamic calculations of Lombardi et al. (Reference 92) for the viscous flow over an NACA 0012 airfoil at zero angle of attack with that for a flat plate. The variation of the local skin friction coefficient, defined as $c_f = \tau_w/q_\infty$, as a function of distance from the leading edge is given in Figure 4.48 for both the airfoil and the flat plate. They are remarkably close; clearly, for the purpose of the present section the modeling of the airfoil skin friction drag by use of flat plate results is reasonable.

With this, we end our discussion of airfoil drag at low speeds. Although the main thrust of this chapter is the low-speed inviscid potential flow over airfoils with the consequent prediction of lift, the present section provides some balance by exploring the effects of viscous flow on airfoil behavior, and the consequent production of drag. More aspects of the real flow over airfoils are given in Section 4.13.

---

[5] In 1921, Walter Diehl's article in NACA TR111, entitled "The Variation of Aerofoil Lift and Drag Coefficients with Changes in Size and Speed," suggested that the airfoil drag coefficient varies in the same manner as that for a flat plate at zero angle of attack. He did not say that the airfoil drag coefficient equals that for a flat plate, but rather has the same Reynolds number variation. Diehl's suggestion, however, appears to be the first effort to use flat plate data in some fashion to estimate airfoil drag.
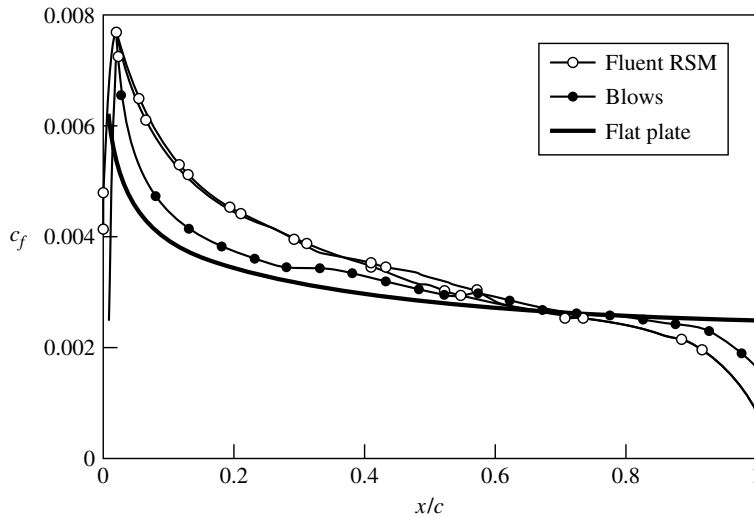
Figure 4.48 Local skin-friction coefficient distributions over an NACA 0012 airfoil, compared with that for a flat plate.

4.13 APPLIED AERODYNAMICS: THE FLOW OVER AN AIRFOIL—THE REAL CASE

In this chapter, we have studied the inviscid, incompressible flow over airfoils. When compared with actual experimental lift and moment data for airfoils in low-speed flows, we have seen that our theoretical results based on the assumption of inviscid flow are quite good—with one glaring exception. In the real case, flow separation occurs over the top surface of the airfoil when the angle of attack exceeds a certain value—the "stalling" angle of attack. As described in Sections 4.3 and 4.12, this is a viscous effect. As shown in Figure 4.9, the lift coefficient reaches a local maximum denoted by $c_{l,\max}$, and the angle of attack at which $c_{l,\max}$ is achieved is the stalling angle of attack. An increase in α beyond this value usually results in a (sometimes rather precipitous) drop in lift. At angles of attack well below the stalling angle, the experimental data clearly show a *linear* increase in c_l with increasing α—a result that is predicted by the theory presented in this chapter. Indeed, in this linear region, the inviscid flow theory is in excellent agreement with the experiment, as reflected in Figure 4.10 and as demonstrated by Example 4.6. However, the inviscid theory does not predict flow separation, and consequently the prediction of $c_{l,\max}$ and the stalling angle of attack must be treated in some fashion by viscous flow theory. Such viscous flow analyses are the purview of Part 4. On the other hand, the purpose of this section is to examine the *physical* features of the real flow over an airfoil, and flow separation is an inherent part of this real flow. Therefore, let us take a more detailed look at how the flow field over an airfoil changes as the angle of attack is increased, and how the lift coefficient is affected by such changes.

The flow fields over an NACA 4412 airfoil at different angles of attack are shown in Figure 4.49. Here, the streamlines are drawn to scale as obtained from
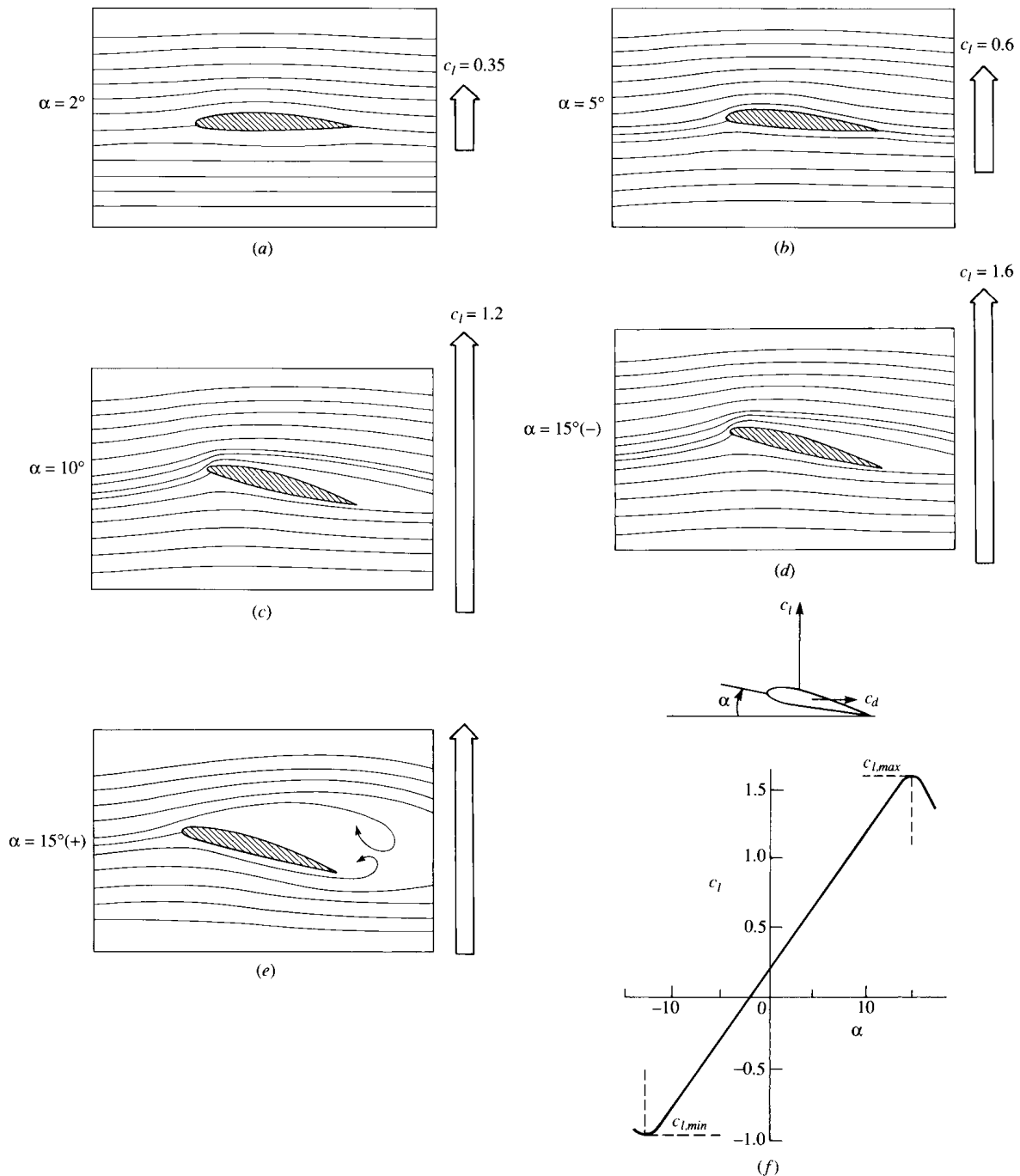
Figure 4.49 Example of leading-edge stall. Streamline patterns for an NACA 4412 airfoil at different angles of attack. *(The streamlines are drawn to scale from experimental data given by Hikaru Ito in Reference 50.)* $Re = 2.1 \times 10^5$ and $V_\infty = 8$ m/s in air. The corresponding experimentally measured lift coefficients are indicated by arrows at the right of each streamline picture, where the length of each arrow indicates the relative magnitude of the lift. The lift coefficient is also shown in part (f).

the experimental results of Hikaru Ito given in Reference 50. The experimental streamline patterns were made visible by a smoke wire technique, wherein metallic wires spread with oil over their surfaces were heated by an electric pulse and the resulting white smoke creates visible streaklines in the flow field. In Figure 4.49, the angle of attack is progressively increased as we scan from Figure 4.49*a* to *e*; to the right of each streamline picture is an arrow, the length of which is proportional to the value of the lift coefficient at the given angle of attack. The actual experimentally measured lift curve for the airfoil is given in Figure 4.49*f*. Note that at low angle of attack, such as $\alpha = 2°$ in Figure 4.49*a*, the streamlines are relatively undisturbed from their freestream shapes and c_l is small. As α is increased to $5°$, as shown in Figure 4.49*b*, and then to $10°$, as shown in Figure 4.49*c*, the streamlines exhibit a pronounced upward deflection in the region of the leading edge, and a subsequent downward deflection in the region of the trailing edge. Note that the stagnation point progressively moves downstream of the leading edge over the bottom surface of the airfoil as α is increased. Of course, c_l increases as α is increased, and, in this region, the increase is linear, as seen in Figure 4.49*f*. When α is increased to slightly less than $15°$, as shown in Figure 4.49*d*, the curvature of the streamlines is particularly apparent. In Figure 4.49*d*, the flow field is still attached over the top surface of the airfoil. However, as α is further increased slightly above $15°$, massive flow-field separation occurs over the top surface, as shown in Figure 4.49*e*. By slightly increasing α from that shown in Figure 4.49*d* to that in Figure 4.49*e*, the flow quite suddenly separates from the leading edge and the lift coefficient experiences a precipitous decrease, as seen in Figure 4.49*f*.

The type of stalling phenomenon shown in Figure 4.49 is called *leading-edge stall*; it is characteristic of relatively thin airfoils with thickness ratios between 10 and 16 percent of the chord length. As seen above, flow separation takes place rather suddenly and abruptly over the entire top surface of the airfoil, with the origin of this separation occurring at the leading edge. Note that the lift curve shown in Figure 4.49*f* is rather sharp-peaked in the vicinity of $c_{l,\max}$ with a rapid decrease in c_l above the stall.

A second category of stall is the *trailing-edge stall*. This behavior is characteristic of thicker airfoils such as the NACA 4421 shown in Figure 4.50. Here, we see a progressive and gradual movement of separation from the trailing edge toward the leading edge as α is increased. The lift curve for this case is shown in Figure 4.51. The solid curve in Figure 4.51 is a repeat of the results for the NACA 4412 airfoil shown earlier in Figure 4.49*f*—an airfoil with a leading-edge stall. The dot-dashed curve is the lift curve for the NACA 4421 airfoil—an airfoil with a trailing-edge stall. In comparing these two curves, note that:

1. The trailing-edge stall yields a gradual bending-over of the lift curve at maximum lift, in contrast to the sharp, precipitous drop in c_l for the leading-edge stall. The stall is "soft" for the trailing-edge stall.
2. The value of $c_{l,\max}$ is not so large for the trailing-edge stall.
3. For both the NACA 4412 and 4421 airfoils, the shape of the mean camber line is the same. From the thin airfoil theory discussed in this chapter, the
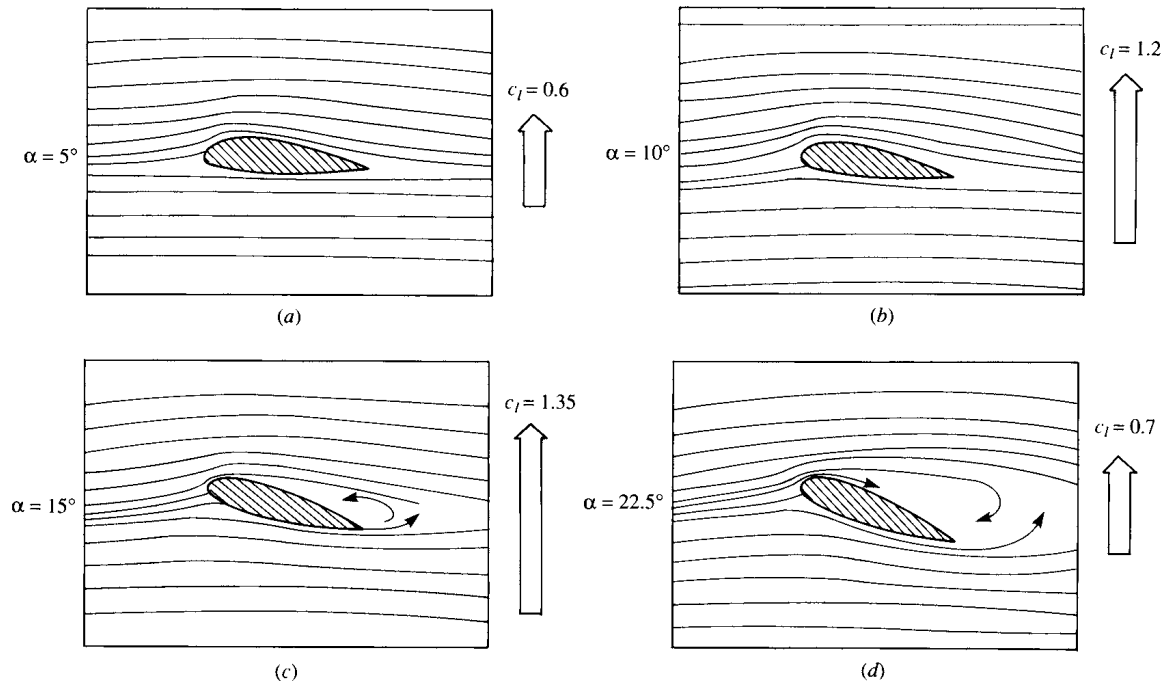
Figure 4.50 Example of trailing-edge stall. Streamline patterns for an NACA 4421 airfoil at different angles of attack. *(The streamlines are drawn to scale from the experimental results of Hikaro Ito in Reference 50.)* $Re = 2.1 \times 10^5$ and $V_\infty = 8$ m/s in air.

linear lift slope and the zero-lift angle of attack should be the same for both airfoils; this is confirmed by the experimental data in Figure 4.51. The only difference between the two airfoils is that one is thicker than the other. Hence, comparing results shown in Figures 4.49 to 4.51, we conclude that the major effect of thickness of the airfoil is its effect on the value of $c_{l,\max}$, and this effect is mirrored by the leading-edge stall behavior of the thinner airfoil versus the trailing-edge stall behavior of the thicker airfoil.

There is a third type of stall behavior, namely, behavior associated with the extreme thinness of an airfoil. This is sometimes labeled as "thin airfoil stall." An extreme example of a very thin airfoil is a flat plate; the lift curve for a flat plate is shown as the dashed curve in Figure 4.51 labeled "thin airfoil stall." The streamline patterns for the flow over a flat plate at various angles of attack are given in Figure 4.52. The thickness of the flat plate is 2 percent of the chord length. Inviscid, incompressible flow theory shows that the velocity becomes infinitely large at a sharp convex corner; the leading edge of a flat plate at an angle of attack is such a case. In the real flow over the plate as shown in Figure 4.52, nature addresses this singular behavior by having the flow separate at the leading edge, even for very low values of α. Examining Figure 4.52a, where $\alpha = 3°$, we observe a small region of separated flow at the leading edge. This separated
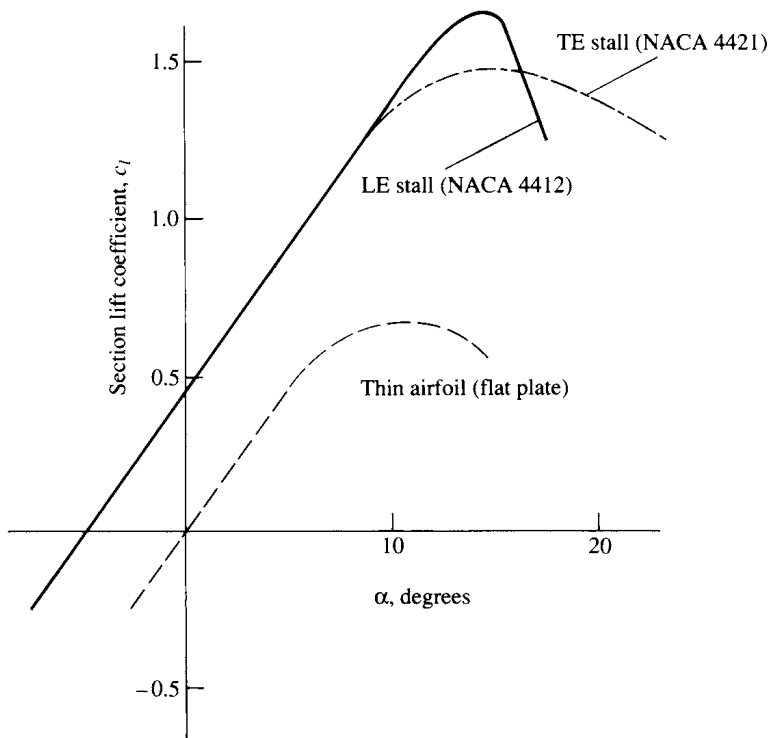
Figure 4.51 Lift-coefficient curves for three airfoils with different aerodynamic behavior: trailing-edge stall (NACA 4421 airfoil), leading-edge stall (NACA 4412 airfoil), thin airfoil stall (flat plate).
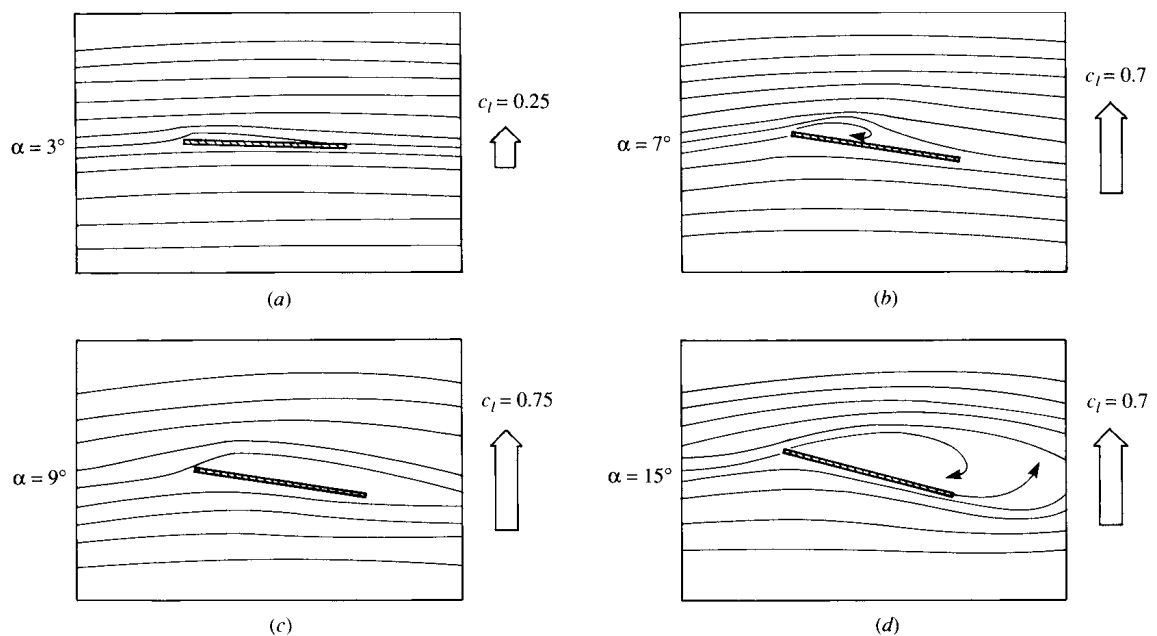

Figure 4.52 Example of thin airfoil stall. Streamline patterns for a flat plate at angle of attack. *(The streamlines are drawn to scale from the experimental data of Hikaru Ito in Reference 50.)*

flow reattaches to the surface further downstream, forming a *separation bubble* in the region near the leading edge. As α is increased, the reattachment point moves further downstream; that is, the separation bubble becomes larger. This is illustrated in Figure 4.52b where $\alpha = 7°$. At $\alpha = 9°$ (Figure 4.52c), the separation bubble extends over almost the complete flat plate. Referring back to Figure 4.51, we note that this angle of attack corresponds to $c_{l,\max}$ for the flat plate. When α is increased further, total flow separation is present, such as shown in Figure 4.52d. The lift curve for the flat plate in Figure 4.51 shows an early departure from its linear variation at about $\alpha = 3°$; this corresponds to the formation of the leading-edge separation bubble. The lift curve gradually bends over as α is increased further and exhibits a very gradual and "soft" stall. This is a trend similar to the case of the trailing-edge stall, although the physical aspects of the flow are quite different between the two cases. Of particular importance is the fact that $c_{l,\max}$ for the flat plate is considerably smaller than that for the two NACA airfoils compared in Figure 4.51. Hence, we can conclude from Figure 4.51 that the value of $c_{l,\max}$ is critically dependent on airfoil thickness. In particular, by comparing the flat plate with the two NACA airfoils, we see that *some* thickness is vital to obtaining a high value of $c_{l,\max}$. However, beyond that, the amount of thickness will influence the type of stall (leading-edge versus trailing-edge), and airfoils that are very thick tend to exhibit reduced values of $c_{l,\max}$ as the thickness increases. Hence, if we plot $c_{l,\max}$ versus thickness ratio, we expect to see a local maximum. Such is indeed the case, as shown in Figure 4.53. Here, experimental data for $c_{l,\max}$ for the NACA 63-2XX series of airfoils is shown as a function of the thickness ratio. Note that as the thickness ratio increases from a small value, $c_{l,\max}$ first increases, reaches a maximum value at a thickness ratio of about 12 percent, and then decreases
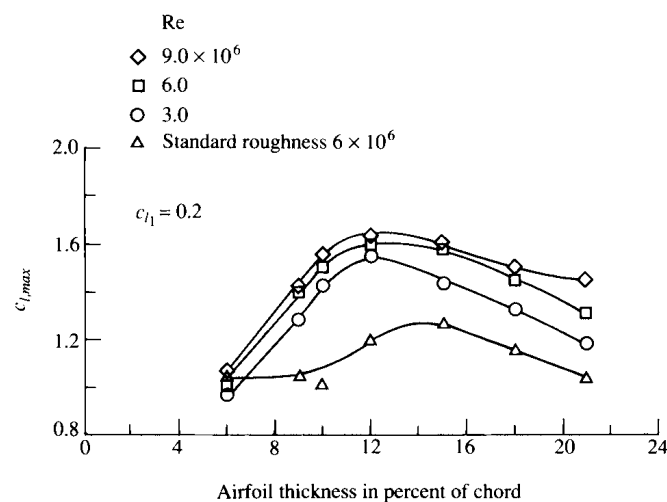

Figure 4.53 Effect of airfoil thickness on maximum lift coefficient for the NACA 63-2XX series of airfoils. *(Source: Abbott and von Doenhoff, Reference 11.)*

at larger thickness ratios. The experimental data in Figure 4.53 is plotted with the Reynolds number as a parameter. Note that $c_{l,\max}$ for a given airfoil is clearly a function of Re, with higher values of $c_{l,\max}$ corresponding to higher Reynolds numbers. Since flow separation is responsible for the lift coefficient exhibiting a local maximum, since flow separation is a viscous phenomenon, and since a viscous phenomenon is governed by a Reynolds number, it is no surprise that $c_{l,\max}$ exhibits some sensitivity to Re.

When was the significance of airfoil thickness first understood and appreciated? This question is addressed in the historical note in Section 4.14, where we will see that the aerodynamic properties of thick airfoils even transcended technology during World War I and impacted the politics of the armistice.

Let us examine some other aspects of airfoil aerodynamics—aspects that are not always appreciated in a first study of the subject. The simple generation of lift by an airfoil is not the prime consideration in its design—even a barn door at an angle of attack produces lift. Rather, there are two figures of merit that are primarily used to judge the quality of a given airfoil:

1. *The lift-to-drag ratio L/D.* An efficient airfoil produces lift with a minimum of drag; that is, the ratio of lift-to-drag is a measure of the aerodynamic efficiency of an airfoil. The standard airfoils discussed in this chapter have high L/D ratios—much higher than that of a barn door. The L/D ratio for a complete flight vehicle has an important impact on its flight performance; for example, the range of the vehicle is directly proportional to the L/D ratio. (See Reference 2 for an extensive discussion of the role of L/D on flight performance of an airplane.)

2. *The maximum lift coefficient $c_{l,\max}$.* An effective airfoil produces a high value of $c_{l,\max}$—much higher than that produced by a barn door.

The maximum lift coefficient is worth some additional discussion here. For a complete flight vehicle, the maximum lift coefficient $C_{L,\max}$ determines the stalling speed of the aircraft as discussed in the Design Box at the end of Section 1.8. From Equation (1.47), repeated below:

$$V_{\text{stall}} = \sqrt{\frac{2W}{\rho_\infty S C_{L,\max}}} \qquad (1.47)$$

Therefore, a tremendous incentive exists to increase the maximum lift coefficient of an airfoil, in order to obtain either lower stalling speeds or higher payload weights at the same speed, as reflected in Equation (1.47). Moreover, the maneuverability of an airplane (i.e., the smallest possible turn radius and the fastest possible turn rate) depends on a large value of $C_{L,\max}$ (see Section 6.17 of Reference 2). On the other hand, for an airfoil at a given Reynolds number, the value of $c_{l,\max}$ is a function primarily of its shape. Once the shape is specified, the value of $c_{l,\max}$ is what nature dictates, as we have already seen. Therefore, to increase $c_{l,\max}$ beyond such a value, we must carry out some special measures. Such special measures include the use of flaps and/or leading-edge slats to increase
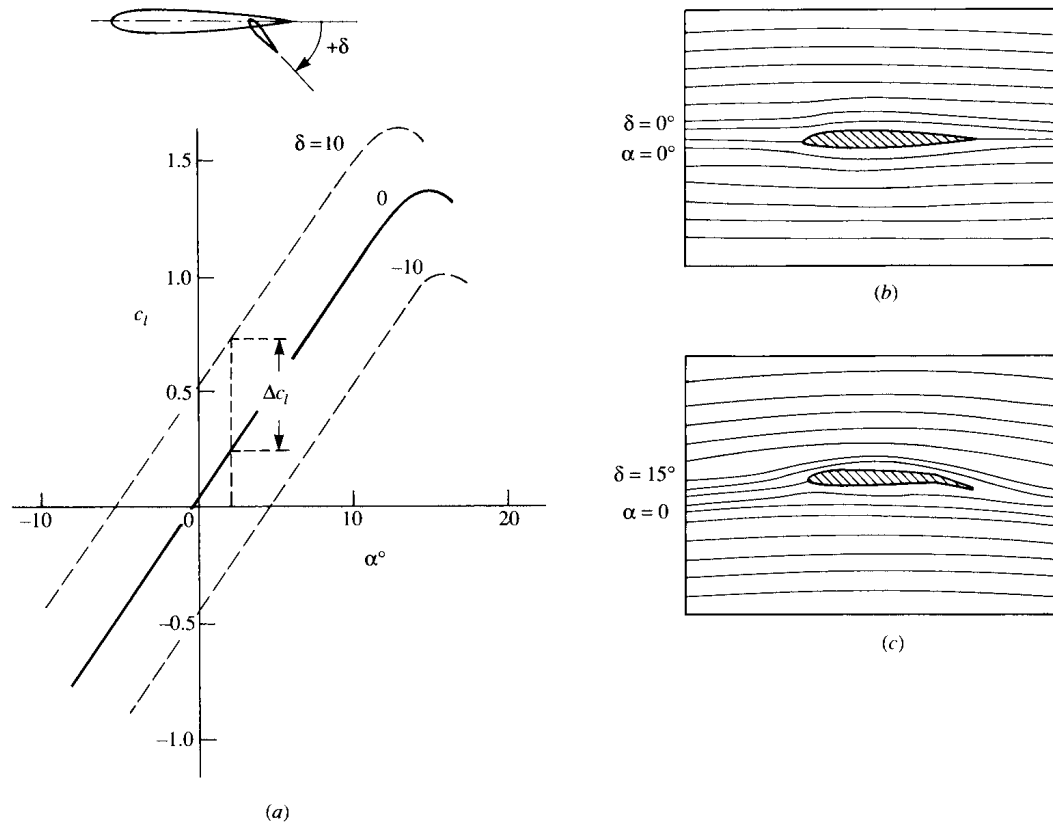
Figure 4.54 Effect of flap deflection on streamline shapes. *(The streamlines are drawn to scale from the experimental data of Hikaru Ito in Reference 50.)* (*a*) Effect of flap deflection on lift coefficient. (*b*) Streamline pattern with no flap deflection. (*c*) Streamline pattern with a 15° flap deflection.

$c_{l,\max}$ above that for the reference airfoil itself. These are called *high-lift devices,* and are discussed in more detail below.

A trailing-edge flap is simply a portion of the trailing-edge section of the airfoil that is hinged and which can be deflected upward or downward, as sketched in the insert in Figure 4.54*a*. When the flap is deflected downward (a positive angle δ in Figure 4.54*a*), the lift coefficient is increased, as shown in Figure 4.54*a*. This increase is due to an effective increase in the camber of the airfoil as the flap is deflected downward. The thin airfoil theory presented in this chapter clearly shows that the zero-lift angle of attack is a function of the amount of camber [see Equation (4.61)], with $\alpha_{L=0}$ becoming more negative as the camber is increased. In terms of the lift curve shown in Figure 4.54*a*, the original curve for no flap deflection goes through the origin because the airfoil is symmetric; however, as the flap is deflected downward, this lift curve simply translates to the left because $\alpha_{L=0}$ is becoming more negative. In Figure 4.54*a*, the results are given for flap deflections of $\pm 10°$. Comparing the case for $\delta = 10°$ with the no-deflection
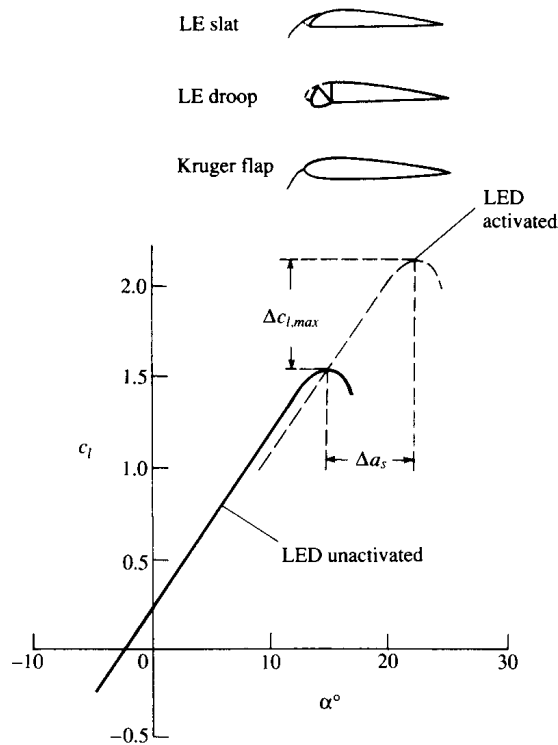
Figure 4.55 Effect of leading-edge flap on lift coefficient.

case, we see that, at a given angle of attack, the lift coefficient is increased by an amount Δc_l due to flap deflection. Moreover, the actual value of $c_{l,\max}$ is increased by flap deflection, although the angle of attack at which $c_{l,\max}$ occurs is slightly decreased. The change in the streamline pattern when the flap is deflected is shown in Figure 4.54b and c. Figure 4.54b is the case for $\alpha = 0$ and $\delta = 0$ (i.e., a symmetric flow). However, when α is held fixed at zero, but the flap is deflected by 15°, as shown in Figure 4.54c, the flow field becomes unsymmetrical and resembles the lifting flows shown (e.g., in Figure 4.49). That is, the streamlines in Figure 4.54c are deflected upward in the vicinity of the leading edge and downward near the trailing edge, and the stagnation point moves to the lower surface of the airfoil—just by deflecting the flap downward.

High-lift devices can also be applied to the leading edge of the airfoil, as shown in the insert in Figure 4.55. These can take the form of a leading-edge slat, leading-edge droop, or a leading-edge flap. Let us concentrate on the leading-edge slat, which is simply a thin, curved surface that is deployed in front of the leading edge. In addition to the primary airflow over the airfoil, there is now a secondary flow that takes place through the gap between the slat and the airfoil leading edge. This secondary flow from the bottom to the top surface modifies
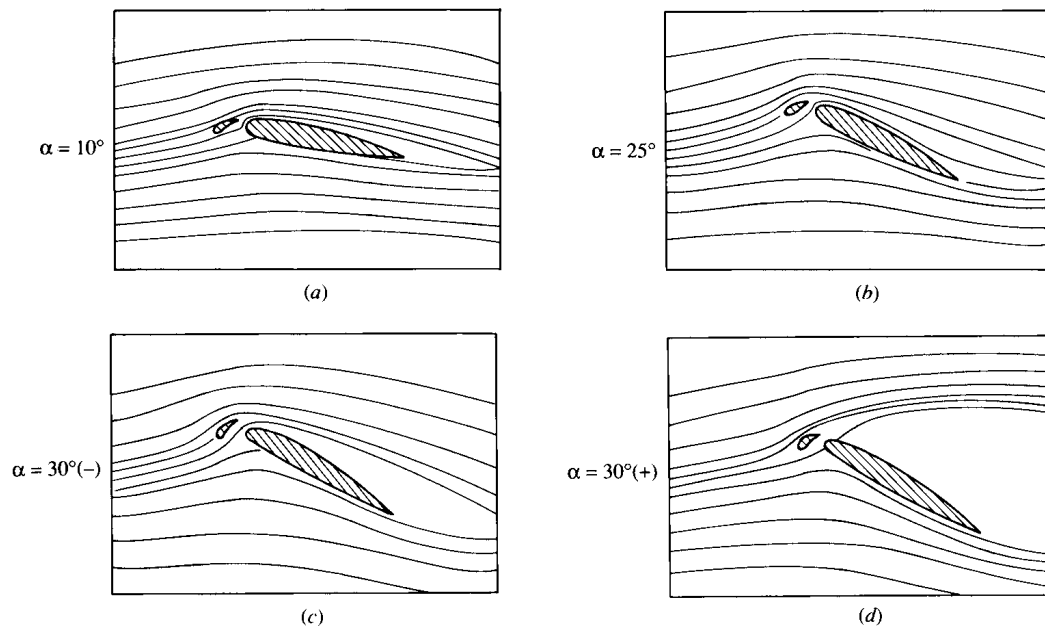
Figure 4.56 Effect of a leading-edge slat on the streamline pattern over an NACA 4412 airfoil. *(The streamlines are drawn to scale from the experimental data in Reference 50.)*

the pressure distribution over the top surface; the adverse pressure gradient which would normally exist over much of the top surface is mitigated somewhat by this secondary flow, hence delaying flow separation over the top surface. Thus, a leading-edge slat increases the stalling angle of attack, and hence yields a higher $c_{l,\max}$, as shown by the two lift curves in Figure 4.55, one for the case without a leading-edge device and the other for the slat deployed. Note that the function of a leading-edge slat is inherently different from that of a trailing-edge flap. There is no change in $\alpha_{L=0}$; rather, the lift curve is simply extended to a higher stalling angle of attack, with the attendant increase in $c_{l,\max}$. The streamlines of a flow field associated with an extended leading-edge slat are shown in Figure 4.56. The airfoil is in an NACA 4412 section. (*Note:* The flows shown in Figure 4.56 do not correspond exactly with the lift curves shown in Figure 4.55, although the general behavior is the same.) The stalling angle of attack for the NACA 4412 airfoil without slat extension is about 15°, but increases to about 30° when the slat is extended. In Figure 4.56a, the angle of attack is 10°. Note the flow through the gap between the slat and the leading edge. In Figure 4.56b, the angle of attack is 25° and the flow is still attached. This prevails to an angle of attack slightly less than 30°, as shown in Figure 4.56c. At slightly higher than 30° flow separation suddenly occurs and the airfoil stalls.

The high-lift devices used on modern, high-performance aircraft are usually a combination of leading-edge slats (or flaps) and multielement trailing-edge flaps. Typical airfoil configurations with these devices are sketched in Figure 4.57. Three
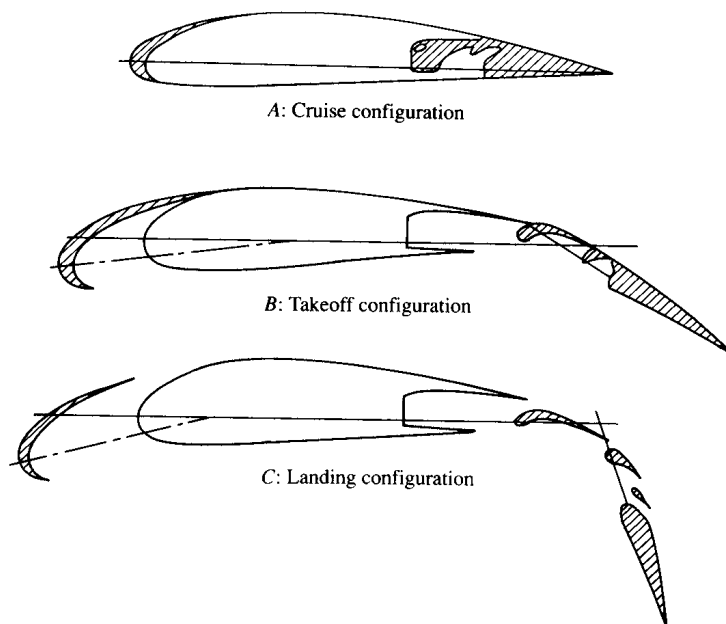
Figure 4.57 Airfoil with leading-edge and trailing-edge high-lift mechanisms. The trailing-edge device is a multielement flap.

configurations including the high-lift devices are shown: *A*—the cruise configuration, with no deployment of the high-lift devices; *B*—a typical configuration at takeoff, with both the leading- and trailing-edge devices partially deployed; and *C*—a typical configuration at landing, with all devices fully extended. Note that for configuration *C*, there is a gap between the slat and the leading edge and several gaps between the different elements of the multielement trailing-edge flap. The streamline pattern for the flow over such a configuration is shown in Figure 4.58. Here, the leading-edge slat and the multielement trailing-edge flap are fully extended. The angle of attack is 25°. Although the main flow over the top surface of the airfoil is essentially separated, the local flow through the gaps in the multielement flap is locally attached to the top surface of the flap; because of this locally attached flow, the lift coefficient is still quite high, on the order of 4.5.

With this, we end our discussion of the real flow over airfoils. In retrospect, we can say that the real flow at high angles of attack is dominated by flow separation—a phenomenon that is not properly modeled by the inviscid theories presented in this chapter. On the other hand, at lower angles of attack, such as those associated with the cruise conditions of an airplane, the inviscid theories presented here do an excellent job of predicting both lift and moments on an airfoil. Moreover, in this section, we have clearly seen the importance of airfoil *thickness* in determining the angle of attack at which flow separation will occur, and hence greatly affecting the maximum lift coefficient.
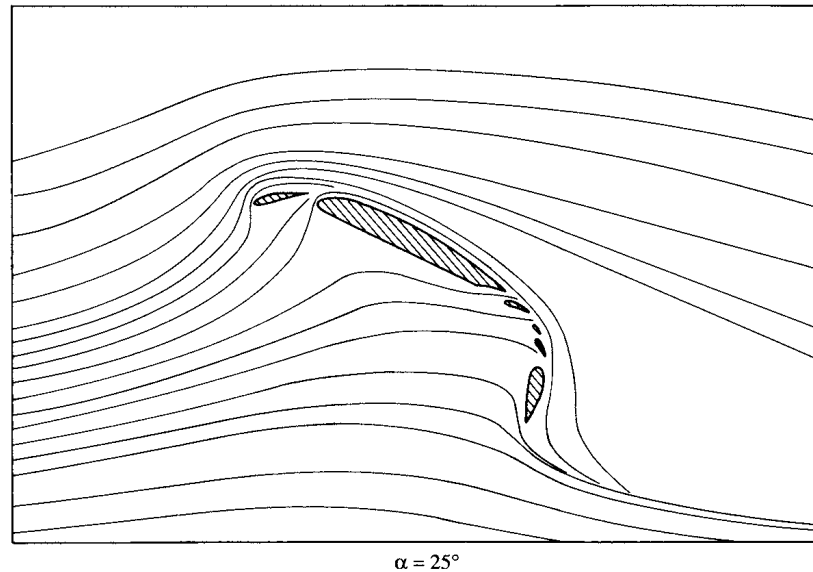
$$\alpha = 25°$$

Figure 4.58 Effect of leading-edge and multielement flaps on the streamline pattern around an airfoil at angle of attack of 25°. *(The streamlines are drawn to scale from the experimental data of Reference 50.)*

4.14 HISTORICAL NOTE: EARLY AIRPLANE DESIGN AND THE ROLE OF AIRFOIL THICKNESS

In 1804, the first modern configuration aircraft was conceived and built by Sir George Cayley in England—it was an elementary hand-launched glider, about a meter in length, and with a kitelike shape for a wing as shown in Figure 4.59. (For the pivotal role played by George Cayley in the development of the airplane, see the extensive historical discussion in chapter 1 of Reference 2.) Note that right from the beginning of the modern configuration aircraft, the wing sections were very thin—whatever thickness was present, it was strictly for structural stiffness of the wing. Extremely thin airfoil sections were perpetuated by the work of Horatio Phillips in England. Phillips carried out the first serious wind-tunnel experiments in which the aerodynamic characteristics of a number of different airfoil shapes were measured. (See section 5.20 of Reference 2 for a presentation of the historical development of airfoils.) Some of Phillips airfoil sections are shown in Figure 4.60—note that they are the epitome of exceptionally thin airfoils. The early pioneers of aviation such as Otto Lilienthal in Germany and Samuel Pierpont Langley in America (see chapter 1 of Reference 2) continued this thin airfoil tradition. This was especially true of the Wright brothers, who in the period of 1901–1902 tested hundreds of different wing sections and planform shapes in their wind tunnel in Dayton, Ohio (recall our discussion in Section 1.1 and the models shown in Figure 1.7). A sketch of some of the Wrights' airfoil sections
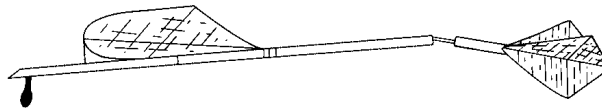
Figure 4.59 The first modern configuration airplane in history: George Cayley's model glider of 1804.
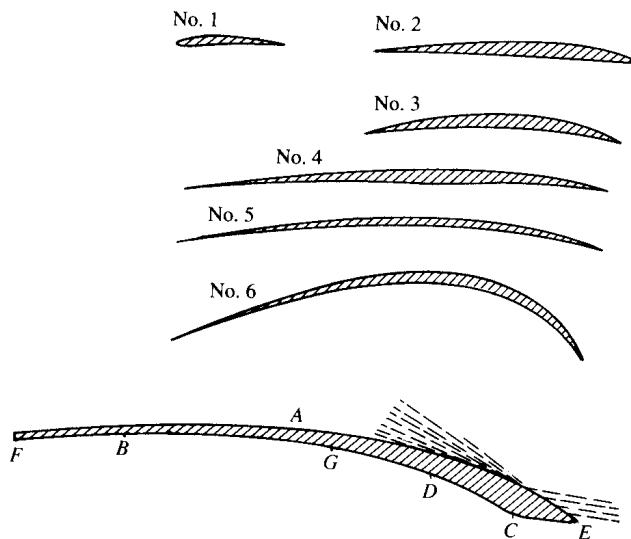

Figure 4.60 Double-surface airfoil sections by Horatio Phillips. The six upper shapes were patented by Phillips in 1884; the lower airfoil was patented in 1891. Note the thin profile shapes.

is given in Figure 4.61—for the most part, very thin sections. Indeed, such a thin airfoil section was used on the 1903 Wright Flyer, as can be readily seen in the side view of the Flyer shown in Figure 4.62. The important point here is that *all* of the early pioneering aircraft, and especially the Wright Flyer, incorporated very thin airfoil sections—airfoil sections that performed essentially like the flat plate results discussed in Section 4.13, and as shown in Figure 4.51 (the dashed curve) and by the streamline pictures in Figure 4.52. Conclusion: These early airfoil sections suffered flow-field separation at small angles of attack and, consequently, had low values of $c_{l,\max}$. By the standards we apply today, these were simply very poor airfoil sections for the production of high lift.

This situation carried into the early part of World War I. In Figure 4.63, we see four airfoil sections that were employed on World War I aircraft. The top three sections had thickness ratios of about 4 to 5 percent and are representative of the type of sections used on all aircraft until 1917. For example, the SPAD XIII (shown in Figure 3.50), the fastest of all World War I fighters, had a thin airfoil section like the Eiffel section shown in Figure 4.63. Why were such thin airfoil
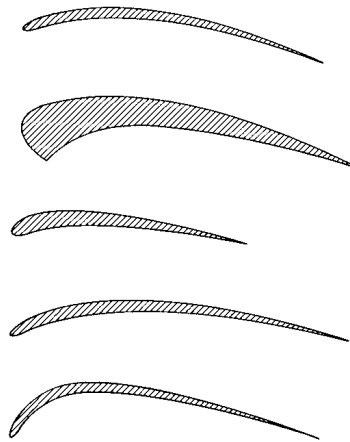
Figure 4.61 Some typical airfoil shapes tested by the Wright brothers in their wind tunnel during 1902–1903.
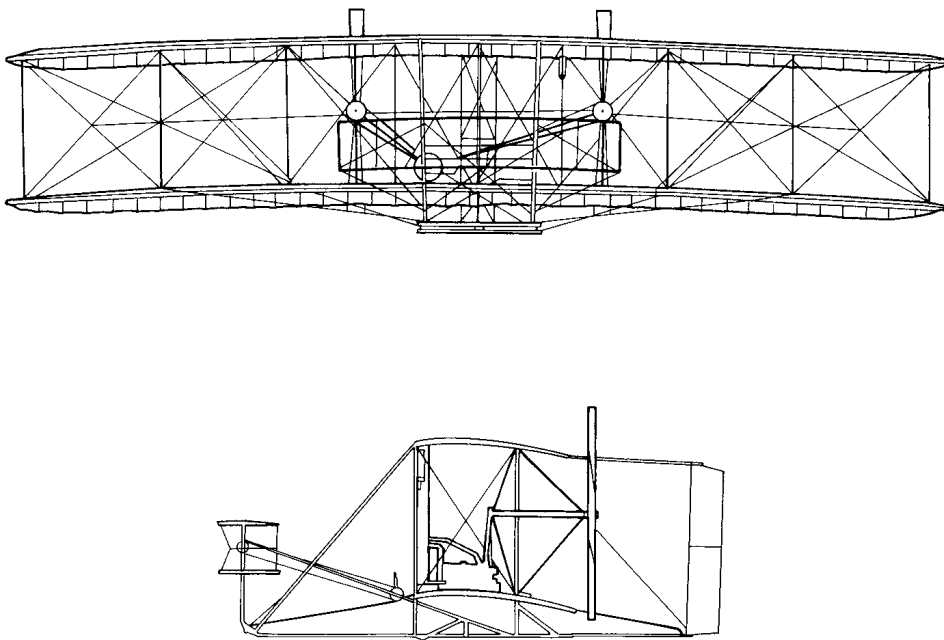

Figure 4.62 Front and side views of the 1903 Wright Flyer. Note the thin airfoil sections. *(Courtesy of the National Air and Space Museum.)*

sections considered to be the best by most designers of World War I aircraft? The historical tradition described above might be part of the answer—a tradition that started with Cayley. Also, there was quite clearly a mistaken notion at that time that *thick* airfoils would produce high drag. Of course, today we know the opposite
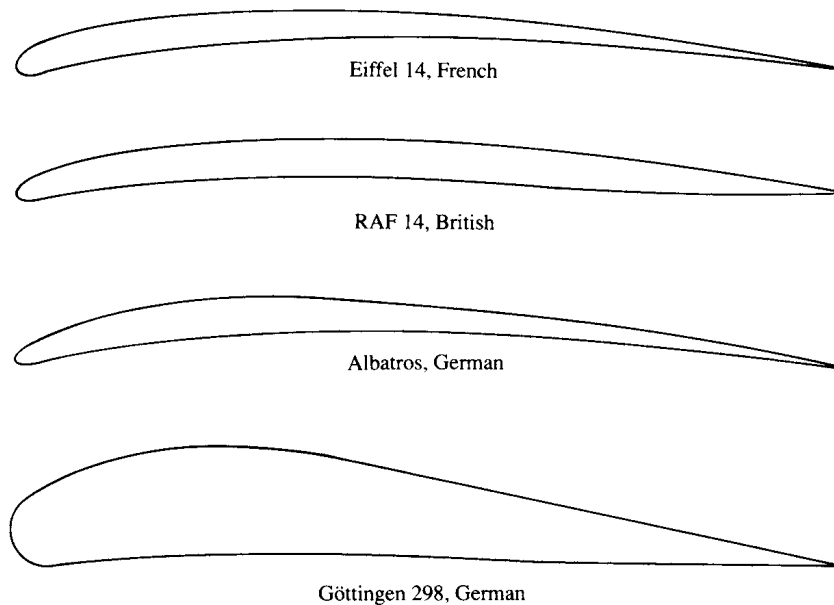
Eiffel 14, French

RAF 14, British

Albatros, German

Göttingen 298, German

Figure 4.63 Some examples of different airfoil shapes used on World War I aircraft. *(Source: Loftin, Reference 48.)*

to be true; review our discussion of streamlined shapes in Section 1.12 for this fact. Laurence Loftin in Reference 48 surmises that the mistaken notion might have been fostered by early wind-tunnel tests. By the nature of the early wind tunnels in use—small sizes and very low speeds—the data were obtained at very low Reynolds numbers, less than 100,000 based on the airfoil-chord length. These Reynolds numbers are to be compared with typical values in the millions for actual airplane flight. Modern studies of low Reynolds number flows over conventional thick airfoils (e.g., see Reference 51) clearly show high-drag coefficients, in contrast to the lower values that occur for the high Reynolds number associated with the flight of full-scale aircraft. Also, the reason for the World War I airplane designer's preference for thin airfoils might be as simple as the tendency to follow the example of the wings of birds, which are quite thin. In any event, the design of all English, French, and American World War I aircraft incorporated thin airfoils and, consequently, suffered from poor high-lift performance. The fundamentals of airfoil aerodynamics as we know them today (and as being presented in this book) were simply not sufficiently understood by the designers during World War I. In turn, they never appreciated what they were losing.

This situation changed dramatically in 1917. Work carried out in Germany at the famous Göttingen aerodynamic laboratory of Ludwig Prandtl (see Section 5.8 for a biographical sketch of Prandtl) demonstrated the superiority of a thick airfoil section, such as the Göttingen 298 section shown at the bottom of Figure 4.63. This revolutionary development was immediately picked up by the famous designer Anthony Fokker, who incorporated the 13-percent-thick Göttingen 298 profile in his new Fokker Dr-1—the famous triplane flown by the "Red Baron," Rittmeister
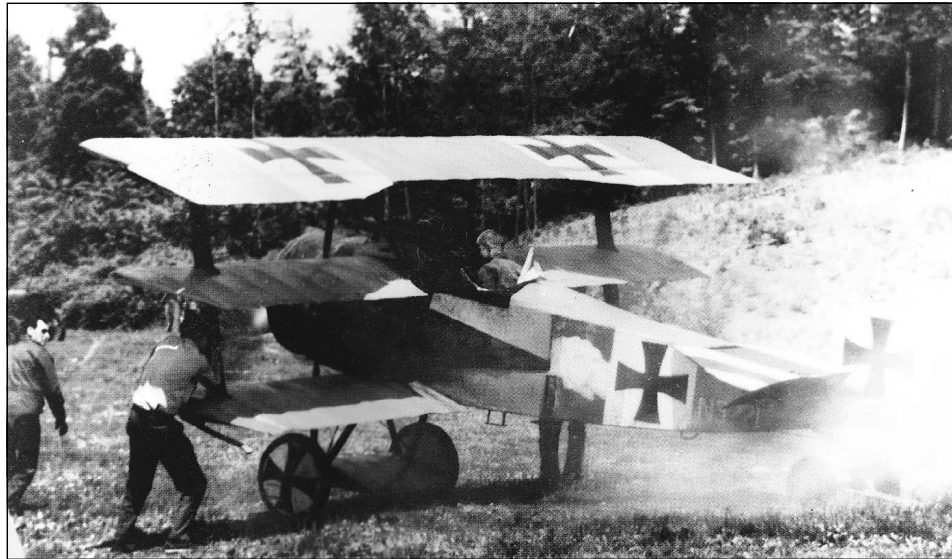
Figure 4.64 The World War I Fokker Dr-1 triplane, the first fighter aircraft to use a thick airfoil. *(Source: Loftin, Reference 48.)*

Manfred Freiher von Richthofen. A photograph of the Fokker Dr-1 is shown in Figure 4.64. The major benefits derived from Fokker's use of the thick airfoil were:

1. The wing structure could be completely internal; that is the wings of the Dr-1 were a cantilever design, which removed the need for the conventional wire bracing that was used in other aircraft. This, in turn, eliminated the high drag associated with these interwing wires, as discussed at the end of Section 1.11. For this reason, the Dr-1 had a zero-lift drag coefficient of 0.032, among the lowest of World War I airplanes. (By comparison the zero-lift drag coefficient of the French SPAD XIII was 0.037.)

2. The thick airfoil provided the Fokker Dr-1 with a high maximum lift coefficient. Its performance was analogous to the *upper* curves shown in Figure 4.51. This in turn, provided the Dr-1 with an exceptionally high rate-of-climb as well as enhanced maneuverability—characteristics that were dominant in dog-fighting combat.

Anthony Fokker continued the use of a thick airfoil in his design of the D-VII, as shown in Figure 4.65. This gave the D-VII a much greater rate-of-climb than its two principal opponents at the end of the war—the English Sopwith Camel and the French SPAD XIII, both of which still used very thin airfoil sections. This rate-of-climb performance, as well as its excellent handling characteristics, singled out the Fokker D-VII as the most effective of all German World War I fighters. The respect given by the Allies to this machine is no more clearly indicated than by a paragraph in article IV of the armistice agreement, which lists war material

Figure 4.65 The World War I Fokker D-VII, one of the most effective fighters of the war, due in part to its superior aerodynamic performance allowed by a thick airfoil section. (*Source:* Loftin, Reference 48.)

to be handed over to the Allies by Germany. In this article, the Fokker D-VII is *specifically* listed—the only airplane of any type to be explicitly mentioned in the armistice. To this author's knowledge, this is the one and only time where a breakthrough in airfoil technology is essentially reflected in any major political document, though somewhat implicitly.

4.15 HISTORICAL NOTE: KUTTA, JOUKOWSKI, AND THE CIRCULATION THEORY OF LIFT

Frederick W. Lanchester (1868–1946), an English engineer, automobile manufacturer, and self-styled aerodynamicist, was the first to connect the idea of circulation with lift. His thoughts were originally set forth in a presentation given before the Birmingham Natural History and Philosophical Society in 1894 and later contained in a paper submitted to the Physical Society, which turned it down. Finally, in 1907 and 1908, he published two books, entitled *Aerodynamics* and *Aerodonetics*, where his thoughts on circulation and lift were described in detail. His books were later translated into German in 1909 and French in 1914. Unfortunately, Lanchester's style of writing was difficult to read and understand; this is partly responsible for the general lack of interest shown by British scientists in

Lanchester's work. Consequently, little positive benefit was derived from Lanchester's writings. (See Section 5.7 for a more detailed portrait of Lanchester and his work.)

Quite independently, and with total lack of knowledge of Lanchester's thinking, M. Wilhelm Kutta (1867–1944) developed the idea that lift and circulation are related. Kutta was born in Pitschen, Germany, in 1867 and obtained a Ph.D. in mathematics from the University of Munich in 1902. After serving as professor of mathematics at several German technical schools and universities, he finally settled at the Technische Hochschule in Stuttgart in 1911 until his retirement in 1935. Kutta's interest in aerodynamics was initiated by the successful glider flights of Otto Lilienthal in Berlin during the period 1890–1896 (see chapter 1 of Reference 2). Kutta attempted theoretically to calculate the lift on the curved wing surfaces used by Lilienthal. In the process, he surmised from experimental data that the flow left the trailing edge of a sharp-edged body smoothly and that this condition fixed the circulation around the body (the Kutta condition, described in Section 4.5). At the same time, he was convinced that circulation and lift were connected. Kutta was reluctant to publish these ideas, but after the strong insistence of his teacher, S. Finsterwalder, he wrote a paper entitled "Auftriebskrafte in Stromenden Flussigkecten" (Lift in Flowing Fluids). This was actually a short note abstracted from his longer graduation paper in 1902, but it represents the first time in history where the concepts of the Kutta condition as well as the connection of circulation with lift were officially published. Finsterwalder clearly repeated the ideas of his student in a lecture given on September 6, 1909, in which he stated:

> On the upper surface the circulatory motion increases the translatory one, therefore there is high velocity and consequently low pressure, while on the lower surface the two movements are opposite, therefore there is low velocity with high pressure, with the result of a thrust upward.

However, in his 1902 note, Kutta did not give the precise quantitative relation between circulation and lift. This was left to Nikolai E. Joukowski (Zhukouski). Joukowski was born in Orekhovo in central Russia on January 5, 1847. The son of an engineer, he became an excellent student of mathematics and physics, graduating with a Ph.D. in applied mathematics from Moscow University in 1882. He subsequently held a joint appointment as a professor of mechanics at Moscow University and the Moscow Higher Technical School. It was at this latter institution that Joukowski built in 1902 the first wind tunnel in Russia. Joukowski was deeply interested in aeronautics, and he combined a rare gift for both experimental and theoretical work in the field. He expanded his wind tunnel into a major aerodynamics laboratory in Moscow. Indeed, during World War I, his laboratory was used as a school to train military pilots in the principles of aerodynamics and flight. When he died in 1921, Joukowski was by far the most noted aerodynamicist in Russia.

Much of Joukowski's fame was derived from a paper published in 1906, wherein he gives, for the first time in history, the relation $L' = \rho_\infty V_\infty \Gamma$—the

Kutta-Joukowski theorem. In Joukowski's own words:

> If an irrotational two-dimensional fluid current, having at infinity the velocity V_∞ surrounds any closed contour on which the circulation of velocity is Γ, the force of the aerodynamic pressure acts on this contour in a direction perpendicular to the velocity and has the value
>
> $$L' = \rho_\infty V_\infty \Gamma$$
>
> The direction of this force is found by causing to rotate through a right angle the vector V_∞ around its origin in an inverse direction to that of the circulation.

Joukowski was unaware of Kutta's 1902 note and developed his ideas on circulation and lift independently. However, in recognition of Kutta's contribution, the equation given above has propagated through the twentieth century as the "Kutta-Joukowski theorem."

Hence, by 1906—just 3 years after the first successful flight of the Wright brothers—the circulation theory of lift was in place, ready to aid aerodynamics in the design and understanding of lifting surfaces. In particular, this principle formed the cornerstone of the thin airfoil theory described in Sections 4.7 and 4.8. Thin airfoil theory was developed by Max Munk, a colleague of Prandtl in Germany, during the first few years after World War I. However, the very existence of thin airfoil theory, as well as its amazingly good results, rests upon the foundation laid by Lanchester, Kutta, and Joukowski a decade earlier.

4.16 SUMMARY

Return to the road map given in Figure 4.7. Make certain that you feel comfortable with the material represented by each box on the road map and that you understand the flow of ideas from one box to another. If you are uncertain about one or more aspects, review the pertinent sections before progressing further.

Some important results from this chapter are itemized below:

A vortex sheet can be used to synthesize the inviscid, incompressible flow over an airfoil. If the distance along the sheet is given by s and the strength of the sheet per unit length is $\gamma(s)$, then the velocity potential induced at point (x, y) by a vortex sheet that extends from point a to point b is

$$\phi(x, y) = -\frac{1}{2\pi} \int_a^b \theta \gamma(s)\, ds \qquad (4.3)$$

The circulation associated with this vortex sheet is

$$\Gamma = \int_a^b \gamma(s)\, ds \qquad (4.4)$$

Across the vortex sheet, there is a tangential velocity discontinuity, where

$$\gamma = u_1 - u_2 \qquad (4.8)$$

The Kutta condition is an observation that for a lifting airfoil of given shape at a given angle of attack, nature adopts that particular value of circulation around the airfoil which results in the flow leaving smoothly at the trailing edge. If the trailing-edge angle is finite, then the trailing edge is a stagnation point. If the trailing edge is cusped, then the velocities leaving the top and bottom surfaces at the trailing edge are finite and equal in magnitude and direction. In either case,

$$\gamma(\text{TE}) = 0 \qquad (4.10)$$

Thin airfoil theory is predicated on the replacement of the airfoil by the mean camber line. A vortex sheet is placed along the chord line, and its strength adjusted such that, in conjunction with the uniform freestream, the camber line becomes a streamline of the flow while at the same time satisfying the Kutta condition. The strength of such a vortex sheet is obtained from the fundamental equation of thin airfoil theory:

$$\frac{1}{2\pi} \int_0^c \frac{\gamma(\xi)\, d\xi}{x - \xi} = V_\infty \left(\alpha - \frac{dz}{dx} \right) \qquad (4.18)$$

Results of thin airfoil theory:

Symmetric airfoil

1. $c_l = 2\pi\alpha$.
2. Lift slope $= dc_l/d\alpha = 2\pi$.
3. The center of pressure and the aerodynamic center are both at the quarter-chord point.
4. $c_{m,c/4} = c_{m,\text{ac}} = 0$.

Cambered airfoil

1.
$$c_l = 2\pi \left[\alpha + \frac{1}{\pi} \int_0^\pi \frac{dz}{dx} (\cos\theta_0 - 1)\, d\theta_0 \right] \qquad (4.57)$$
2. Lift slope $= dc_l/d\alpha = 2\pi$.
3. The aerodynamic center is at the quarter-chord point.
4. The center of pressure varies with the lift coefficient.

The vortex panel method is an important numerical technique for the solution of the inviscid, incompressible flow over bodies of arbitrary shape, thickness, and angle of attack. For panels of constant strength, the governing equations are

$$V_\infty \cos \beta_i - \sum_{j=1}^{n} \frac{\gamma_j}{2\pi} \int_j \frac{\partial \theta_{ij}}{\partial n_i} ds_j = 0 \qquad (i = 1, 2, \ldots, n)$$

and
$$\gamma_i = -\gamma_{i-1}$$

which is one way of expressing the Kutta condition for the panels immediately above and below the trailing edge.

4.17 PROBLEMS

4.1 Consider the data for the NACA 2412 airfoil given in Figure 4.10. Calculate the lift and moment about the quarter chord (per unit span) for this airfoil when the angle of attack is $4°$ and the freestream is at standard sea level conditions with a velocity of 50 ft/s. The chord of the airfoil is 2 ft.

4.2 Consider an NACA 2412 airfoil with a 2-m chord in an airstream with a velocity of 50 m/s at standard sea level conditions. If the lift per unit span is 1353 N, what is the angle of attack?

4.3 Starting with the definition of circulation, derive Kelvin's circulation theorem, Equation (4.11).

4.4 Starting with Equation (4.35), derive Equation (4.36).

4.5 Consider a thin, symmetric airfoil at $1.5°$ angle of attack. From the results of thin airfoil theory, calculate the lift coefficient and the moment coefficient about the leading edge.

4.6 The NACA 4412 airfoil has a mean camber line given by

$$\frac{z}{c} = \begin{cases} 0.25 \left[0.8\frac{x}{c} - \left(\frac{x}{c}\right)^2 \right] & \text{for } 0 \le \frac{x}{c} \le 0.4 \\ 0.111 \left[0.2 + 0.8\frac{x}{c} - \left(\frac{x}{c}\right)^2 \right] & \text{for } 0.4 \le \frac{x}{c} \le 1 \end{cases}$$

Using thin airfoil theory, calculate
(a) $\alpha_{L=0}$ (b) c_l when $\alpha = 3°$

4.7 For the airfoil given in Problem 4.6, calculate $c_{m,c/4}$ and x_{cp}/c when $\alpha = 3°$.

4.8 Compare the results of Problems 4.6 and 4.7 with experimental data for the NACA 4412 airfoil, and note the percentage difference between theory and experiment. (*Hint:* A good source of experimental airfoil data is Reference 11.)

4.9 Starting with Equations (4.35) and (4.43), derive Equation (4.62).

4.10 For the NACA 2412 airfoil, the lift coefficient and moment coefficient about the quarter-chord at −6° angle of attack are −0.39 and −0.045, respectively. At 4° angle of attack, these coefficients are 0.65 and −0.037, respectively. Calculate the location of the aerodynamic center.

4.11 Consider again the NACA 2412 airfoil discussed in Problem 4.10. The airfoil is flying at a velocity of 60 m/s at a standard altitude of 3 km (see Appendix D). The chord length of the airfoil is 2 m. Calculate the lift per unit span when the angle of attack is 4°.

4.12 For the airfoil in Problem 4.11, calculate the value of the circulation around the airfoil.

4.13 In Section 3.15 we studied the case of the lifting flow over a circular cylinder. In real life, a rotating cylinder in a flow will produce lift; such real flow fields are shown in the photographs in Figures 3.34(*b*) and (*c*). Here, the viscous shear stress acting between the flow and the surface of the cylinder drags the flow around in the direction of rotation of the cylinder. For a cylinder of radius R rotating with an angular velocity ω in an otherwise stationary fluid, the viscous flow solution for the velocity field obtained from the Navier-Stokes equations (Chapter 15) is

$$V_\theta = \frac{R^2\omega}{r}$$

where V_θ is the tangential velocity along the circular streamlines and r is the radial distance from the center of the cylinder. (See Schlichting, *Boundary-Layer Theory,* 6th ed., McGraw-Hill, 1968, page 81.) Note that V_θ varies inversely with r and is of the same form as the inviscid flow velocity for a point vortex given by Equation (3.105). If the rotating cylinder has a radius of 1 m and is flying at the same velocity and altitude as the airfoil in Problem 4.11, what must its angular velocity be to produce the same lift as the airfoil in Problem 4.11? (*Note:* You can check your results with the experimental data for lift on rotating cylinders in Hoerner, *Fluid-Dynamic Lift,* published by the author, 1975, p. 21–4, Fig. 5.)

4.14 The question is often asked: Can an airfoil fly upside-down? To answer this, make the following calculation. Consider a positively cambered airfoil with a zero-lift angle of −3°. The lift slope is 0.1 per degree. (*a*) Calculate the lift coefficient at an angle of attack of 5°. (*b*) Now imagine the same airfoil turned upside-down, but at the same 5° angle of attack as part (*a*). Calculate its lift coefficient. (*c*) At what angle of attack must the upside-down airfoil be set to generate the same lift as that when it is right-side-up at a 5° angle of attack?

4.15 The airfoil section of the wing of the British Spitfire of World War II fame (see Figure 5.19) is an NACA 2213 at the wing root, tapering to an NACA 2205 at the wing tip. The root chord is 8.33 ft. The measured profile drag coefficient of the NACA 2213 airfoil is 0.006 at a Reynolds number of

9×10^6. Consider the Spitfire cruising at an altitude of 18,000 ft. (a) At what velocity is it flying for the root chord Reynolds number to be 9×10^6? (b) At this velocity and altitude, assuming completely turbulent flow, estimate the skin-friction drag coefficient for the NACA 2213 airfoil, and compare this with the total profile drag coefficient. Calculate the percentage of the profile drag coefficient that is due to pressure drag. *Note:* Assume that μ varies as the square root of temperature, as first discussed in Section 1.8.

4.16 For the conditions given in Problem 4.15, a more reasonable calculation of the skin friction coefficient would be to assume an initially laminar boundary layer starting at the leading edge, and then transitioning to a turbulent boundary layer at some point downstream. Calculate the skin-friction coefficient for the Spitfire's airfoil described in Problem 4.15, but this time assuming a critical Reynolds number of 10^6 for transition.